Modeling of Compact Antennas for Wireless Communication in Complex Environment

By

Md. Mizanur Rahman

B.Sc. Eng., Bangladesh University of Engineering and Technology, Dhaka, 1993
M.Sc. Eng., Bangladesh University of Engineering and Technology, Dhaka, 1996

A Dissertation Submitted in Partial Fulfillment of the
Requirements for the Degree of

DOCTOR OF PHILOSOPHY

in the Department of Electrical and Computer Engineering

We accept this dissertation as conforming to the required standard

Dr. M. A. Stuchly, Supervisor (Dept. of Elec. and Comp. Eng.)

Dr. W. J. R. Hoefer, Departmental Member (Dept. of Elec. and Comp. Eng.)

Dr. J. Bornemann, Departmental Member (Dept. of Elec. and Comp. Eng.)

Dr. N. Djilali, Outside Member (Dept. of Mechanical Engineering)

Dr. E. V. Jull, External Examiner (Dept. of Elec. and Comp. Eng., University of British Columbia)

University of Victoria

Supervisor: Dr. Maria A. Stuchly

Abstract

Demand for low-profile and compact antennas has greatly increased due to miniaturization of electronic devices. High performance for these antennas is also desired. The conflicting nature of the requirements of high performance and compact size makes the design of these antennas challenging. The primary focus of this dissertation is to investigate and enhance the performance of various compact and low-profile antennas for wireless communications.

Two dual band antennas for handheld telephones have been designed for the operation in AMPS and PCS bands and investigated in presence of the user's head. Antenna performance is evaluated in terms of VSWR, far-field radiation patterns, and the specific absorption rate (SAR) of energy in the user's head. A finite difference time domain (FDTD) code has been used for the modeling of antennas and user's head.

Two wide band circularly polarized patch antennas have also been analyzed using an FDTD code. A Moment Method based code (Ensemble) has been used to verify the performance of the antennas. Excitation of surface waves within the substrate of patch antennas is one of the main reasons for their low efficiency. Recently developed 2D planar photonic band gap (PBG) structures can be used to prevent the propagation of these unwanted surface waves within a particular frequency band. An analytical model has been developed for two existing PBG structures that predicts the band gaps for these structures. A new PBG structure with lower operating frequency and multiple stop bands has also been developed and modeled using the proposed analytical model. The analytical results have been compared with FDTD computed results and a good agreement has been found. Finally, a wide band circularly polarized patch has been further analyzed and integrated with a PBG structure. A significant improvement in the antenna performance is obtained with the use of PBG structure. The numerical results obtained are in excellent agreement with the measured data.

Examiners:

Dr. M. A. Stuchly, Supervisor (Dept. of Elec. and Comp. Eng.)

Dr. W. J. R. Hoefer, Departmental Member (Dept. of Elec. and Comp. Eng.)

Dr. J. Bornemann, Departmental Member (Dept. of Elec. and Comp. Eng.)

Dr. N. Djilali, Outside Member (Dept. of Mechanical Engineering)

Dr. E. V. Jull, External Examiner (Dept. of Elec. and Comp. Eng., University of British Columbia)

Contents

List of Figures

List of Tables

List of Acronyms and Abbreviations

ABC	Absorbing Boundary Condition
AMPS	Advanced Mobile Phone Service
AR	Axial Ratio
CAD	Computer Aided Design
CATR	Compact Antenna Test Range
DCS	Digital Cellular System
FCC	Federal Communication Commission (U.S.)
FDTD	Finite Difference Time Domain
FEM	Finite Element Method
FVTD	Finite Volume Time Domain
GSM	Global System for Mobile Communication
GTD	Geometrical Theory of Diffraction
MoM	Method of Moment
PBC	Periodic Boundary Conditions
PBG	Photonic Band Gap
PCS	Personal Communications Services
PEC	Perfect Electric Conductor
PIFA	Planar Inverted F Antenna
PLF	Polarization Loss Factor
PMC	Perfect Magnetic Conductor
PML	Perfectly Matched Layer
PTD	Physical Theory of Diffraction
TLM	Transmission Line Matrix
SAR	Specific Absorption Rate
VNA	Vector Network Analyzer
VSWR	Voltage Standing Wave Ratio

Acknowledgements

I would like to express my heartiest appreciation to my supervisor, Dr. M. A. Stuchly for her continuous guidance and encouragement shown throughout this research work and the process of writing this dissertation. I can not thank you enough for your patience and forbearance with me. Special thanks to Dr. M. Okoniewski for his valuable suggestions as related to this work, especially on the numerical modeling. I would like to thank members of my dissertation committee Dr. W. J. R. Hoefer, Dr. J. Bornemann, and Dr. N. Djilali for taking time from their busy schedule, and for the valuable suggestions they provided.

I wish to thank Mr. K. Caputa for his day to day help with the computers in the lab and also with the measurements. My other colleagues in the lab, Elise, Mike, Trev, Asad, and Kimmo deserve special thanks for their valuable suggestions and help.

I would also like to express my appreciation to Dr. Lot Shafai, University of Manitoba for allowing me to use the anechoic chamber for the antenna measurements. Special thanks go to Brad for his help with the measurements. The financial support of the Canadian Commonwealth Scholarship and NSERC is greatly acknowledged.

Finally, I wish to express my deepest gratitude to my wife, Sharmin for her continuous support and encouragement. Sharmin, without your understanding, sacrifices, and prayers the dream would never come to reality, thanks.

To my mother, and to the memory of my father.

Chapter 1

Introduction

1.1 Motivation

With the recent advances in the wireless communications, the need for compact, low-profile, and high performance antennas has greatly increased. The greatest demand for these antennas is from personal communication systems (e.g. cellular telephones, pagers, mobile data systems and global positioning systems) and other mobile applications (e.g. automobiles, trains). Depending on applications, there are differences in antenna performance requirements (e.g. gain, bandwidth, polarization). However, compact and low-profile antennas are essential for such applications, for either mechanical reasons or due to the miniaturization of electronic equipment in general.

It is well known that, as the size of the antenna is reduced, the efficiency tends to degrade and the bandwidth becomes narrower [1]. So, the conflicting nature of the requirements of high performance and compact size makes the design of these antennas very challenging. In addition, the interaction of the antenna with its complex environment also effects its performance. These environments may include the presence of the user's body or other complex structures.

Since two frequency bands have been allocated for personal wireless communication (e.g. AMPS & PCS in North America and GSM & DCS in Europe) an antenna for handsets is needed that can operate in both the allocated frequency bands. These antennas are typically a few millimeters to 2-3 centimeters away from the user's body. This has consequences for both the antenna and the user. Since at microwave frequencies the user's body behaves like a lossy dielectric, its presence modifies the antenna characteristics. Also, a significant fraction of the radiated energy is absorbed by the user's body, resulting in lower antenna efficiency of the antenna and possible health risks for the user. So, from both antenna design and user's health risks points of view, the interaction of the human body with the antenna must be investigated and understood. Linear wire antennas have been most often used in the current generation of wireless telephones. For dual band operation, the use of two separate antennas has been reported in the literature [2], [3]. A single antenna that can operate in both the allocated bands would offer an attractive alternative.

Among the low-profile antennas, microstrip patch antenna is a strong candidate for different applications due to some attractive features (e.g. lightweight, compact size, thin profile, ease of fabrication, and especially reduced SAR in the user's head). Along with these advantages patch antennas have some inherent disadvantages, namely narrow impedance bandwidth and low efficiency [4]. A number of techniques for increasing the bandwidth have been reported in the literature, but most of them are achieved by increasing the volume of the antenna. Techniques for increasing the bandwidth without increasing the size of the antenna deserve further research.

One of the main reasons for low efficiency of patch antennas is the excitation of surface waves. Recently, a high-impedance electromagnetic surface has been investigated and shown to prevent the propagation of surface waves within a particular frequency band. These high-impedance surfaces are basically frequency selective surfaces that are referred to as 2D planar photonic band gap (PBG) structures. These structures offer promising performances when used as the ground plane for antennas. Investigations of antennas on PBG surfaces are relatively recent. Better understanding of their properties and more efficient design methods for 2D PBG structures are needed.

1.2 Objective and Contributions

The general objective of this thesis is to investigate performance of various antennas for wireless communications. The antennas considered for this research require numerical modeling for the evaluation of their performances because of the environment in which they operate. In most of the cases due to the presence of the user's body, which is a heterogeneous lossy dielectric, numerical simulation is necessary. Therefore, the finite difference time domain (FDTD) method is used for numerical modeling. The contributions of the thesis in antennas for wireless communication include:

1. **Dual-Band Antenna:** Design and characteristics evaluation of antennas for handsets that can operate in two allocated frequency bands (824-894 MHz and 1850-1900 MHz) of the personal communication service have been performed. Two different dual-band antennas have been designed, namely the sleeve-monopole and the dual-meander-sleeve. Qualitative performances of the antennas have been evaluated using the FDTD method

taking the proximity of the user's head into account. The specific absorption rates (SAR) of the energy within the user's head from the designed antenna are also evaluated.

2. **Broad Band Patch Antenna:** Two broad band microstrip patch antennas with circular polarization have been developed. To design the antennas numerical modeling is performed using the FDTD method.
3. **Modeling of PBG structures:** An analytic model for the existing 2D planar PBG structures has been developed. The transmission properties of the structures are computed numerically and compared with the results obtained by the analytical model. A new 2D planar PBG structures with lower operating frequency and multiple stop bands has also been developed and modeled using the proposed analytical model.
4. **Application of PBG structures:** One of the existing planar PBG structures has been used to enhance the performance of the circularly polarized broad band patch antenna.

1.3 Outline

Chapter 2 reviews the previous research related to the antennas for handsets and their interactions with the user. Some attention is devoted to the techniques for improving the bandwidths of microstrip patch antennas. It also presents some literature review related to the development of planar PBG structures and their application in antenna systems and explains how this work builds upon the previous knowledge.

Chapter 3 presents the modeling methods. Since all the numerical analysis in this work has been carried out using FDTD technique, a brief description of the method is given first. The different aspects of the modeling criteria are described. The model of the human head and the handset is described that has been used for handset antenna analysis. Next, the method for numerical evaluation of the specific absorption rate (SAR) has been validated by comparing the numerical results with the experimental results. Finally, the experimental methods for measuring the antenna properties have been described.

Chapter 4 describes the results regarding the dual-band handset antennas. First, a description of the antennas are given. Next, antenna performances in free space and in the presence of the user's head are presented and explained. It also presents the data regarding the SAR of radiated energy within the user's head from the designed antenna and compares those with recommended safety standards.

Chapter 5 analyzes two novel microstrip patch antennas with broad impedance bandwidth and circular polarization. After a brief description of the antennas, different aspects of the antenna design and analysis are described. Next, a discussion of the analysis and results is presented.

Chapter 6 describes various high-impedance surfaces for the low-profile antenna, which are basically 2D planar PBG structures. After a brief description of the analyzed structures, a simple analytical model of the 2D planar PBG structure is presented. The analytic design is compared with the results obtained by numerical modeling. Finally, it presents a new structure with a lower operating frequency and multiple stop bands. This new structure has also been modeled using the proposed analytical model and compared with the numerical results.

Chapter 7 examines the use of a planar PBG structure for the performance enhancement of circularly polarized patch antenna described in Chapter 5. First the design and analysis of both the reference and PBG patch antenna using FDTD method are described. Next, experimental results for these antennas are presented, followed by a discussion.

Chapter 8 closes the thesis with a few concluding remarks and description of the possible future extensions of this work.

Chapter 2

Literature Review

A brief review of literature related to this work is given. First, the research related to the modeling of handset antennas and their interaction with the user is reviewed. Design and characterization of both single and dual band antennas are discussed. Next, the advantages and limitations of microstrip patch antennas are discussed. As they have narrow impedance bandwidths, different techniques for improving their bandwidth are reviewed. Finally, the background material relevant to the development of planar PBG structures and their applications in different antenna systems are discussed.

2.1 Modeling of Handset Antennas

Wireless communication systems, especially those for the cellular communications have experienced enormous growth over the last decade. Antennas for handsets are receiving increasing interest as they constitute an important part of these systems [1]. Since the size of the handset units dramatically decreased in the last few years, the main design efforts have been devoted to maintaining approximately the same antenna performance (e.g. a gain of 0 dBi, bandwidth of $\sim 10\%$, and uniform coverage over the horizontal plane), while ensuring that the antenna is small enough. Different antennas are currently used for handsets that usually operate in a single frequency band (e.g. AMPS or GSM). The popular antennas for handsets include a monopole, a sleeve dipole, a normal mode helix, and a planar inverted F antenna (PIFA) [1]. Patch antennas have recently come into use. Performance analysis of most of the antennas has been done on an infinite ground plane. For these antennas, simple, closed form analytical formulas are available for evaluating the antenna performance (e.g. an operating frequency, radiation patterns, gain) [5]. For example, a monopole antenna on an infinite ground plane may be modeled by image theory as a dipole with one-half of the input impedance and double the peak directivity of the dipole [5]. But when the antennas are placed on a handset, the metallic part of the casing of the handset acts as a radiating element. Alternatively, one may consider the metal casing as the ground plane. Due to the small size of the ground plane, its edges act as scatterers which diffract the incident field. The diffraction from the edges modifies the current on the ground plane and alters the radiation pattern, causing scalloping [9] or nulls [10] in the forward radiation, the presence of back radiation (radiation behind the ground plane) [11], and higher cross polarization levels [10]. Other antenna parameters may be affected as well. The smaller the ground plane, the stronger the currents on its back side, resulting in stronger back radiation. The metal casing of the handset becomes an integral part of the antenna system itself.

Many analytical tools can be used to model the diffraction of fields from ground plane edges. These include such techniques as the method of moments (MoM) [14], the geometrical theory of diffraction (GTD) [7] and the physical theory of diffraction

(PTD) [7]. The MoM and the GTD are sometimes used together.

A monopole antenna on a conducting box has been studied in [10] and [12]. It has been shown that as the monopole antenna is moved from the center of the top surface towards the edges or a corner, the magnitude of the conductance decreases by 50%, the resonance frequency increases by a few percent, and deep nulls are produced in the radiation pattern. For a helical antenna, a reduction of the ground plane radius to approximately the radius of the helix results in a transition from forward to backfire radiation [13]. A PIFA attached to a rectangular metal box (handset) has been analyzed in [15]. The handset and the antenna has been modeled by wire grids and the MoM has been used to compute the antenna characteristics. A null around $\theta = 230^0$ is observed in the $E - plane$ radiation pattern due to the metal box.

To satisfy the rapid growth of the mobile telephony, an additional frequency band is used (e.g. PCS or DCS) [16]. Since there are two different frequency bands allocated, subscribers who travel over service areas employing different frequency bands need two separate antennas unless a dual-frequency antenna is used. Obviously the later is a better choice in terms of cost, complexity, and space usage. Recently, several dual-band antennas for handsets have been described [2], [3], [17]-[19]. These include both planar and wire antennas.

A dual frequency planar inverted F antenna (PIFA) has been described by Liu *et. al.* in [2]. A smaller antenna is inscribed in the original one to get the higher operating frequency and the two antennas are excited using separate feeds. A bandwidth of 7% and 6.25% has been obtained for lower and higher frequency bands, respectively. A capacitively loaded PIFA with capacitive feed has been proposed in [18] for dual frequency operation. The PIFA described in [18] also uses two different antennas and separate feeds. A smaller antenna size is achieved at the expense of a narrower bandwidth and complex structure. Both the antennas presented in [2] and [18] have been analyzed numerically using FDTD method with the handset modeled as a rectangular metal box. The numerical results have been verified using experimental measurements. Erätuali *et. al.* has described a dual frequency wire antenna consisting of two separate antennas (a monopole and a normal mode helix) placed with the monopole along the axis of the helix. The monopole and the helix are designed for using at the higher frequency and lower frequency band, respectively. Bandwidths obtained for higher and lower frequency are 9.6% and 8%, respectively. The handset in this work has been modeled using a wire grid model and the antenna has been analyzed using MoM.

Until recently, modeling of handset antennas has not taken the proximity of the user into account due to the complexity of modeling a human body. However, it is well known that antenna performance is affected by the presence of the user's head and often also the hand, which are heterogeneous lossy dielectric materials. Recent advances in numerical electromagnetic modeling techniques have made modeling of human body viable. Several numerical methods can and have been used for investigations of antenna in the proximity of models of human body. The models of the head range from a simple homogeneous semi-infinite plane or box [21], homogeneous or layered spheres [22], to anatomically based heterogeneous models [23], [25]. For heterogeneous models, the most suitable are the FDTD, the finite volume time domain (FVTD), and finite element (FEM) method.

Effects of the user proximity on the antenna performance have been investigated by several authors [20] - [26] using experimental and numerical techniques. An early experimental work on a 600 MHz dipole antenna next to a human body model has shown that scattering of fields by the body perturbs the current distribution on the antenna [20]. The body of the user has been modeled as a rectangular cylindrical plexiglass container filled with saline solution. A numerical analysis using the FDTD technique has been performed to investigate the effects of the body proximity on the antenna resonant frequency, input impedance, efficiency and far-field radiation pattern [22]. The numerical modeling includes a monopole antenna on a PCS device (a metal box), a head (modeled as a sphere of muscle tissue) and a hand grasping the phone (modeled as a block of muscle tissue). Antenna characteristics have been investigated at 914 MHz and 1890 MHz and verified by experimental measurements. The results show a decrease in resonant frequency of 10% and a decrease in efficiency of 55-57% due to the presence of the head and hand. A considerable amount of distortion is also observed in the radiation patterns of the antenna. Diffraction and scattering from the head also result in significant cross-polarization. The presence of the head results in a shadow effect, meaning that the magnitude of the far field radiation is less in the direction of the head compared to the other directions (by 2 dB at 915 MHz and by 12 dB at 1890 MHz). Similar tests have been performed by other investigators using an anatomically accurate head model (obtained from magnetic resonant imaging), a heterogeneous hand model and a variety of different antenna configurations mounted on handsets [23]. Antenna performance has been investigated at 915 MHz. A decrease in resonant frequency and bandwidth of 32 and 52% has been found, respectively. The numerical analysis, using a FDTD algorithm, agreed well with measurements.

Okoniewski and Stuchly [25] have investigated the interaction between the handset antenna and the user's head using both canonical and anatomically based models. It has been shown that both box and spherical models yield overestimated SAR values and box models provide distorted and unreliable results for the antenna far-field pattern. Watanabe *et. al.* [26] has shown that maximum local SAR is lower for a head model without ear than for one with ear. In both of these cases dielectric covered rectangular metal box has been used as the model of the handset. Tinniswood *et.al.* [27] used more accurate Computer Aided Design (CAD) files for the handset model and investigated the effects of wires and circuit boards inside the telephone on the antenna performance and SAR distribution. It has been observed that the CAD file and simple box model of the handset produce similar SAR distributions within the head in the region of the highest EM absorption close to the antenna.

2.2 Broad Band Patch Antennas

Microstrip antenna technology has been rapidly developing for the last two decades. It has found applications in a wide variety of microwave systems due to many advantages (e.g. low profile, lightweight, ease of fabrication, low cost)[4]. In addition, these antennas are mechanically rigid, which makes them less susceptible to damage than wire antennas. Microstrip antennas present an alternative option for cellular telephone handset as potentially the amount of radiation absorbed by the user should be minimized. However, there are some inherent drawbacks too. A narrow impedance bandwidth is probably the most significant disadvantage for this type of antenna. A typical impedance bandwidth for a basic microstrip patch element is 1 to 3% [28], compared with a 15% to 20% bandwidth of dipole, slot and horn antennas [4]. Thus, much of the research on microstrip antennas has been devoted to various techniques for increasing the impedance bandwidth. Electrically thick substrate increases the bandwidth, but the impedance locus becomes increasingly inductive [29], [30], making impedance matching difficult. In addition, surface waves are excited that lower the antenna efficiency. Other techniques generally fall into three categories: external impedance matching, use of multiple resonances, and addition of losses (to sacrifice efficiency for bandwidth). Usually, an improvement in bandwidth for printed antennas has only been achieved at the expense of an increase in volume or a loss in efficiency [31].

External impedance matching is an effective and simple method of widening the bandwidth because it usually does not require any modification of the antenna element itself. Impedance matching is typically achieved by adding a matching circuit to the feed network, usually on the same substrate as the antenna [32], [33]. The matching network may consists of tuning stubs, quarter-wave transformer sections, capacitively coupled lines, or active devices. Good results are achieved when the matching circuits are close to the antenna element. However, care must be taken to prevent the matching circuit from interfering with the antenna radiation pattern. An impedance bandwidth of about 25% has been obtained by matching the input impedance of a single microstrip element [33]. Using transistors in the matching network, matching combined with amplification has achieved a bandwidth of 24% and an added signal gain of approximately 10 dB [34]. As mentioned earlier, the input impedance of a patch becomes increasingly inductive as the substrate thickness increases, so an obvious approach to bandwidth improvement is to tune this inductance with a series capacitor. This technique has been implemented in [35], where the end of the center conductor of a coax feed is formed into a tab that does not contact the patch element. This arrangement forms a series capacitor which can be controlled by varying the size of the tab and spacing from the patch. Another approach, suggested by Hall [36], is to feed the patch with a coax probe in the usual manner, but with a circular or linear gap in the patch conductor around the feed point. This gap, however, must be very narrow to obtain sufficient coupling to the patch, so fabrication is difficult. Impedance matching can also be achieved by modifying the antenna itself (e.g. by creating slots in the patch e.g. [37]).

Alternatively, the bandwidth can also be increased by introducing dual or multiple closely-spaced resonances. For microstrip antennas, this can be achieved using stacked multiple patches [38], [39], or co-planar multiple-resonator elements [40], [41], and slot loading (cutting slots into the patch) [42]. The stacked patch configuration occupies less surface area than the co-planar patch configuration, and tight coupling is more easily achieved. The stacked patch can also be used in array configurations without the need for increased element spacing and the concomitant danger of grating lobes. However, using the stacked configuration makes fabrication, modification, and addition of components more difficult. In practice, the bottom and top patches are very close in size, with one slightly larger than the other to resonate at a lower frequency. Bandwidths of up to 10% to 20% have been achieved with stacked patches [43]. Using co-planar parasitic patches, a bandwidth of up to 25% has been achieved with one center fed patch and four surrounding parasitic patches [43]. This design has some potential drawbacks when compared to the stacked patch approach. First, to achieve close coupling between parasitic patches, very small gaps between the elements must be used, which makes a fabrication tolerance critical. In addition, since different parts of the configuration radiate with different phase and amplitude at different frequencies, the pattern and phase center usually change markedly over the frequency band of operation, especially for wider bandwidth designs. It may also be difficult to position coplanar feeds and matching networks on the board, since there is less space to mount them. For this reason, the driven patch is usually fed by coaxial probe, although aperture coupling can be used very conveniently. Slot loading does not increase the size of the antenna, as do the other two methods. Therefore, it is preferable in applications where size is critical. A bandwidth as wide as 47% obtained with slot loading has been reported in [42]. The resonant frequency and bandwidth can be adjusted by changing the depth and width of the notches.

Bandwidth improvement can also be achieved at the expense of efficiency by adding loss into the antenna system. This results, though, in decrease of radiation efficiency. Adding a 6 dB attenuator in series with a microstrip antenna leads to a minimum of 12 dB return loss over a broad band. The antenna gain is also reduced by 6 dB [43]. Losses can be added externally using attenuators, distributed using lossy substrate materials, or added to the antenna directly using chip resistors or other loads. This method of broad-banding is generally undesirable for all antenna design, and further reduces the already relatively low radiation efficiency of microstrip antennas.

2.3 PBG Structures for Antenna Applications

Photonic band gap (PBG) structures are a class of composite periodic structures that exhibit transmission (pass) and reflection (stop) bands in their frequency response. These bands in a photonic structure occur due to the constructive and destructive interference of the electromagnetic waves [44]. PBG structures can be made of dielectric only [45], or of metallic elements embedded in a dielectric material [46]. Two and three dimensional arrangements of the PBG crystals have been explored [47]. Recently, there has been increasing interest in PBG engineering for use at microwave and millimeter-wave frequencies. Numerous engineering applications of these structures have been described at microwave frequencies, such as microstrip filters [48], high power components [49], and magnetic conducting surfaces [50]. An application of PBG structures in antenna systems is also receiving interest. Kesler *et. al* [52] has described the application of a finite thickness slab of 2D, all dielectric PBG material as a planar reflector for a dipole antenna. A slab of *woodpile* PBG material has been examined as a planar, all-dielectric reflector for a dipole/monopole antenna [53]. Antenna characteristics such as the field pattern and input impedance have been obtained using full wave analysis.

PBG structures have been analyzed numerically by either calculating the dispersion diagram ($\beta - \omega$) [55], [56], or calculating the transmission and reflection coefficients [57], [58]. Due to the complexity of PBG structures, their characterization can be achieved only with full wave analysis. Numerical techniques such as plane wave expansion method [59], integral equation method [60], finite element method [61], finite difference both in frequency domain [62], [63], and time domain [52], [64] have proved effective for different structures. Some of these structures have also been modeled analytically. Plihal *et. al.* [56] has described a method of calculating the dispersion diagram of a 2D dielectric PBG structure. The structure in [56] consists of infinitely long, parallel, dielectric rods with circular cross section embedded in a different dielectric material. A position-dependent dielectric constant and the plane wave approximation are used to calculate the dispersion diagram of the structure.

Recently, a new class of 2D planar PBG structure has emerged [55], [50], [65]. The traditional 2D structures are uniform and extend to infinity in the third dimension, whereas this new class of 2D PBG structures is finite in the third dimension. The 2D planar PBG structures can prevent electromagnetic wave propagation along the surface of the structures and serve as high impedance surfaces within the stop band [55], [65], [66]. The PBG structure presented in [65], and shown in Fig. 2.1, is an array of small metal sheets (square or hexagon) connected to a continuous metal sheet using thin metal wires. The space between the top and bottom metal layer is filled with a dielectric material. This structure has been modeled using a "LC" parallel resonant circuit to predict the operating frequency. A finite element method has been used to calculate the dispersion diagram and has been verified by measurements. Another PBG structure, described in [50], and shown in Fig. 2.2, consists of a square metal pad with four narrow connecting branches and supported by a continuous ground plane. A dielectric material fills the space between the top metal layer and the ground plane. Transmission properties of the structure have been calculated using the FDTD method. A grounded periodic dielectric substrate with square lattice and finite height as shown in Fig. 2.3 has been analyzed in [55]. The effect of the height of the substrate on the band diagram has been determined using the FDTD method.

The high impedance property of 2D planar PBG structures such as those mentioned above makes them suitable candidates for ground planes for different antennas, whenever surface waves deteriorate antenna performance [51], [54] [66], [67]. Qian *et. al.* [51] have analyzed a simple microstrip patch antenna placed in a photonic band gap structure described in [65]. It has been shown that the radiation pattern of the patch antenna in the *E-plane* becomes narrower due to the suppression of the wave

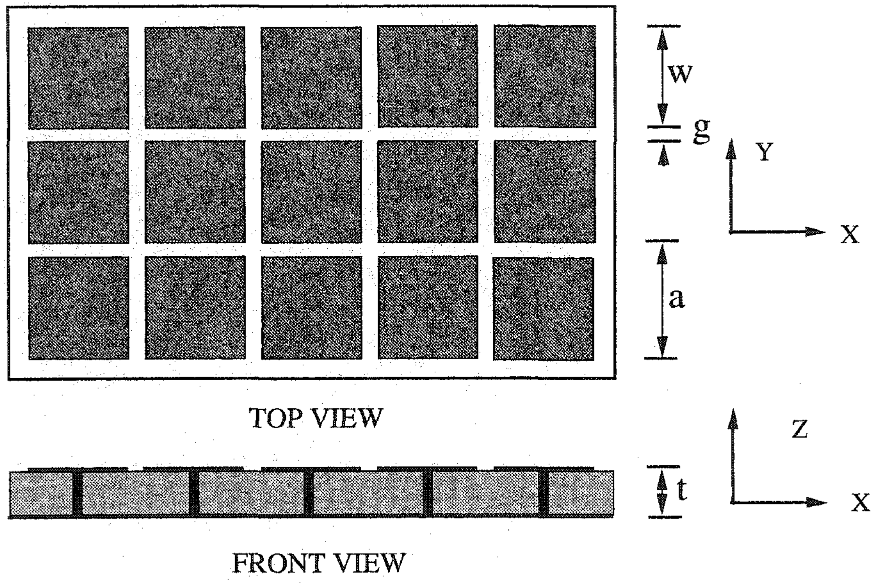

Figure 2.1: PBG structure consists of square array of square metal plates with shorting pins [65].

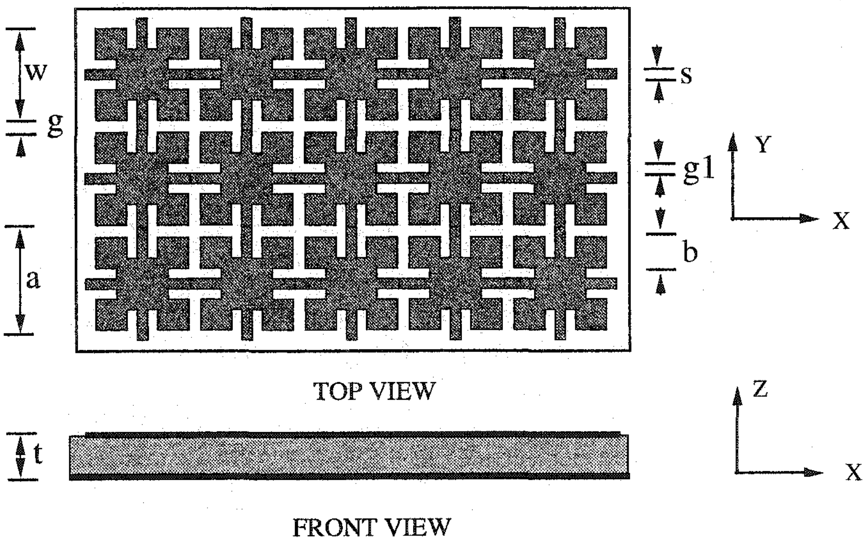

Figure 2.2: PBG structure consists of array of square metal plates with connecting branches [50].

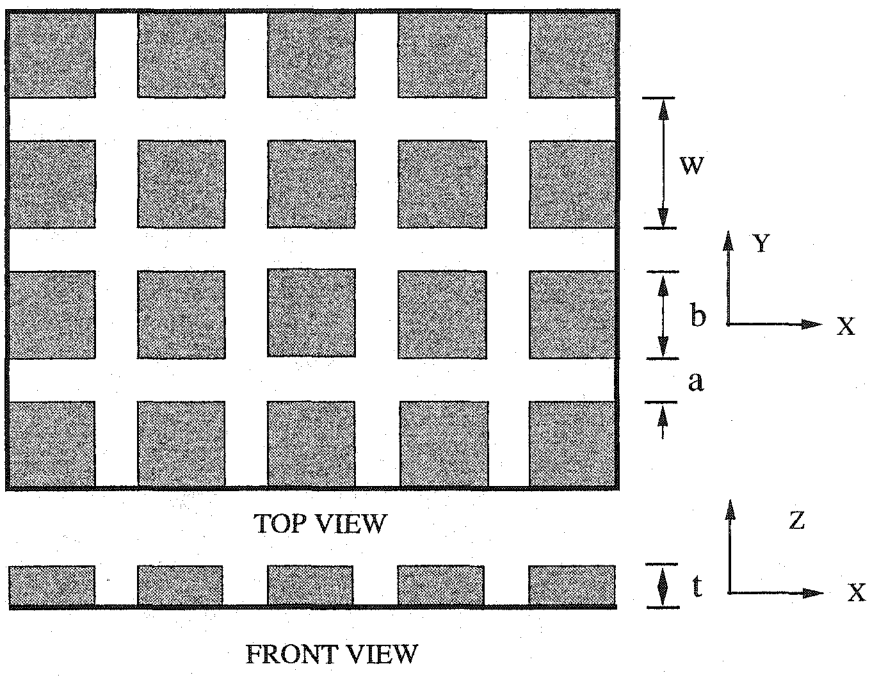

Figure 2.3: Grounded dielectric material with square lattice and finite height [55].

propagation along the surface. This increases the antenna gain. An improvement of the antenna bandwidth has also been reported. The use of the 2D planar PBG structure as a ground plane for vertical monopole and horizontal wire antennas improves their radiation patterns and increases their gain due to the suppression of the surface waves [65]. Similarly, an aperture-coupled patch antenna on a PBG structure described in [50], shows a significant improvement in antenna performance. The finite height grounded periodic dielectric, described in [55] (Fig. 2.3) has been used as a substrate for microstrip phased arrays [67]. It has been shown that the scan blindness of the phased arrays can be eliminated by using this PBG structure. A microstrip patch antenna with a finite ground plane, integrated with PBG substrate is reported in [54]. A significant reduction of back radiation has been observed due to the reduction of edge currents [54]. The antennas in [51], [54], [66], and [67] have been modeled with the FDTD technique due to its capability of analyzing complex structures. The results have often been verified by measurements.

2.4 Concluding Remarks

The review of present state of knowledge on handset antennas has indicated that dual-band antennas are likely be the next generation antennas for handsets. However, there is a paucity of reports on their design, and an apparent lack of antenna designs with a single feed. Furthermore, only few designs described in the literature for both single and double band operation have been analyzed in a realistic environment that includes a handset and a realistic model of the human head. Thus, one of the aims of this research is to design dual band antennas for handsets and analyze their performance in the proximity of an anatomically based human head model.

Microstrip antennas, due to the compact geometry and lower energy deposition in the user's body, are an attractive alternative to the other antenna configurations for handsets. As discussed, the development of microstrip antennas for handheld devises poses many challenges, including technological limitations (e.g. bandwidth and efficiency) and physical constraints (e.g. size). Moreover, most of the broadbanding techniques for microstrip antennas, presented in the literature, achieve wider bandwidth at the cost of increased volume and degraded performance.

Another new recent method of improving the antenna performance (e.g. gain, efficiency, bandwidth) is, as briefly reviewed, by the use of PBG materials for suppression of surface waves. Integration of 2D planar PBG structure as a high-impedance surface with antenna systems is relatively new. A shortage of reports on their analytical modeling is evident. Therefore, as a part of this research compact broadband patch antennas with the 2D planar PBG structures are analyzed and their applications for handsets and other wireless mobile antennas are explored.

For the analysis of antennas in complex environments such as proximity of a human body and mounting on a ground plane comparable in size to the wavelength, the most suitable methods are FDTD, FVTD, TLM and FEM. Time domain techniques offer an advantage of complete characterization of performance in the required range in one simulation. The FDTD has been most often used to analyze the handset antennas in the proximity of an anatomically based head model (composed of voxels) and complex PBG structures. Thus due to its capability of analyzing complex structures, robustness, and other inherent advantages, the FDTD method has been selected for numerical analysis in this research.

Chapter 3

Models and Methods

Due to the complex nature of the antennas and their environments considered in this work, numerical modeling is necessary. Besides, a complex structure such as PBG needs to be investigated using full wave analysis to get a better understanding of its behavior. As mentioned earlier, the FDTD method can be readily applied to the complex geometry of inhomogeneous dielectrics and metals. It is also suitable for obtaining the data of interest in a broad frequency range in one computational run. Therefore, it is well suited to the analysis of the different antennas and their environment studied in this work. This chapter briefly addresses the issues related to the accuracy of the FDTD modeling. Application of numerical methods to analyzing different antennas and PBG structures is described in more detail. The handset and human head models are presented. Methods for the verification of SAR determination and measurement of antenna properties are also outlined.

3.1 Finite-Difference Tome-Domain Method

The finite-difference time-domain method is a popular numerical electromagnetic technique that is based on solving the differential forms of Maxwell's equations [69]. The FDTD method is a time-domain technique, which requires the discretization of both time and space. The method iterates through time for a given number of time steps, and at each time step, the field components are updated using relatively simple linear equations.

The FDTD method, introduced to electromagnetics by Yee in 1976 [68], is a direct solution of Maxwell's differential equations. Two of the differential equations are [7]:

$$\nabla \times \bar{H} = \bar{J} + \frac{\partial \bar{D}}{\partial t} \tag{3.1}$$

$$\nabla \times \bar{E} = \bar{M} - \frac{\partial \bar{B}}{\partial t} \tag{3.2}$$

where $\bar{E}$ and $\bar{H}$ are the electric and magnetic field strength, $\bar{J}$ and $\bar{M}$ are the electric and magnetic current density, and $\bar{D}$ and $\bar{B}$ are the electric and magnetic flux density [7]. All of the field variables are functions of space and time, $f(x, y, z, t)$. To solve the differential equations numerically, space and time are discretized and differentiation is performed using finite-difference approximations. A commonly used finite-difference approximation is the central finite-difference formula, shown below for differentiation in the x direction:

$$\frac{\partial f(x,y,z,t)}{\partial x} \approx \frac{f\left(x+\frac{\Delta x}{2},y,z,t\right)-f\left(x-\frac{\Delta x}{2},y,z,t\right)}{\Delta x} \tag{3.3}$$

where Δx is an increment in the x direction. It can be shown that applying the central finite-difference formula to (3.1) and (3.2) produces a set of six scalar equations in which the field values at each point in time and space are related only to field values at neighboring points [69]. Thus, the solution of each field value does not depend on the formulation of large matrices, which is a great advantage of the FDTD method. However, $\bar{E}$ and $\bar{H}$ must be evaluated at all nodes in the computational space. This is accomplished by iterating through space along a regular grid. A unit cell of the grid, known as Yee cell, is shown in Fig. 3.1. As shown in Fig. 3.1, $\bar{E}$ and $\bar{H}$ field components are evaluated at different locations on the grid. They are also evaluated at alternate time steps. To ensure the numerical stability of the FDTD method, the time stepping increment, Δt, must be less than the Courant limit [70]:

$$\Delta t = S\sqrt{\mu\varepsilon}\left[\frac{1}{\Delta x^2}+\frac{1}{\Delta y^2}+\frac{1}{\Delta z^2}\right]^{-\frac{1}{2}} \tag{3.4}$$

where μ and ε are the permeability and permittivity of the medium, respectively, and $S \leq 1$ is the stability coefficient.

For sufficient accuracy of the results, spatial increments in the Yee grid $(\Delta x, \Delta y, \Delta z)$ must be small in wavelengths $(\lambda/10 - \lambda/20)$, and a sufficient number of time steps must be chosen [69]. Even smaller grid or special algorithms have to be used to represent highly non-uniform fields. Accuracy also depends on the proper application of boundary conditions and the accurate modeling of metals and dielectric materials.

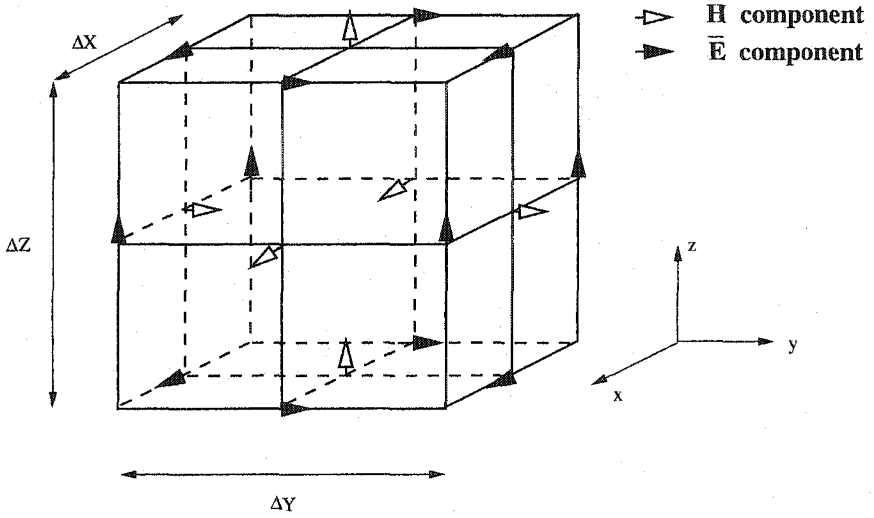

Figure 3.1: Yee cell in the FDTD method.

Absorbing boundary conditions (ABCs) have been formulated which simulate the effect of an unbounded region. Different types of ABCs are used for various applications, as their advantages and limitations are dependent on their use. One of the most popular and advantageous ABCs is the perfectly matched layer (PML) introduced in 1994 by Berenger [71]. PMLs can provide a reflection smaller than -60 to -110dB for an arbitrary angle of incidence and even when the boundary is placed no more than 5 cells from the surface of the scatterer.

The accurate modeling of metal and dielectric objects is an important issue in the FDTD method, particularly if the FDTD grid does not conform to the shape of the object, or if the object is small compared to the size of the cell. A two-dimensional example of the later situation is shown in Fig. 3.2a. In this geometry, two metal sheets are modeled whose thickness is less than the height of the Yee cell. Conventional FDTD update equations for this geometry either ignore the metal sheets or assume that they occupy the entire volume of their cells. Either approach results in a considerable error. A finer spatial discretization may be used, as shown in Fig.3.2b, but this may place impractical demands on the available computer memory or computational time. Improvements can be made to the conventional FDTD algorithm that increases the modeling accuracy while maintaining the computational efficiency. These improvements include subcell gridding, using nonuniform grids, and subcell modeling [72]. In the subcell gridding method, shown in Fig.3.2c, a fine grid is used around the small features, while a regular coarse grid is used in the remaining region. Nonuniform grids, as shown in Fig.3.2d, are made gradually denser near the small features. Subcell modeling is often used when it is impractical to decrease the mesh size to the dimensions of the object, even if subcell gridding or nonuniform gridding is used. In subcell modeling the update equations are modified near the object of interest rather than modifying the grid. The new update equations are typically based on the integral forms of Maxwell's equations that take into account assumptions of field behavior in the region of interest. For example, modeling of thin wires with radii greater than zero and less than one cell width requires modifying Yee's standard FDTD update equations in the cells adjacent to the wires [68]. Subcell modeling is also used to model wires with circular cross section and diameter not equal to the multiple of the cell width. Modeling of metal sheet edges is another example of subcell modeling. A special algorithm is also required to accurately model the field singularity at the edges.

A more detailed description of the different aspects of the modeling is discussed in the subsequent sections for different applications considered in this work. For modeling different structures and antennas studied in this work, an in house developed FDTD is used. The accuracy of the code has been verified previously for a wide range

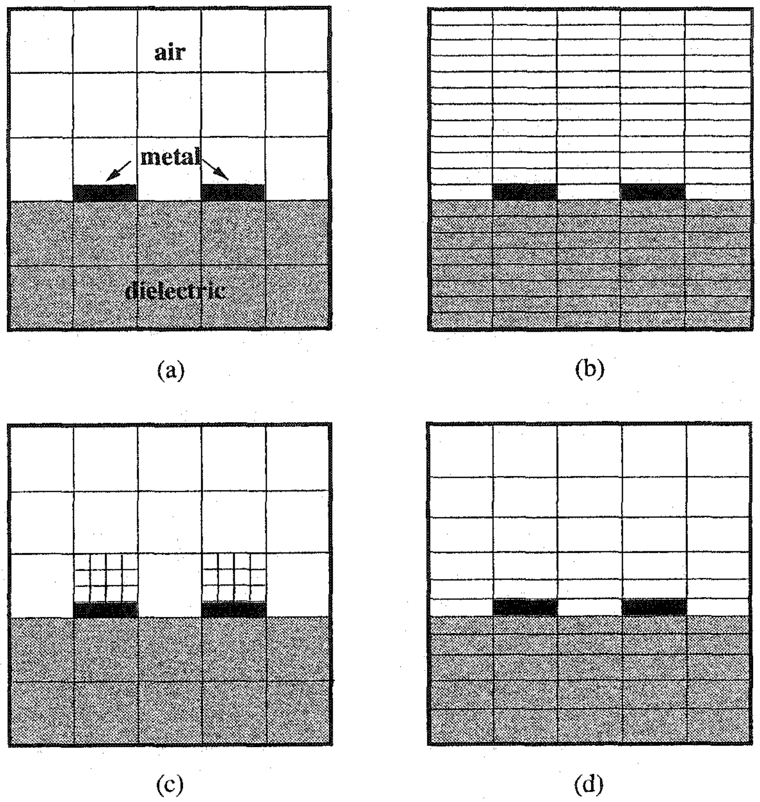

Figure 3.2: FDTD modeling of coplanar lines using (a) a coarse grid, (b) a fine grid, (c) a subcell grid, and (d) a nonuniform grid.

of electromagnetic problems [25], [73]-[75].

3.2 Computational Method

3.2.1 Antennas on Handsets

The Yee-cell, rectangular grid [68] and the total-field formulation [69] are used in FDTD code. The computational space is truncated with perfectly matched layers (PML) placed 4 to 5 cells away from the nearest surface of the objects. Parameters of the PML are selected to ensure boundary reflections below a desired limit with a minimum number of layers. For the discretization of the computational space, appropriate mesh sizes are used to represent antennas and other structures accurately and simultaneously limit computational resources. Both uniform and nonuniform grids are used.

A special algorithm is used to handle dielectric objects with shapes and/or voxels that do not coincide with the FDTD mesh. This algorithm considers the field continuity conditions and the integral form of Maxwell's equations in a sub-cell regime. Using fast logic integration, the weighted flux averages are computed and look-up tables of the dielectric constant and conductivity are assembled for each field component separately. This algorithm increases the accuracy of computations, particularly when, for example, the human head model is not aligned with the coordinate system. In the cases where the metal surfaces do not coincide with the mesh, another specialized algorithm is used that allows for accurate treatment of fields near these surfaces [76].

All the structures are excited using a gap excitation with the time-domain envelope of a frequency-shifted Gaussian pulse. The center frequency and the pulse width are selected to cover the entire frequency range of interest.

For antenna analysis, the far field radiation pattern is obtained by transformation in the frequency domain of the computed near field electric and magnetic field vectors on a box (Huygen's surface) enclosing the modeled structures using the field equivalence principle [69]. An input impedance for different antennas is computed, using the voltage across the feed gap and the current at the feed point of the antenna, as follows:

$$Z_{in}(\omega) = \frac{\mathcal{F}\left[V(t)\right]}{\mathcal{F}\left[I(t)\right]} exp\left[-j\omega\frac{\Delta t}{2}\right] \tag{3.5}$$

where $Z_{in}(\omega)$ is the input impedance in frequency domain, and $\mathcal{F}\left[V(t)\right]$ and $\mathcal{F}\left[I(t)\right]$ are the FT of the time domain data of input voltage and current, respectively. The voltage ($V(t)$) is computed from the electric field along the feed line and the current ($I(t)$) is computed from the magnetic fields around a small loop centered at the feed-point. A correction factor of $\frac{\Delta t}{2}$, where Δt is the time step, is used to account for the time shift between the grid points at which the voltage and current are evaluated [69].

The antenna efficiency, when placed near the human head, is computed as:

$$\eta = \frac{P_{rad}}{P_{rad} + P_{abs}} \tag{3.6}$$

where P_{abs} is the power absorbed in the volume V of the head:

$$P_{abs} = \frac{1}{2} \int_{V} \sigma |E_t|^2 dv \tag{3.7}$$

and P_{rad} is the radiated power from the antenna and obtained as:

$$P_{rad} = \frac{1}{2} \int_{S} Re(\bar{E} \times \bar{H}^*) \cdot d\bar{s} \tag{3.8}$$

where the surface S encloses the antenna-head configuration, E_t and σ are the magnitude of an induced electric field in the biological tissue and tissue conductivity, respectively. $\bar{E}$ and $\bar{H}$ are the total electric and magnetic fields, and dv and $d\bar{s}$ are the differential volume and differential surface vector, respectively. The induced electric field distribution within the body is highly dependent on the geometry of the head, the external field frequency and polarization, and other factors [77]. A generally accepted dosimetry measure of RF exposure is the specific absorption rate (SAR), which is defined as the power absorbed per unit mass of tissue. It is calculated from the induced electric field $\bar{E}_t$ in the biological tissue as [78]:

$$SAR = \frac{\sigma}{2\rho} |E_t|^2 \quad W/kg \tag{3.9}$$

where ρ is the tissue specific density. The SAR can be computed for a single voxel or a number of voxels forming a volume of certain mass. For compliance with standards in the US and Europe, the SAR averaged over 1 g [79] or 10 g [80] of cube shaped tissue must not exceed a specific value. The guidelines do not specify how the averaging should be done, neither do they give any specifics regarding air inclusions in the cube volume. In this research an averaging algorithm has been used that permits the averaging over the specified cube mass with selectable air content at the outer bound of the cube [81]. An air content of 20% has been selected for this work. Such a large air content in the cube gives a higher SAR value than for a lower air content.

The biological head model (described in 3.3.2) used in this work for modeling the antenna-head interaction has electrical properties that are dispersive in nature. The dielectric properties of the model change significantly over the frequency range of interest. The FDTD code used for this work is not capable of handling this dielectric dispersion. To overcome this problem, two sets of dielectric values for the head model at 835 MHz and 1900 MHz have been used. Within each bandwidth of interest the permittivity values vary very little with frequency. The antenna properties and the SAR distribution within the head are computed at 835 MHz and 1900 MHz using two FDTD runs with the corresponding dielectric values of the head model.

3.2.2 Broad Band Patch Antennas

Broad band patch antennas described in Chapter 5 and 7 are also designed using the FDTD method. In the FDTD simulations, antennas are placed over large finite ground planes. Input impedances and components of the radiated fields are computed in the same way as described in the previous section. The E_θ and E_ϕ components of the computed radiation patterns are further used to compute the polarization loss factor (PLF) for incident right circularly polarized (RCP) waves and the axial ratio (AR) of the circularly polarized waves radiated by the antennas. The PLF and AR are computed as follows [5]:

$$PLF = 10log_{10}\left|\rho_{\mathrm{i}}.\rho_{\mathrm{r}}\right|^2 \tag{3.10}$$

where ρ_i and ρ_r are the unit vectors of the incident and radiated fields respectively.

and

$$AR = \frac{OA}{OB} \tag{3.11}$$

where

$$OA = \left[\frac{1}{2}\left\{|E_\theta|^2 + |E_\phi|^2 + \left[|E_\theta|^4 + |E_\phi|^4 + 2|E_\theta|^2|E_\phi|^2cos(2\Delta\phi)\right]^{1/2}\right\}\right]^{1/2} \tag{3.12}$$

$$OB = \left[\frac{1}{2}\left\{|E_\theta|^2 + |E_\phi|^2 - \left[|E_\theta|^4 + |E_\phi|^4 + 2|E_\theta|^2|E_\phi|^2cos(2\Delta\phi)\right]^{1/2}\right\}\right]^{1/2} \tag{3.13}$$

and $\Delta\phi$ is the phase difference between E_θ and E_ϕ.

The broad-band patch antenna developed in this work is additionally analyzed using a moment method based package, Ensemble® (Ansoft, Pittsburg) [83]. Ensemble provides rapid results for simple antennas, as well as an estimate of the antenna gain which is not available in our FDTD code. Because the FDTD is a time-domain technique, the frequency response of the antenna is obtained from a single simulation with an appropriate excitation. However, relatively long simulation times are required because of the resonant structure. Ensemble requires solutions at a number of frequencies. Finally, many results can be verified by comparison of the results obtained with the two programs.

The Ensemble solution is based on the mixed potential integral equation which expresses fields of electric and magnetic surface currents by Green's functions [83]. The resulting integral equation is approximated by dividing the solution region into cells and approximating the currents in the cells with basis functions. The Ensemble approach allows for use of triangular and rectangular elements. Coaxial probes (wires with voltage gap sources) are modeled with attachment modes for greater accuracy. For simulating the microstrip patch antennas in this work an infinite ground plane is used. Structures are meshed with a minimum grid resolution of $\lambda/17$, with increased resolution in selected subregions, e.g. along the edge of the patches.

3.2.3 Photonic Band Gap Structures

For the analysis of the photonic band gap structures in Chapter 6, reflection (S_{11}) and transmission (S_{21}) coefficients are computed. Surface waves (coupled LSE and LSM modes to the normal to the surface) are launched along the substrate by an open ended microstrip line and detected by another microstrip line aligned with the first one, as shown in Fig. 3.3. The PBG structures are inserted between the two microstrip lines as in [66]. Signals are recorded at four points, three on the input side with equal spacing between them and the other one on the output side (Fig. 3.3). First, these FDTD computed time domain signals are transformed into frequency domain using FT. Then the three frequency domain signals from the input side are used to separate the incident ($E_{inc}(f)$) and reflected ($E_{ref}(f)$) signals using the method outlined in [82]. The reflection and transmission coefficients are calculated using:

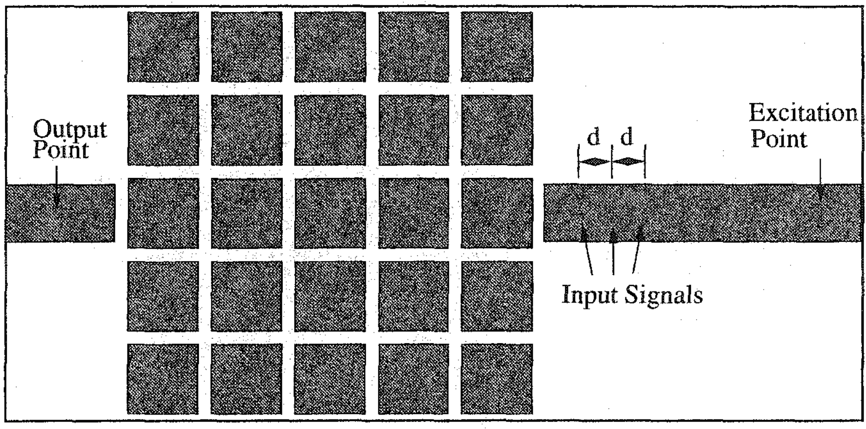

Figure 3.3: Transmission through PBG structure.

$$S_{11} = 20log_{10}\frac{|E_{ref}(f)|}{|E_{inc}(f)|} \tag{3.14}$$

and

$$S_{21} = 20log_{10}\frac{|E_{out}(f)|}{|E_{inc}(f)|} \tag{3.15}$$

where $E_{out}(f)$ is the output signal in frequency domain.

The FDTD method has also been used to evaluate the reflection phase of the PBG structures for normal plane wave incidence. A single cell of the structure is terminated with periodic boundary conditions (PBC) on four sides to simulate an infinite planar structure for this purpose. A plane wave is launched in the direction normal to the surface and the reflected wave from the structure is recorded to compute the phase of the reflection coefficient. The reflected signal is computed in two steps as shown in Fig. 3.4. First, $E_{inc}(t)$ is computed with PMLs on top and bottom of the computational space (Fig. 3.4a). In the second computation, the bottom PML

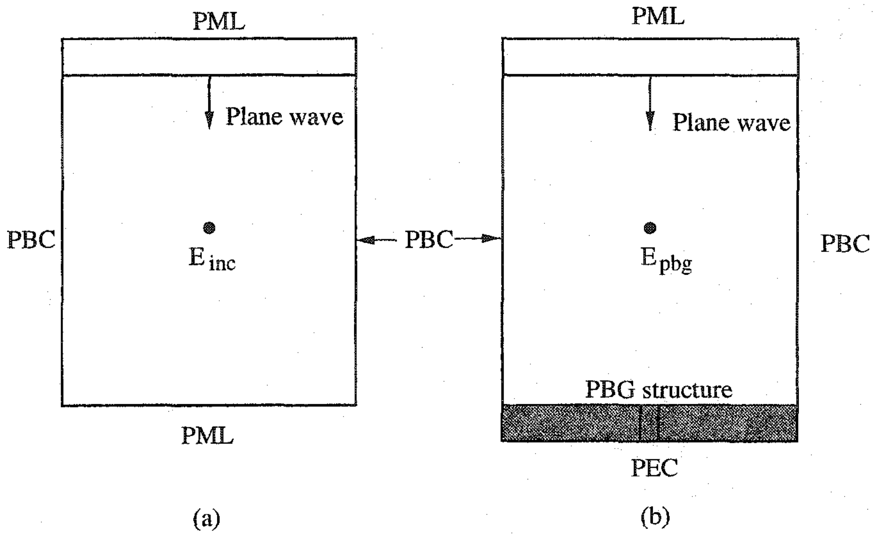

Figure 3.4: Computation of the phase of the reflected signal from the PBG structure
.

is replaced with perfect electric conducting boundary (PEC) and the PBG cell is inserted on the PEC (Fig. 3.4b). The signal $E_{pbg}(t)$ is recorded at the same point as E_{inc} from the second computation. The reflected signal is computed as

$$E_{nref}(t) = E_{pbg}(t) - E_{inc}(t) \tag{3.16}$$

After taking the FT of $E_{nref}(t)$ and $E_{pbg}(t)$, the phase of the reflected signal with respect to the incident signal can be computed as

$$\theta_{nref}(f) = \theta_{pbg}(f) - \theta_{inc}(f) \tag{3.17}$$

For the modeling of shorting pins present in the PBG structures, a thick-wire model has been used (wire cross section is discretized into more than one cell). This is due to the presence of all the 6 components of the fields within the structure.

The thin-wire model that essentially assumes a TM wave (with respect to the wire) yields to weak stability in modeling of these structures. The position of the absorbing boundaries (PMLs) above the surface of the PBG structures has virtually no effect on the reflections from the boundary. However, they have been placed $0.25\lambda - 0.5\lambda$ above the surface of the PBG structures with sufficient number of layers for minimum reflections. For discetization of the computational space, the mesh size is dictated by the size of the elements of the structure rather than the stability criterion.

3.3 Models

One of the main objectives of this research is to design PCS antennas and to investigate the interaction between the antennas and the user's head using numerical analysis. A model of the handset and a biological model of the user's head are therefore needed.

3.3.1 Handset

It has been mentioned in the previous chapter that a small ground plane has a significant effect on the antenna characteristics. For PCS antennas the small metal casing of the handset acts as the ground plane for the antenna. So, it is important to analyze the PCS antennas placed on a realistic model of the handset. A wire grid model of the handset is the simplest of different models that has been used for handset antenna analysis. A solid rectangular metal box is a more accurate model of the handset.

Since it can be easily modeled using the FDTD technique, a rectangular metal box has been used as the model of the handset for this research. Metal boxes of two different sizes are used that are representative of sizes of different commercially available cellular phone sets. They are $126mm \times 46mm \times 26mm$ and $100mm \times 50mm \times 20mm$. To make the handset model more realistic, the metal box is coated with an insulating layer having a permittivity of (ε_r') 2.1 and no dielectric losses. The thickness of the coating is 2mm and 1mm for first and second model, respectively.

3.3.2 Human Head

In terms of macroscopic behavior, a biological body is a volume of lossy dielectric material, and each tissue type has a complex permittivity $\hat{\varepsilon}$:

$$\hat{\varepsilon} = \varepsilon_0(\varepsilon_r' - j\varepsilon_r'') = \varepsilon_0\varepsilon_r' - j\frac{\sigma}{2\pi f} \tag{3.18}$$

where ε_0 is the permittivity of free space (F/m), ε_r' and ε_r'' are the real and imaginary parts of the relative permittivity of the medium, σ is the conductivity (S/m) and f is the frequency (Hz). At a given frequency, the complex permittivity is completely described by ε_r' and σ. Accurate values of ε_r' and σ for human tissue over broad frequency range are available in the literature [84].

Various head models have previously been investigated. These include homogeneous boxes and spheres, and heterogeneous and anatomically based accurate models. Anatomically accurate models are desirable, as spherical models yield overestimated SAR values and box models provide distorted and unreliable results for the antenna far-field pattern [25].

The head model used in this research is based on a model developed at the Radiology Department of Yale University using CT (Computer Topography) and MRI

Table 3.1: Dielectric properties of the tissues in the head model at 835 MHz

Tissue	ε_r'	σ (S/m)	Tissue	ε_r'	σ (S/m)
skin	41.8	0.84	skull	16.7	0.23
spinal cord	32.7	0.56	spine	16.7	0.23
brain-white matter	49.9	1.23	brain-gray matter	32.7	0.56
jaw bone	16.7	0.23	muscle	56.1	0.94
parotid gland	49.9	1.23	lachrymal glands	49.9	1.23
spinal canal	68.8	2.34	tongue	55.5	0.91
pharynx	42.9	0.75	esophagus	42.9	0.75
nasal septum	42.9	0.75	fat	11.4	0.1
blood	61.6	1.51	CSF	68.8	2.38
eye-sclera	55.5	1.14	eye-humor	68.9	1.61
lens	46.7	0.77	bone marrow	61.6	1.51
cartilage	42.9	0.75	pituitary gland	49.9	1.23
ear bones	42.9	0.75	trachea	42.1	0.75

(Magnetic Resonance Imaging) scans [85]. Improvements to the original Yale model have been made at the University of Victoria. Twenty-six different tissue types are identified and their dielectric constant and conductivity values are assigned. As mentioned earlier, to analyze the antenna-head interaction at two frequency bands two sets of permittivity and conductivity values of the tissues are used. Table 3.1 and Table 3.2 show the dielectric properties of different tissues of the head model at 835 MHz and 1900 MHz, respectively. The head model used in this work has a resolution of 1.1 mm and is illustrated in Fig.3.5.

3.4 Verification of SAR Evaluation

In electromagnetic field dosimetry of human exposure to cellular phones, two techniques are currently used: measurements and numerical simulations. Measurements involve evaluating electric field strength in phantom (model) of the head due to op-

Table 3.2: Dielectric properties of the tissues in the head model at 1900 MHz

Tissue	ε'_r	σ (S/m)	Tissue	ε'_r	σ (S/m)
skin	37.2	1.25	skull	16.4	0.45
spinal cord	32.0	0.9	spine	16.4	0.45
brain-white matter	43.2	1.29	brain-gray matter	32.0	0.9
jaw bone	16.4	0.45	muscle	49.4	1.64
parotid gland	43.2	1.29	lachrymal glands	43.2	1.29
spinal canal	77.3	2.55	tongue	49.4	1.64
pharynx	38.1	1.28	esophagus	38.1	1.28
nasal septum	38.1	1.28	fat	9.38	0.92
blood	54.2	2.27	CSF	77.3	2.55
eye-sclera	52.6	1.73	eye-humor	67.1	2.14
lens	42.0	1.15	bone marrow	54.2	2.27
cartilage	38.1	1.28	pituitary gland	43.2	1.29
ear bones	38.1	1.28	trachea	38.1	1.28

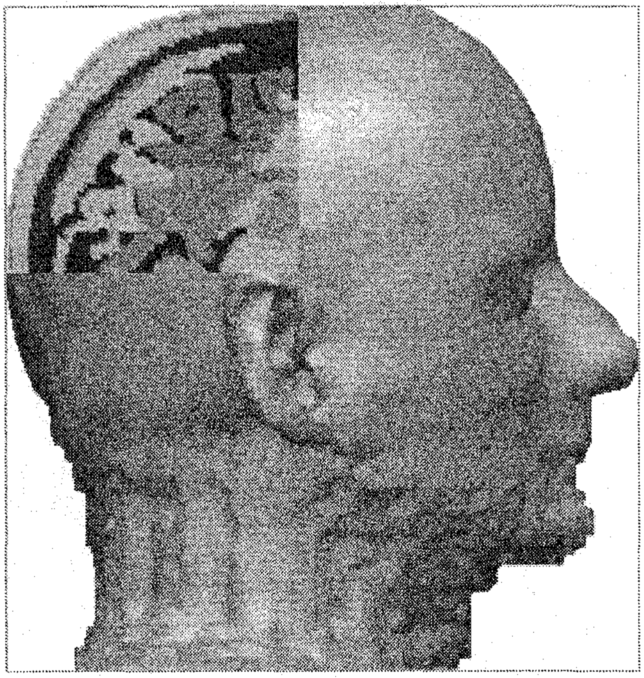

Figure 3.5: Model of the human head (resolution 1.1 mm up to the chin, 3.6 mm below).

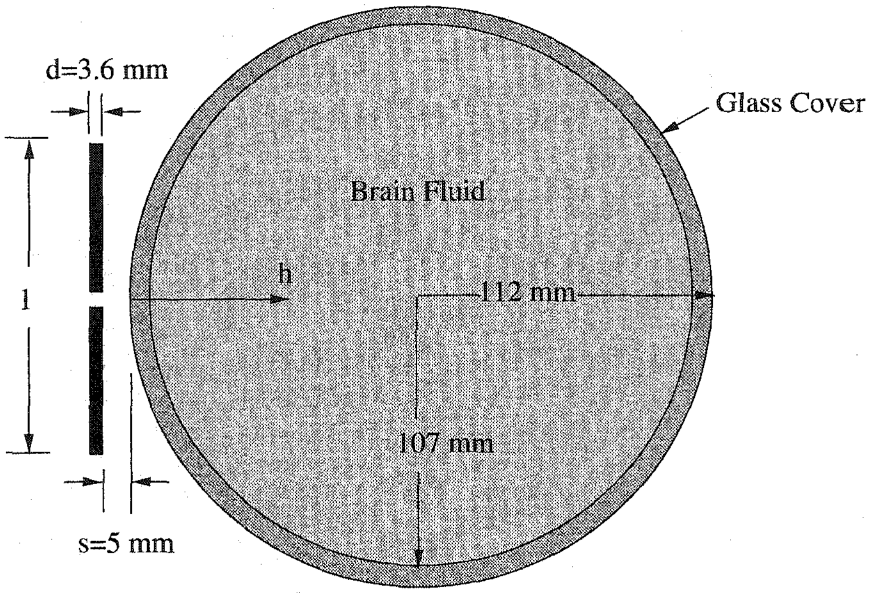

Figure 3.6: Different dimensions of the spherical head model and dipole antenna.

eration of nearby antenna. Numerical simulations, used in this research, compute electric fields and then SAR in a numerical model of a human head. Thus, it is important to establish agreement between these techniques in order to validate the use of numerical simulation for dosimetry purpose.

A simple model has been used in place of the head for comparison between measurements and computations. A spherical flask filled with homogeneous simulated brain fluid material is placed in the near-field of a resonant half-wave dipole operating at cell phone frequencies in North America (i.e. 835 MHz and 1900 MHz). Dimensions of the structure are illustrated in Fig. 3.6. The length of the dipole (l) is 168 mm and 77 mm for 835 MHz and 1900 MHz, respectively. The dielectric properties of the sphere shell and the brain fluid are given in Table 3.3 at the two frequencies of interest.

The FDTD code has been used to model the structure and compute SAR within

Table 3.3: Dielectric properties of the spherical phantom.

Frequency MHz	Brain Fluid		Glass Cover	
	ε_r'	σ (S/m)	ε_r'	σ (S/m)
835	41.1	1.06	4.0	1.0
1900	45.5	1.31	4.0	1.0

the spherical model. The computational space ($260mm \times 247mm \times 247mm$) has been discretized using graded mesh. The grid size ranges from 1 mm near the antenna feed point and within the sphere along the diameter perpendicular to the antenna to 4 mm near the edge of the computational space. PMLs (6 layers, parabolic profile, -50 dB reflection) have been used to truncate the computational space. Antennas have been excited at the center (2 mm gap) with a pulse of center frequency at 1400 MHz and a width of 900 MHz. The numerically evaluated SAR is also compared with the measured SAR obtained by a University of Utah research group.

Fig. 3.7 and Fig. 3.8 show the computed SAR along the diameter of the sphere and perpendicular to the antenna for 835 MHz and 1900 MHz, respectively. The figures also show the measured SAR (dotted line) and compare those with the computed values (solid line). The SARs are normalized to 1.0 W and 0.5 W radiated power from the antenna at 835 MHz and 1900 MHz, respectively.

A good agreement can be observed between the measured and numerically computed SARs. This agreement adds confidence to numerical simulations of handset antennas operating near a head.

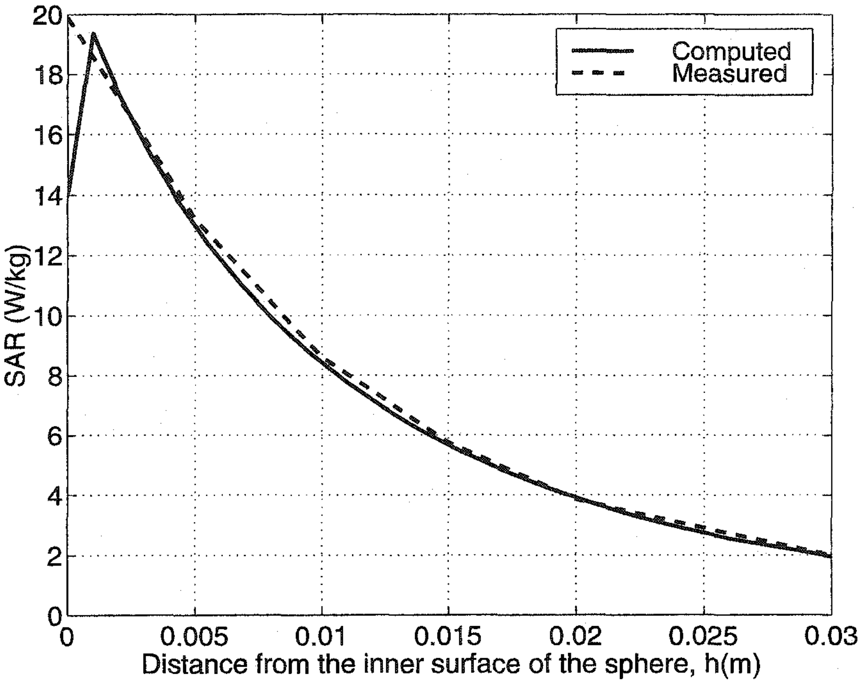

Figure 3.7: Comparison of measured and FDTD computed SARs at 835 MHz. SARs are normalized to a radiated power of 1.0 W.

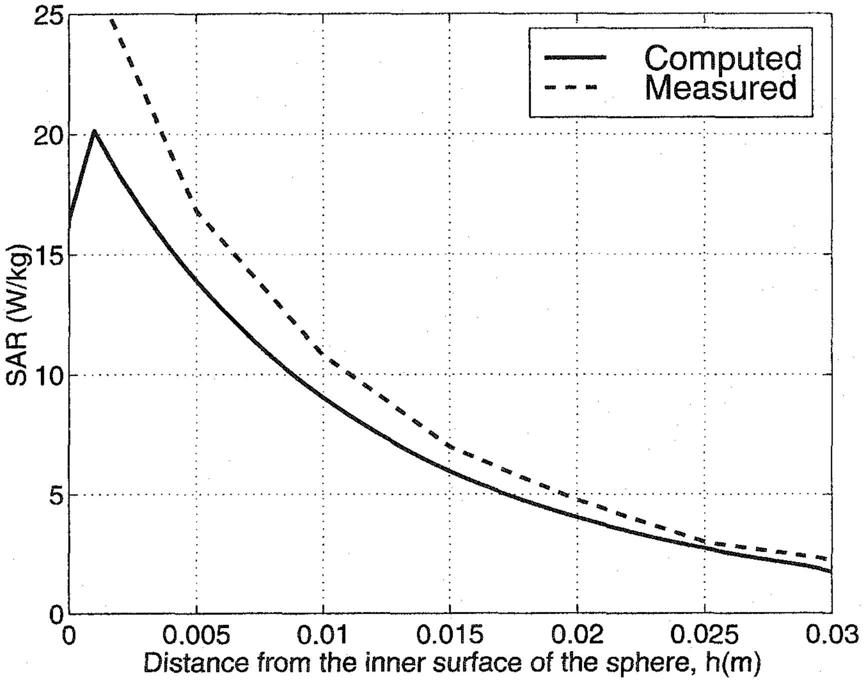

Figure 3.8: Comparison of measured and FDTD computed SARs at 1900 MHz. SARs are normalized to a radiated power of 0.5 W.

Chapter 4

Dual Band Antennas for PCS Handsets

4.1 Introduction

With the widespread use of the hand-held wireless communication system and allocation of the second frequency band, there has been increasing interest in developing dual-band antennas for handheld devices. It has also stimulated increasing interest in the electromagnetic interaction between the antenna and the user. Of interest are the influence of the close proximity of the user's head on the antenna performance, the potential health effects of the radio frequency (RF) fields absorbed in the user's head and compliance of the hand-held devices with existing safety standards. These issues must be addressed while also ensuring that the handset antenna is small enough to be used on a handset and has sufficient gain, bandwidth and efficiency.

In this chapter, the FDTD technique is used to design and analyze two dual band antennas for a handset at frequencies near 835 MHz and 1900 MHz. The research develops the dual band antennas and investigates the interactions between the antennas and the user. The antennas are a sleeve-monopole and a dual meander-sleeve. The antenna modeling incorporates the antenna, a cellular telephone handset and a biological model of the user's head. Performance of the antennas is evaluated in terms of impedance bandwidths, far-field radiation patterns, and the SAR in the user's body. The results reported here have already been published in [86] and [87].

4.2 Description of the Antennas

A monopole antenna is one of the most popular and widely used antennas for handheld telephones. Its popularity is due to its attractive bandwidth and radiation characteristics even in the proximity of the user. However, it operates in one frequency band only. Dual-band operation can be achieved by adding parasitic elements to it. An analytical study by King [88] describes the dual band operation of a sleeve dipole. In addition to the second resonance frequency, the sleeve dipole provides broad impedance bandwidth. Another advantage of this antenna is its capability to operate over a frequency range of 4:1 with minimal change in the radiation pattern. Considering the open-sleeve dipole configuration described by King and Wong [89], in this work two thin metal strips have been used as sleeves (parasitic elements) to obtain the second operating frequency. The sleeves are placed on both sides of the monopole and mounted on the top center of the handset model (described in 3.3.1). The external view of the sleeve-monopole antenna and the handset is shown in Fig. 4.1(a). The antenna elements are modeled with thin metal strips of width w. Other parameters of the strip-sleeve monopole, illustrated in Fig 4.1(b), are monopole length, L, sleeve length, l, and sleeve spacing, S.

The dual-meander antenna described in [90] provides similar characteristics as those of monopole antenna but with reduced height and wider bandwidth. A dual-

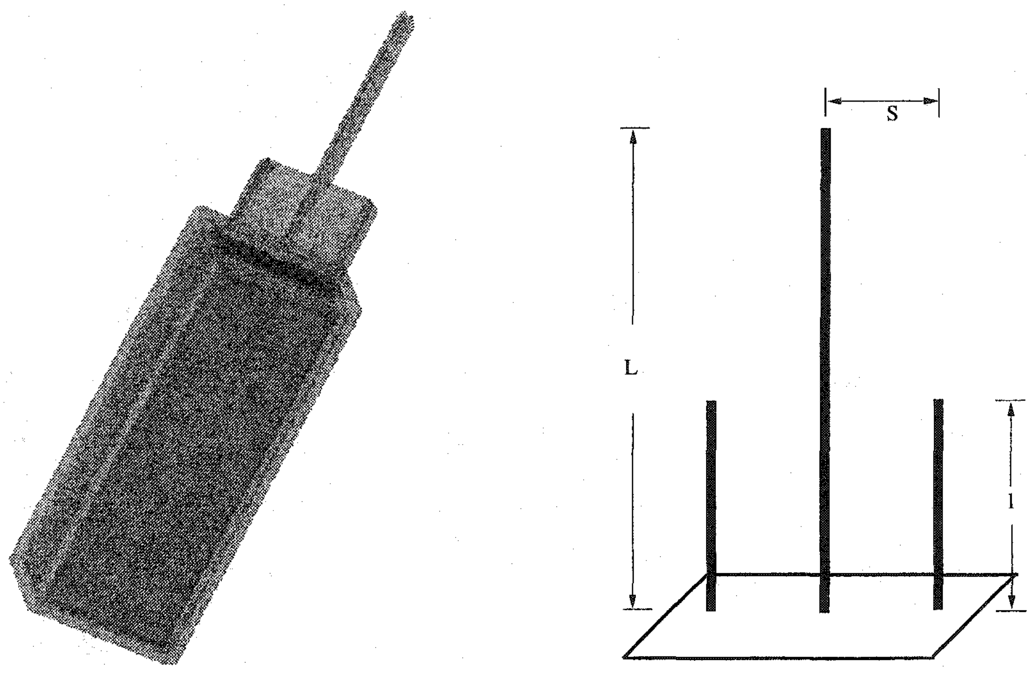

(a) (b)

Figure 4.1: Sleeve-monopole antenna and the handset: (a) external view, and (b) different dimensions of the antenna.

meander antenna can also be designed to operate in two frequency bands by adding sleeves to it. Thus, the dual-meander antenna with sleeves offers some advantages over sleeve-monopole antenna. Recently, a dual-meander antenna with sleeves over an infinite ground plane has been analyzed for vehicular applications [74]. The design has to be modified from that on the infinite ground plane to be used for handheld telephones. In the present research, a dual-meander antenna has been designed and analyzed for handheld telephones. The antenna elements have been modeled using thin metal strips of width w. The parameters of the dual-band meander antenna shown in Fig. 4.2(a) are: $b1$, $b2$, d, antenna length L, number of dual meander sections N, sleeve length, l, and sleeve spacing, S. The antenna has been analyzed for two different positions (center and edge) on the handset as shown in Fig. 4.2(b).

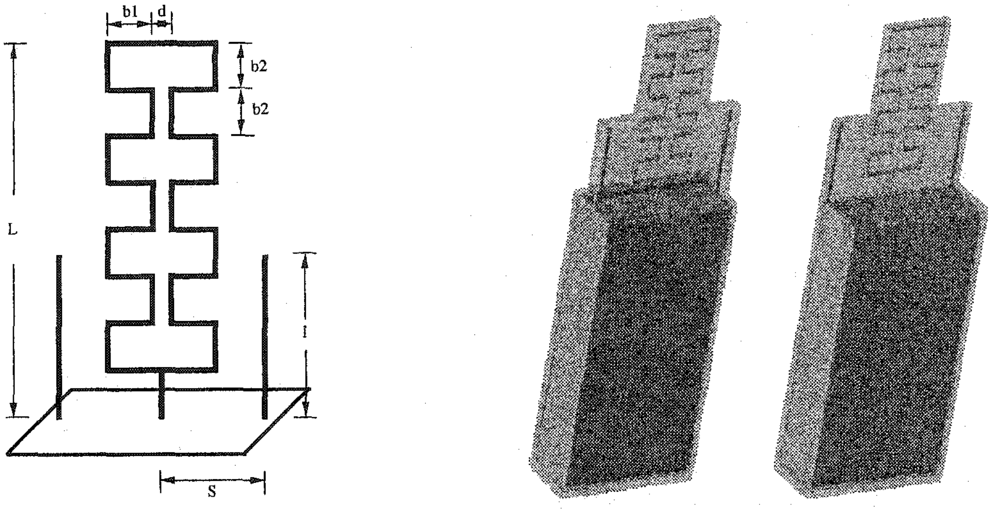

(a)

(b)

Figure 4.2: Dual-meander antenna with sleeves and the handset: (b) different dimensions of the antenna, and (a) external view for two different positions of the antenna on the handset.

Both the sleeve-monopole and the dual-meander sleeve antenna have been printed on a dielectric substrate ($\varepsilon_r = 2.1$) of 2 mm thickness and covered with another layer of the same dielectric material of the same thickness. The different parameters of the antennas are obtained by numerical simulations to get the dual-frequency operation in the desired bands (e.g. AMPS and PCS).

4.3 Modeling Configurations

The FDTD code has been used for the design and analysis of the antennas. The computational space is truncated with PMLs of 7 layers, parabolic profile, and -60 dB reflections for both antennas. A uniform grid with a cubic Yee cell of 2 mm is used for the analysis of the sleeve-monopole antenna, while a graded mesh is used to model the small dimensions of the dual-meander antenna. The grid size ranges from the finest resolution of 0.5 mm to the most coarse of 7 mm and gradual change with

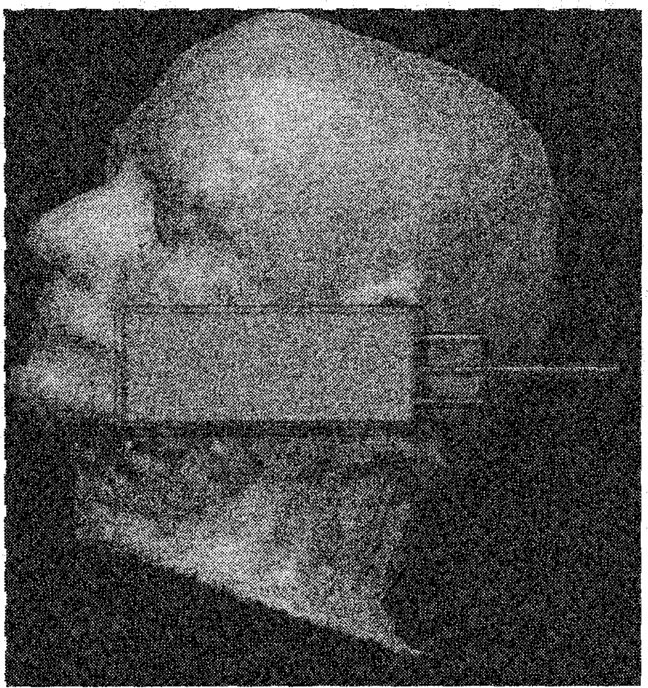

Figure 4.3: Orientation of the handset with respect to the user's head.

a ratio of 1:1.2. The antennas are excited from a 50 Ω source using a Gaussian pulse centered at 1.4 GHz and a bandwidth of 1.2 GHz. For analyzing the antennas in the presence of the user's head, the handset has been placed in a realistic use position touching the user's cheek as shown in Fig. 4.3. Due to the fact that the resolution of the head model (1.1 mm) and the Yee cells are not equal, a dielectric averaging algorithm has been used to convert the head model to the Yee cell resolution. The number of simulation time steps has been 1800 to 2000 to ensure that the pulse amplitude had decayed to a small fraction of its peak value.

4.4 Results

4.4.1 Antenna Design

Sleeve-Monopole Antenna: The different antenna dimensions shown in Fig. 4.1 are given in Table 4.1. The width of the metal strips (w) for the sleeve-monopole antenna has been taken as $2mm$. The length of the monopole (L), length of the sleeves (l), and the spacing between the sleeves (S) are selected to get the antenna operation in the 824-894 MHz (AMPS) and 1.85-1.99 GHz (PCS) frequency bands with a VSWR below 1.5 with respect to 50Ω input impedance. To obtain the optimum antenna dimensions two parametric studies are performed. Namely, the effect of sleeve length and the effect of sleeve spacing has been investigated. The monopole length is selected as $L = 90mm$ to get the first operating frequency near 900 MHz ($\approx \lambda/4$). Fig. 4.4(a) shows the effect of sleeve spacing on the antenna input impedance. The sleeve spacing is varied from $14mm$ to $22mm$ in $2mm$ increments, with a constant sleeve height of $30mm$. It can be observed that the third resonant frequency increases as the spacing increases while the first resonance remains almost constant. The input resistance near the first resonance remains constant at 50Ω while near the third resonant frequency it increases as the sleeve spacing increases. The effect of the sleeve length on the input impedance is shown in Fig. 4.4(b). The sleeve length has little effect on the first resonant frequency and the input resistance near the first resonance. However, the input resistance near the third resonance increases as the length increases. A decrease in the third resonant frequency is also observed as the sleeve height increases. However, this trend is discontinued when l becomes greater than $L/3$. This actually effects the VSWR bandwidth in the higher frequency band. Therefore, based on Fig.

Table 4.1: Antenna dimensions for Sleeve-Monopole antenna (See also Fig. 4.1).

Design	Strip Width, w(mm)	Monopole Length, L(mm)	Sleeve Length, l(mm)	Sleeve Spacing, S(mm)
Initial	2	90	28	14
Final	2	90	30	18

4.4, optimum dimensions of the sleeve-monopole antenna are selected as: monopol length $L = 90mm$, sleeve length $l = 30mm$, and sleeve spacing $S = 18mm$ and show in Table 4.1.

Dual-Meander-Sleeve Antenna: Table 4.2 shows the different dimensions of th antenna illustrated in Fig. 4.2. The dual-meander monopole and the sleeves ha been implemented as a $1mm$ wide strip line. The parameters of the dual-meande monopole is taken as length $L = 64mm$, number of sections $N = 4$, $d = 5mm$ and $b1 = b2 = 8mm$ to get the first operating frequency near 900 MHz [74]. Thu this antenna is 30% shorter than the monopole of the sleeve-monopole antenna. I can be mentioned here that the length of the dual-meander monopole can be furthe reduced by increasing the number of meander sections and increasing the dimensio $b1$. However, each increment in $b1$ makes the antenna wider. The second operatin frequency could be achieved by changing the sleeve lengths and their separation fro the meander. The effect of the sleeve dimensions on the antenna operating frequencie are similar to those for sleeve-monopole antenna discussed above. To retain have bee performed by simultaneously changing the l and S. The optimum values of the sleev dimensions are shown in Table 4.2 ($l = 31mm$ and $S = 24mm$) for both positions o the antenna on the handset.

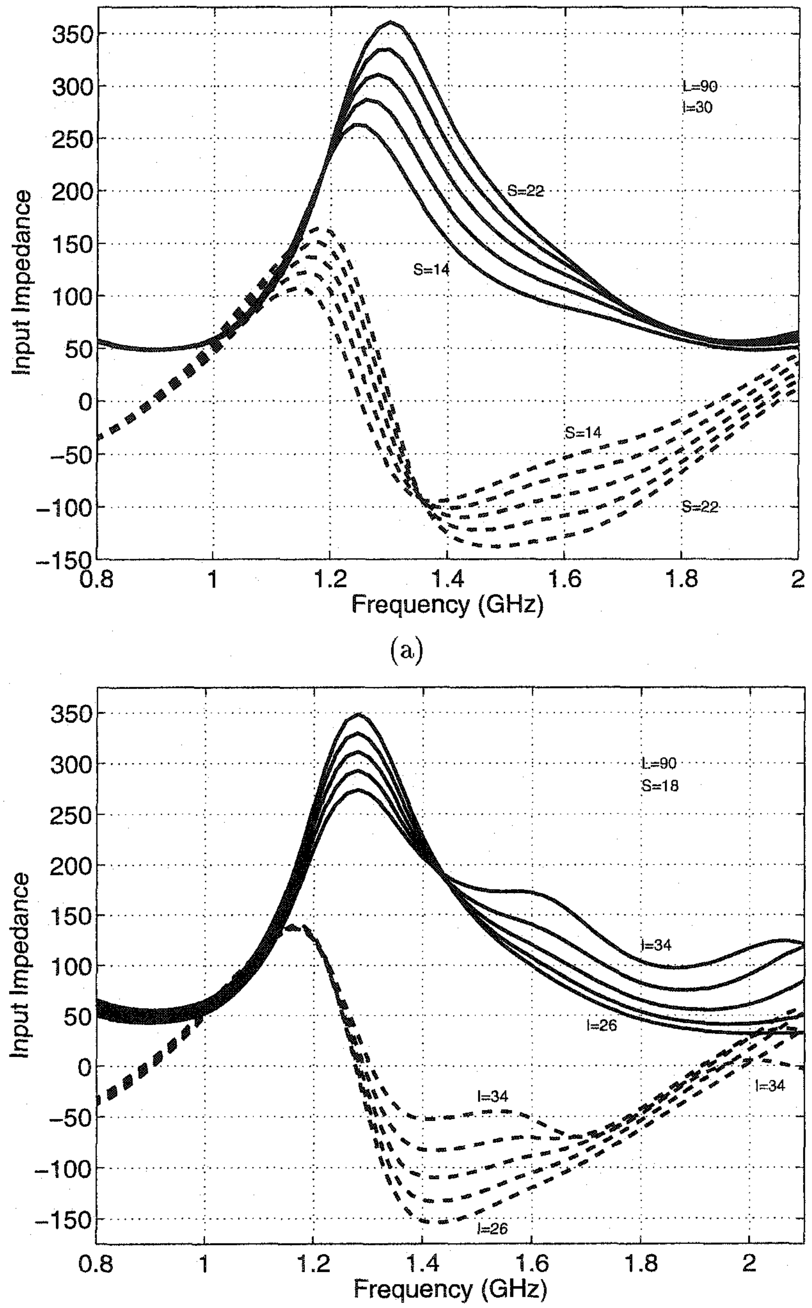

(a)

(b)

Figure 4.4: Parametric studies of the sleeve-monopole antenna parameters on its input impedance. (solid line: resistance, dashed line: reactance). (a) Effect of sleeve spacing. $l = 30mm$ constant, separation s varied from $14mm$ to $22mm$. (b) Effect of sleeve length. Separation $S = 18mm$ constant, length varied from $26mm$ to $34mm$.

Table 4.2: Antenna dimensions for a Dual-Meander-Sleeve antenna for both positions on the handset (See also Fig. 4.2).

Design	Strip Width, w(mm)	Meander Height, L (mm)	Meander Parameters			Sleeve Length, l(mm)	Sleeve Spacing, S(mm)
			N(mm)	d(mm)	b1=b2(mm)		
Initial	1	64	4	5	8	28	14
Final	1	64	4	5	8	31	24

4.4.2 Antenna Characteristics

Sleeve-Monopole Antenna: Fig. 4.5 and 4.6 show the input impedance and VSWR of the antenna, respectively. The characteristics are shown as a function of frequency in free space (solid line) and in the proximity of the user's head (dashed line). The resonant frequencies are 0.910 and 1.911 GHz in free space. The resonant resistances at these two frequencies are close to 50 Ω. The bandwidths with VSWR $\leq$ 2 are 172 MHz (800-972 MHz, 19.3%), and 216MHz (1811-2027 MHz, 11.2%) in free space. It can be observed from Fig. 4.6 that the bandwidth in both bands increases due to the presence of the user's head. Also, the lower resonance frequency decreases, but the higher resonance frequency remains almost the same.

The radiation patterns of the antenna at resonant frequencies in E and H principal planes and are shown in Fig. 4.7 and 4.8, respectively. Patterns are normalized to the maximum field. When the E plane patterns in free space (solid lines) are considered, it can be observed that the antenna radiates more power below the horizon for both frequencies. It is well known, that the radiation pattern of an antenna mounted on a handset resembles that of a dipole, as the current flow on the handset makes the antenna behave as an asymmetric dipole [8]. The H-plane patterns in free space

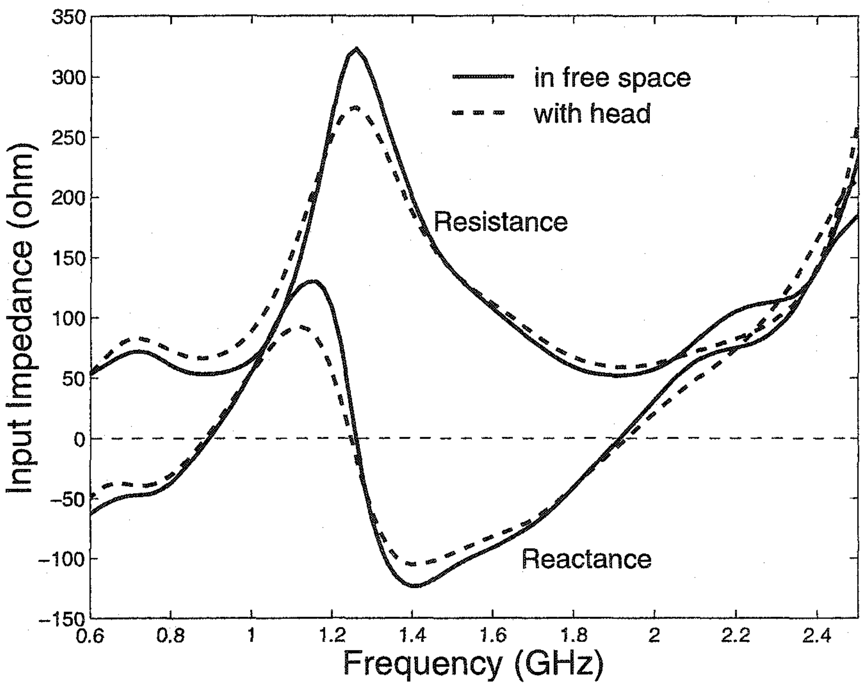

Figure 4.5: Input impedance of the sleeve-monopole with and without the presence of user's head.

(solid lines) are omnidirectional as for conventional monopoles. Significant changes can be noted in the radiation patterns in both frequency bands due to the presence of the user's head. In the H-plane the antenna loses its omnidirectional characteristics (dotted lines) due to the presence of the user's head. The patterns in the E-plane also become asymmetric and a dip can be observed at $\theta \approx 140^0$. This is due to the power absorbed in the user's head. This effect is typical for practically all linear antennas on handsets [25], [27].

Dual-Meander-Sleeve Antenna: Fig. 4.9 shows the VSWR characteristics for the two antenna locations considered. The figures show the characteristics both in free space and in the user's proximity. It can be noted that, in all cases, the VSWR is less than 1.5. Both the *E-plane* and *H-plane* radiation patterns of the dual-meander-sleeve antenna are similar to the sleeve-monopole antenna. So, the dual-meander-

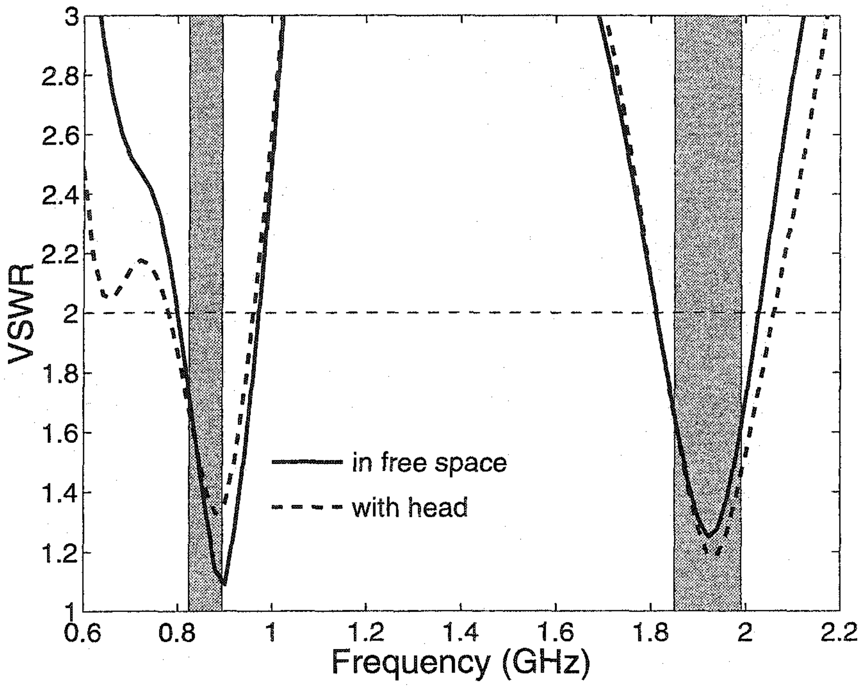

Figure 4.6: VSWR characteristics of sleeve-monopole with and without the presence of user's head.

sleeve antenna provides better VSWR bandwidth than the sleeve-monopole antenna without affecting the other characteristics. Also, the matching of this antenna is superior to the sleeve-monopole antenna.

4.4.3 SAR

The SAR, power absorbed per unit mass of tissue, is normalized to the antenna output power of 1 W for both frequency bands. The maximum SARs for both antennas are shown in Table 4.3.

For compliance, the maximum 1g SAR should be within the U.S. Federation of Communication Commission (FCC) [79] prescribed safe limit. According to FCC 1g SAR should be less than 1.6 W/kg for maximum output power from the antenna.

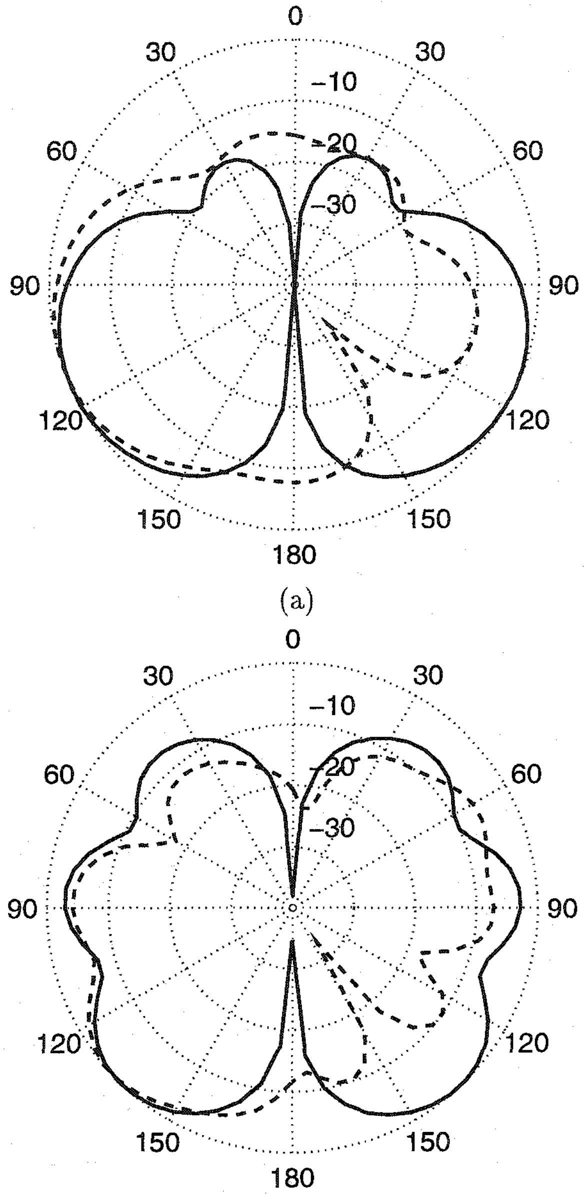

(a)

(b)

Figure 4.7: E-plane radiation patterns of the sleeve-monopole (solid line: in free space, dashed line: in presence of the user), (a) at the lower resonant frequency, and (b) at the higher resonant frequency.

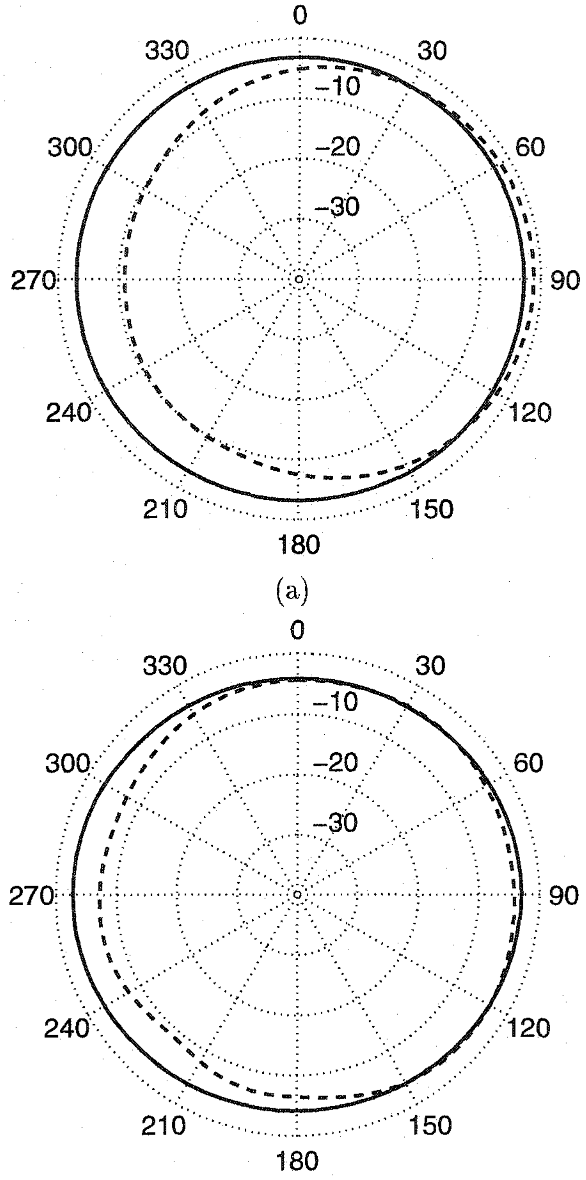

(a)

(b)

Figure 4.8: H-plane radiation patterns of the sleeve-monopole (solid line: in free space, dashed line: in presence of the user), (a) at the lower resonant frequency, and (b) at the higher resonant frequency.

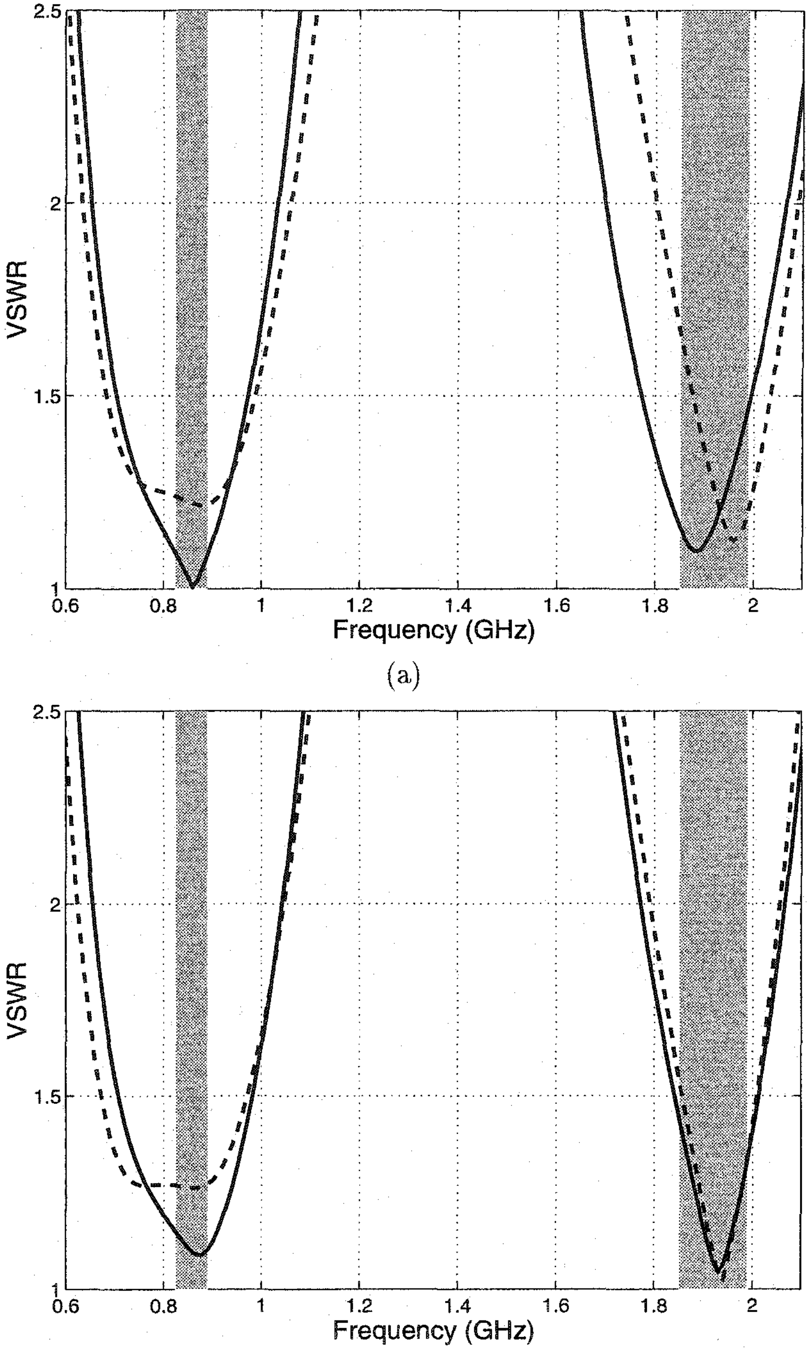

(a)

(b)

Figure 4.9: VSWR characteristics of the dual-meander-sleeve antenna in two positions on the handset (solid line: in free space, dashed line: in presence of the user). Gray areas show the allocated bandwidth. (a) Antenna at the center of the box. (b) Antenna in the edge of the box.

Table 4.3: Specific Absorption Rates (SAR) of the designed antennas normalized to 1 W.

Antenna	Frequency MHz	SAR (1g) W/kg
Sleeve-monopole	840	2.6
	1900	3.3
Meander-sleeve	840	2.3
	1900	2.2

Table 4.4: Specific Absorption Rates (SAR) of the designed antennas normalized to maximum typical output power.

Antenna	Frequency MHz	SAR (1g) W/kg
Sleeve-monopole	840	1.5
	1900	0.41
Meander-sleeve	840	1.4
	1900	0.28

The maximum output power for the handset antennas is 0.6 W and 0.125 W for the AMPS and PCS band, respectively. Table 4.4 shows the peak 1g SARs normalized to the maximum output power of the antenna. It can be observed that SARs are within the FCC prescribed safe limit.

4.5 Conclusions

Both dual-band antennas provide a viable option for use in mobile telephones. The new antennas operate in AMPS (824-894 MHz) and PCS (1850-1990 MHz) bands with sufficient bandwidths (VSWR ≤ 2) with single feed. The antennas also provide satisfactory dual-band operation in the presence of the user's head. Power absorbed in the user's head (SAR) is also within the FCC prescribed safe limit. The radiation patterns of both the antennas are satisfactory for practical communication environment.

Furthermore, the dual-meander-sleeve antenna is shorter than the sleeve-monopole antenna with lower VSWR in free space and with the user's head in the close proximity. The overall performance of the meander-sleeve antenna varies minimally with different positions of the antenna on the top of the telephone case. In summary, these new antennas achieved satisfactory performance in two frequency bands with their properties similar or superior to those of ordinary monopoles.

Chapter 5

Broad Band Patch Antennas

5.1 Introduction

As cellular telephones and other PCS devices have become smaller and more portable, the demand for microstrip antennas has increased. In addition to their low profile and compact size, microstrip antennas can produce the necessary circular polarization for satellite communications. However, their polarization bandwidth is even narrower than the impedance bandwidth.

In this chapter, two microstrip antennas are described that provide wide impedance bandwidth along with circular polarization. The proposed antennas are fed by one element and use the multiple resonance technique for bandwidth increment. Therefore, the volume or surface area of the radiating structure is not increased. Antenna characteristics are analyzed using two different numerical techniques and compared with those of a standard patch with similar dimensions. Part of this work has already been published [91].

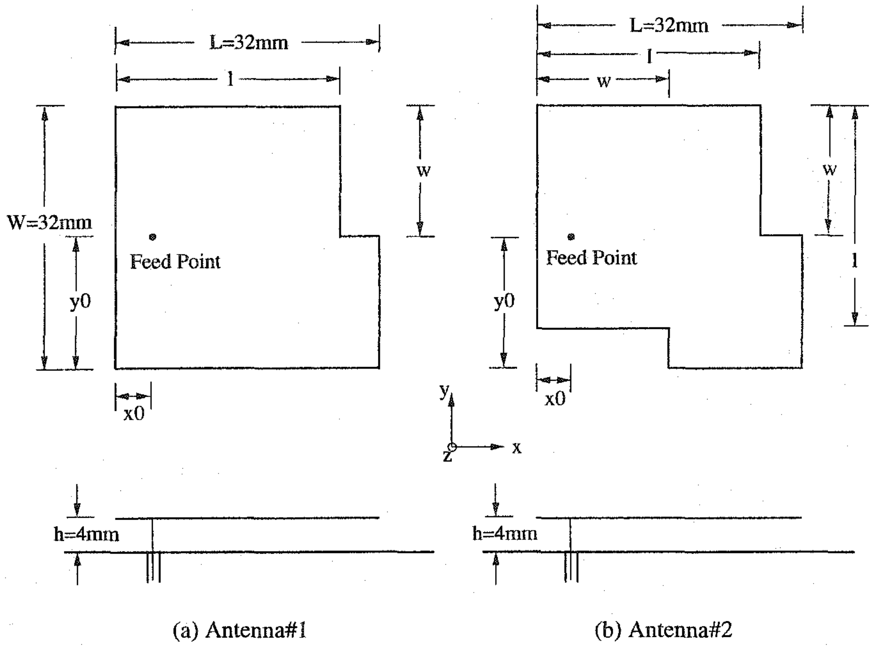

(a) Antenna#1 (b) Antenna#2

Figure 5.1: Dimensions of the modified square patch antennas.

5.2 Antenna Design and Analysis

The antennas have been analyzed initially with the FDTD code. The computational space is truncated with PMLs (8,P, -50dB) and discretized with 1mm cubic Yee cells. The coaxial feed probe is modeled as a finite thickness wire of 0.8 mm diameter with a 50 Ω impedance gap excitation at the base (as explained in more detail in Section 3.2.)

A square patch with an arbitrary size and height is modified to get two closely spaced resonances, as shown in Fig. 5.1. The dimensions of the square patch are $32mm \times 32mm \times 4mm$. The modified patches are fed with a coaxial cable and the resonant cavity is filled with air for the initial analysis. These modified patches resonate at two closely spaced frequencies (f_{r1}, f_{r2}).

Several parameters, namely l, w and the position of the feed point (x_0, y_0) of the proposed antennas, have a strong influence on their input impedance. The effects of these parameters on the input resistance for antenna #1 (Fig. 5.1a) are shown in Fig. 5.2. The peaks in input resistance indicate the resonances. It can be noted that if the feed point is shifted towards the longer side of the patch, it has one resonance at a higher frequency, and if it is shifted towards the shorter side, the patch resonates at a lower frequency. A decrease in length l moves the two resonant frequencies apart, and an increase tends to blend the two resonances together and close to the resonant frequency of the square patch . When w increases, f_{r1} remains constant, but f_{r2} increases. Also, the input resistance at f_{r1} decreases, whereas at f_{r2} it increases.

Within the range of parameters investigated the optimal design has $l = 26mm, w = 18mm, y_0 = 18mm$ and $x_0 = 2mm$ (Table 5.1). The probe location x_0 is selected to match the input resistance with the feed line of 50Ω. However, the reactance of the modified patch is high near the resonance frequencies due to the coaxial feed. The same phenomenon is also observed for the standard square patch. A capacitive feed [35] is used to obtain zero input reactance at the resonance frequencies. A square metal sheet of $8mm \times 8mm$ is attached to the inner conductor of the coaxial line and placed below the patch with a gap of $1mm$ between them. The VSWR of the modified patch and the square patch is compared in Fig. 5.3.

The radiation patterns of the antenna for both resonant frequencies in xz and yz planes are shown in Fig. 5.4. At both frequencies there are both E_θ and E_ϕ in both planes. At the higher resonant frequency E_θ is dominant in the xz-plane and E_ϕ is dominant in the yz-plane. At lower resonance frequency E_θ is dominant in the yz-plane and E_ϕ is dominant in the xz-plane. This indicates that all four edges of the patch are radiating and the TM_{01} and TM_{10} cavity modes are excited. This is

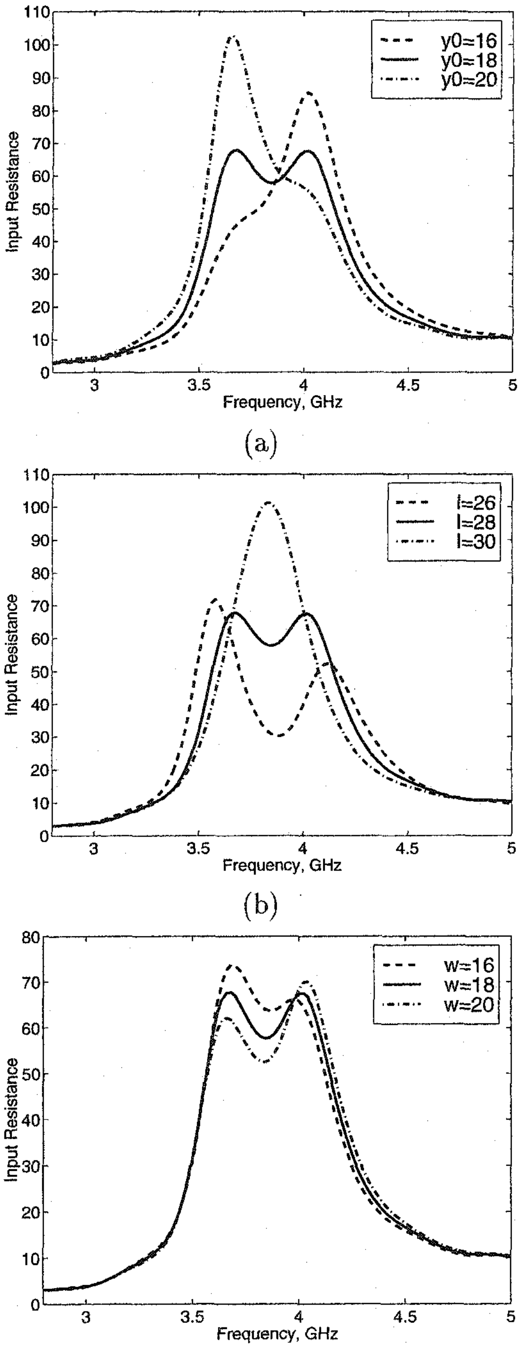

(a)

(b)

(c)

Figure 5.2: Effect of different parameters of the modified patch (antenna#1) on its input resistance: (a) Position of the feed point, y_0, withx_0=6 mm, w=14 mm, l=28 mm (b) Length of the shorter side, l, with x_0=6 mm, y_0=18 mm, w=14 mm, and (c) Width of the shorter side, w, with x_0=6 mm, y_0=18 mm, l=28 mm.

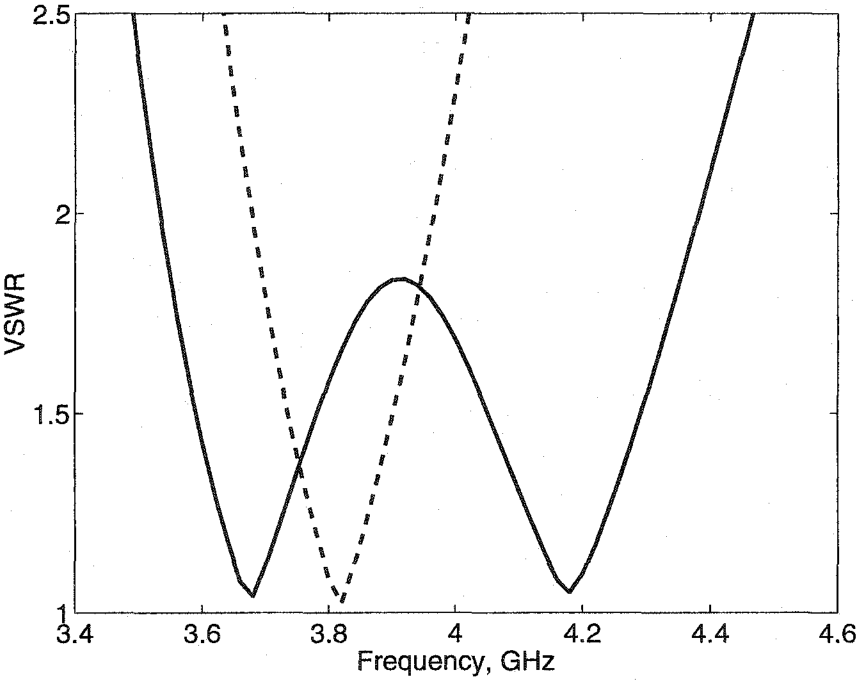

Figure 5.3: VSWR characteristics of the modified patch (antenna#1)(solid line) compared with standard square patch (dotted line).

further illustrated in Fig. 5.5, which shows the E_z under the patch at two resonant frequencies.

The excitation of both TM_{01} and TM_{10} modes may be beneficial for the reception of circularly polarized waves. For circular polarization the axial ratio of the radiated field should be 0 dB. To improve the AR a narrow slot is cut on the patch along the y-axis 14 mm from the left edge with the dimensions of $3mm \times 20mm$ to perturb the current distribution on the patch. With this modification, both the E_θ and E_ϕ are equally dominant in both principal planes for both frequencies as shown in Fig. 5.6. The E_z distribution under the patch for both frequencies resembles that of a diagonally fed square patch; i.e. both TM_{01} and TM_{10} modes are excited (Fig. 5.7). To verify the circular polarization property of the antenna, polarization loss factor

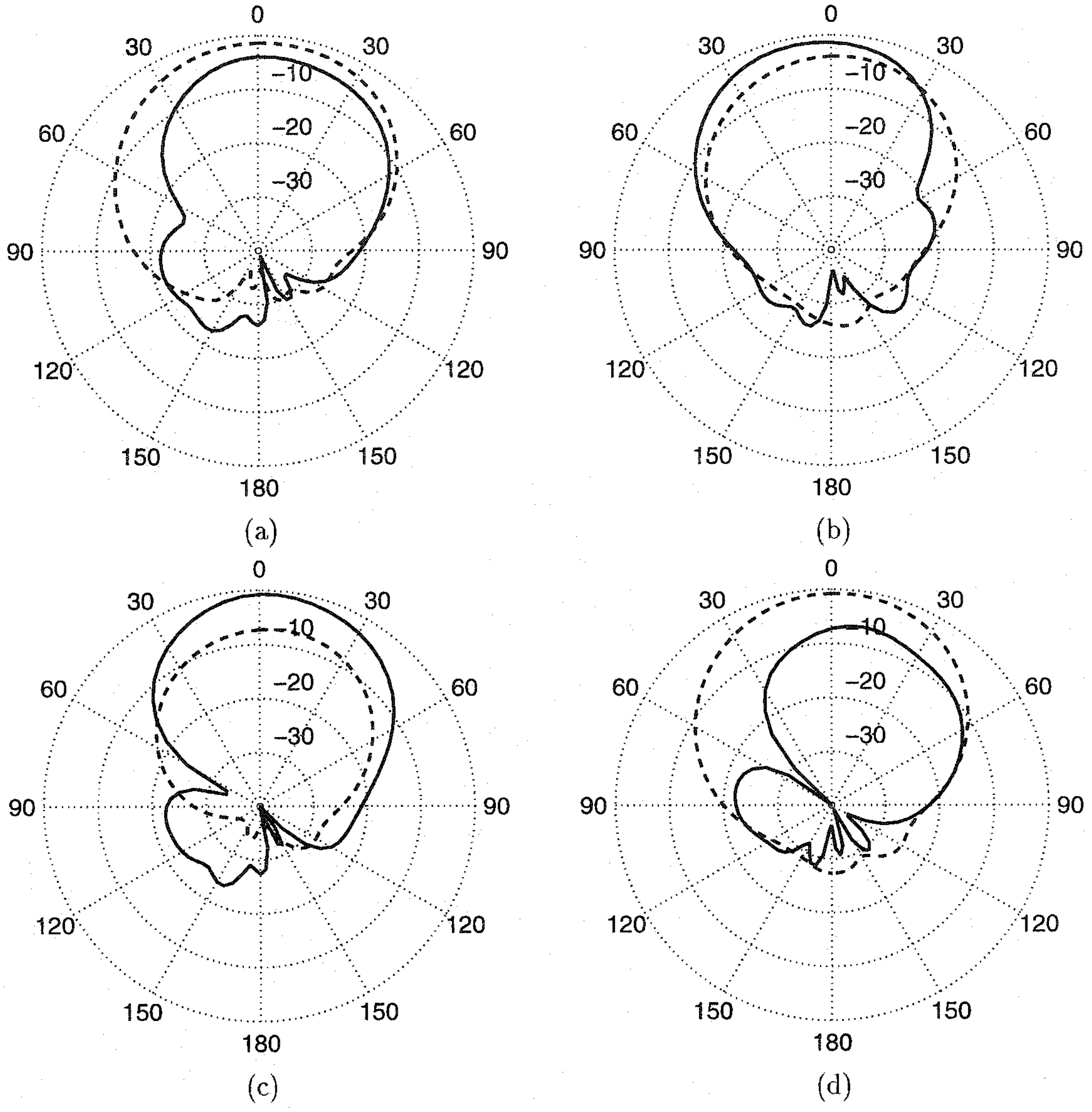

(a) (b) (c) (d)

Figure 5.4: Radiation patterns E_θ (solid line) and E_ϕ (dotted line) of the modified patch (antenna#1): (a) & (b) at the lower resonant frequency in xz and yz plane, respectively, and (c) & (d) at the higher resonant frequency in xz and yz plane, respectively.

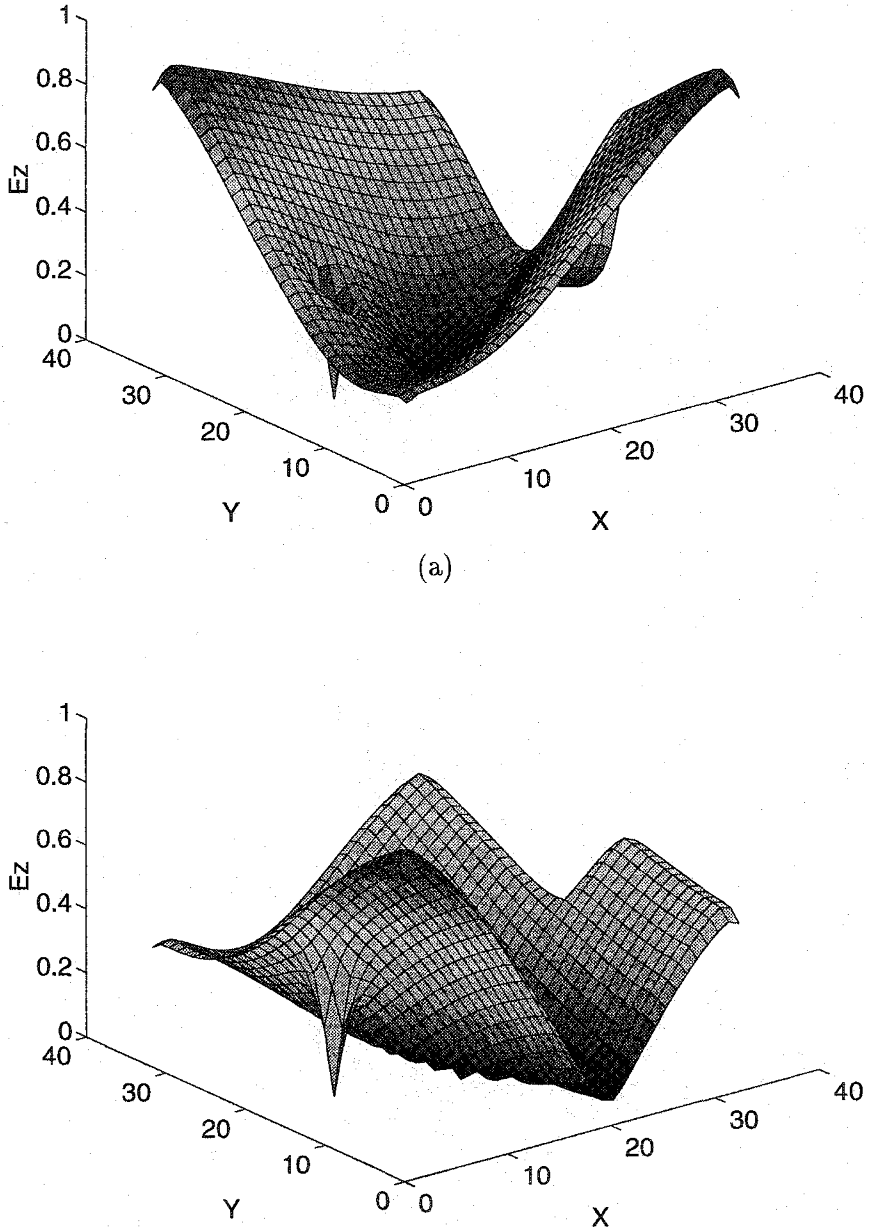

(a)

(b)

Figure 5.5: E_z field pattern under the modified patch (antenna#1): (a) Lower resonant frequency, and (b) Higher resonant frequency.

(PLF) is calculated for an incident RCP wave and shown in Fig. 5.8. PLF$\leq$1.5 dB within 3 dB beamwidth ($\theta = 40^0$) and PLF$\leq$3 within 10 dB beamwidth ($\theta = 60^0$) can be observed. This indicates that the antenna has a reasonably low PLF with omnidirectional radiation pattern within the main radiation region for both resonant frequencies.

The modified square patch of Fig. 5.1(a) (Antenna#1) produces orthogonal modes with unequal amplitudes. This antenna can be further modified, as shown in Fig. 5.1(b) (Antenna#2), to produce orthogonal modes with equal amplitudes. Essential dimensions of antenna #2 have similar effects on its input impedance as those of antenna #1. The optimal dimensions of the second antenna have been found as $l = 28mm, w = 16mm, y_0 = 16mm$ and $x_0 = 1mm$ (Table 5.1). The high input inductance at resonant frequencies is compensated with capacitive feed technique. Antenna #2 provides similar VSWR characteristic to antenna #1 (Fig. 5.9) with a wide input impedance bandwidth. The axial ratio and the PLF are also calculated for antenna #2 for different frequencies and shown in Fig. 5.10. For most of the applications the maximum acceptable axial ratio is less than 6 dB. It is observed that for both the antennas the 6 dB axial ratio bandwidth is much narrower than the impedance bandwidth. This is true for all circularly polarized antennas. It is also observed that the amplitude ratio of the radiated fields ($|E_\theta/E_\phi|$) is 1 at the resonant frequencies and increases at other frequencies. On the other hand, the phase difference of 90^0 occurs between them at the midband frequency (between the two resonant frequencies). Thus, the AR and PLF can be improved along with VSWR in the midband region by increasing l. That brings the two resonant frequencies closer to the midband frequency. This can be achieved only at the expanse of reduced

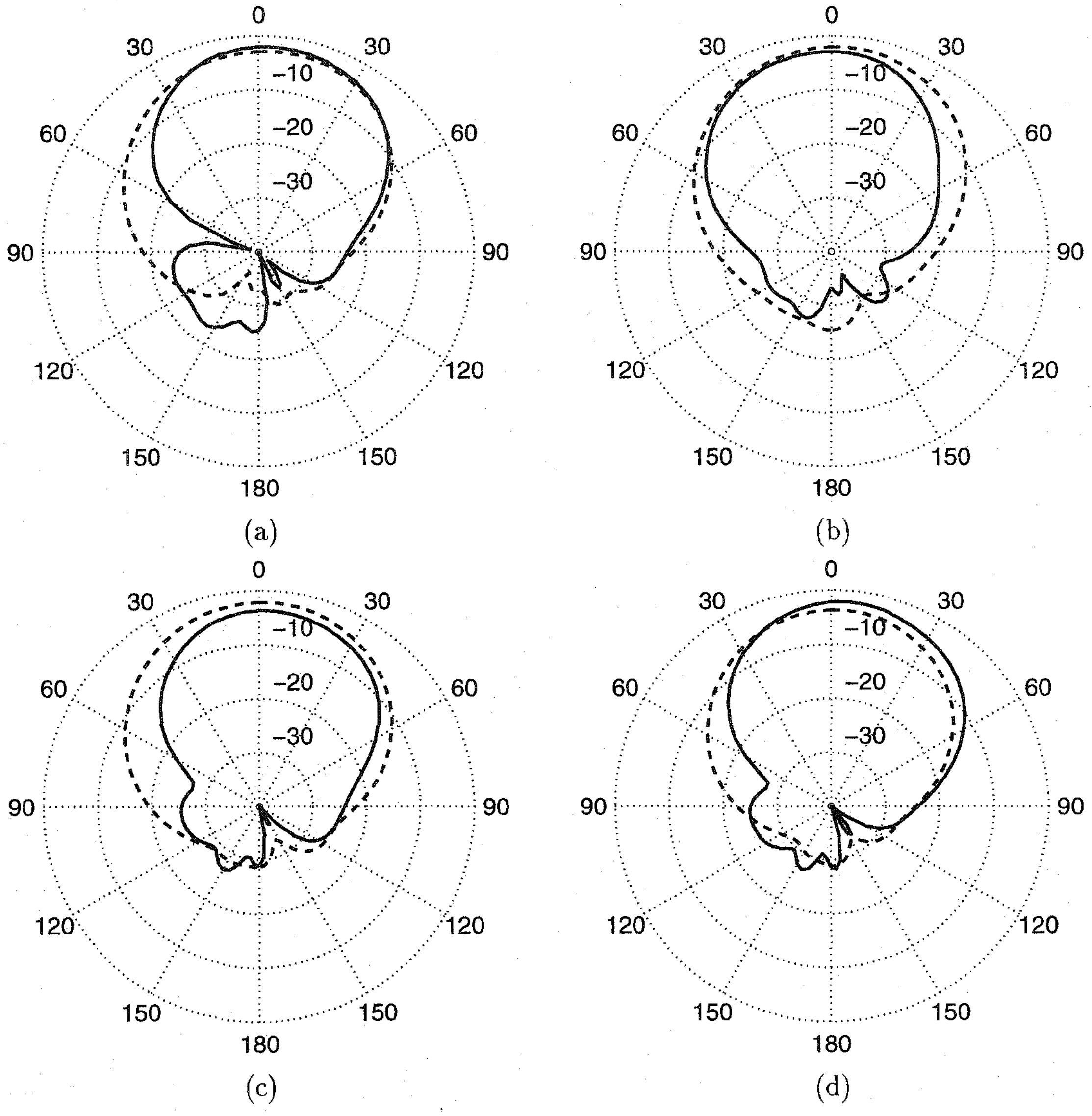

(a) (b) (c) (d)

Figure 5.6: Radiation patterns E_θ (solid line) and E_ϕ (dotted line) of the slot loaded modified patch (antenna#1): (a) & (b) at the lower resonant frequency in xz and yz plane, respectively, and (c) & (d) at the higher resonant frequency in xz and yz plane respectively.

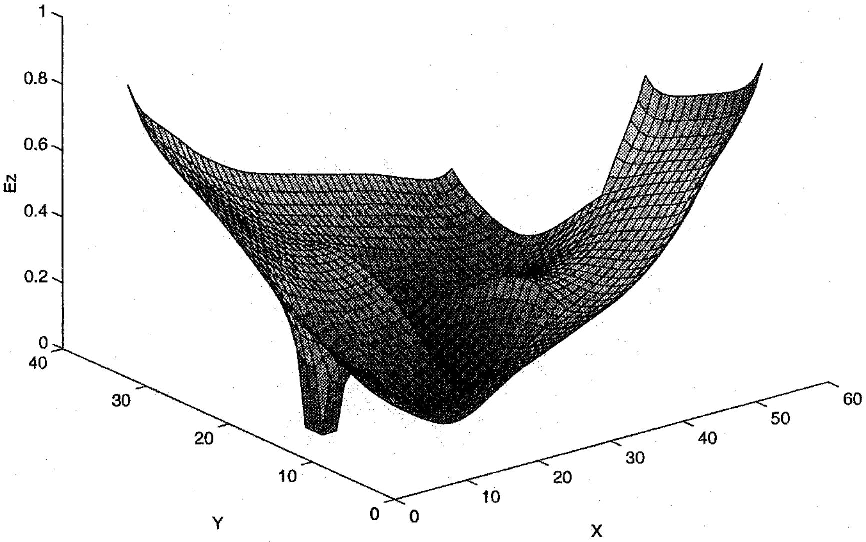

(a)

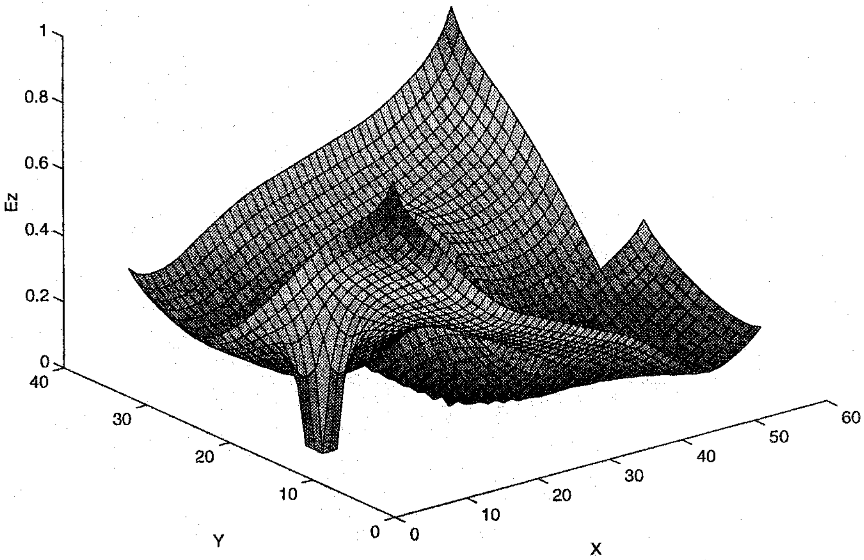

(b)

Figure 5.7: E_z field pattern under the slot loaded modified patch (antenna#1): (a) Lower resonant frequency, and (b) Higher resonant frequency.

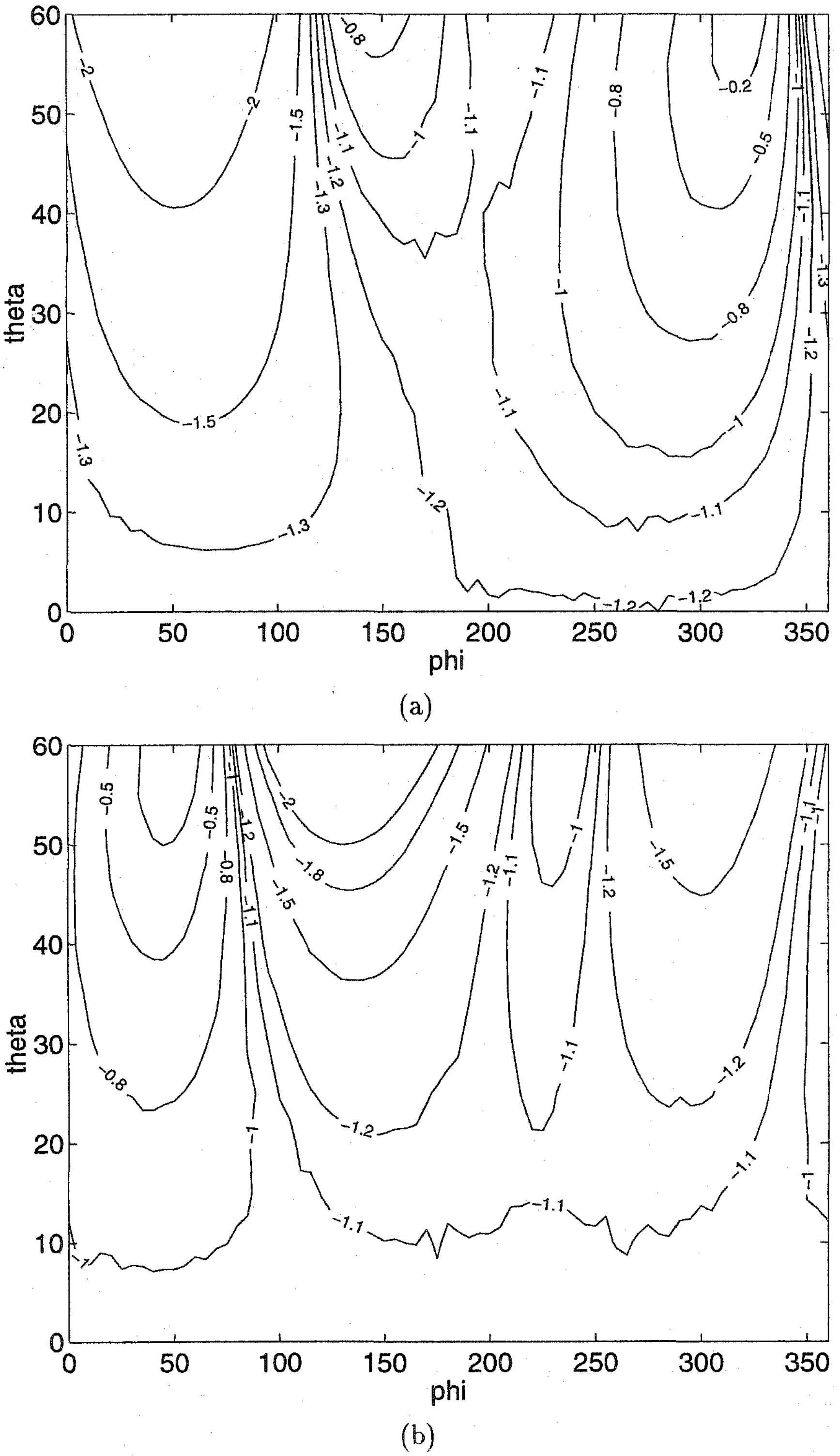

Figure 5.8: Polarization loss factor (PLF) of the slot loaded modified patch (antenna#1) for an incident RCP wave: (a) Lower resonant frequency, and (b) Higher resonant frequency.

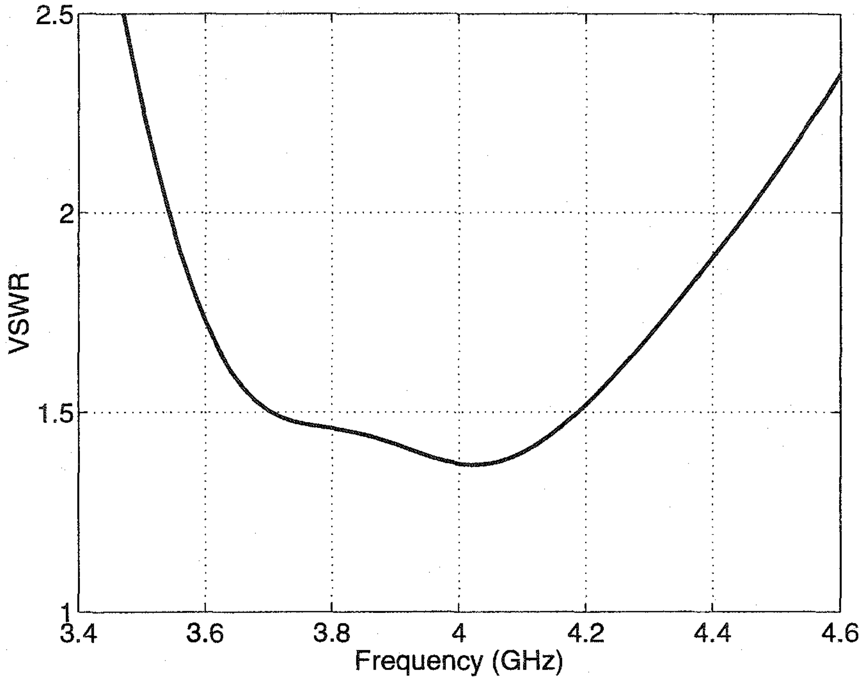

Figure 5.9: VSWR characteristics for the modified patch (antenna#2).

impedance bandwidth. The radiation patterns and PLF for the second modified patch (antenna #2) are shown in Fig. 5.11 and 5.12, respectively for both resonant frequencies (3.7GHz and 4.2GHz).

Performances of these antennas can also be enhanced using recently developed PBG structures. This has been discussed in detail in Chapter 7.

The different characteristics of both the above antennas have also been computed with a dielectric substrate of $\varepsilon_r = 2.1$. Similar performance characteristics have been observed except for the reduced operating frequency and narrower bandwidth. This is expected, as the Q factor of the antennas increases due to the presence of the dielectric substrate. Table 5.1 gives the dimensions of the various antennas that have been analyzed, while Table 5.2 summarizes their performance. It should be noted, that the antenna gain is computed with Ensemble. Bandwidths and the resonance

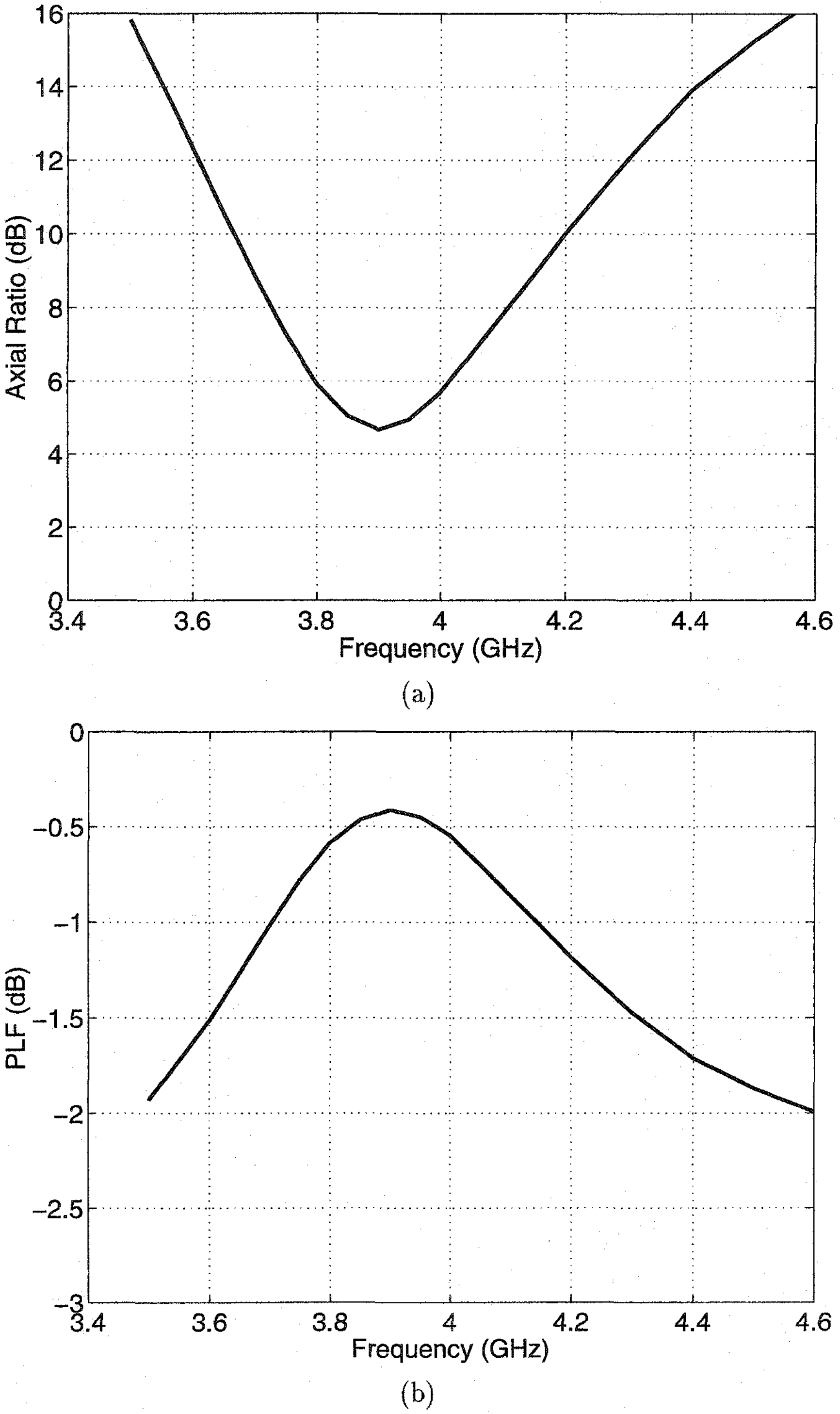

Figure 5.10: (a) Axial Ratio (AR), (b) Polarization Loss Factor (PLF) for the modified patch (antenna#2).

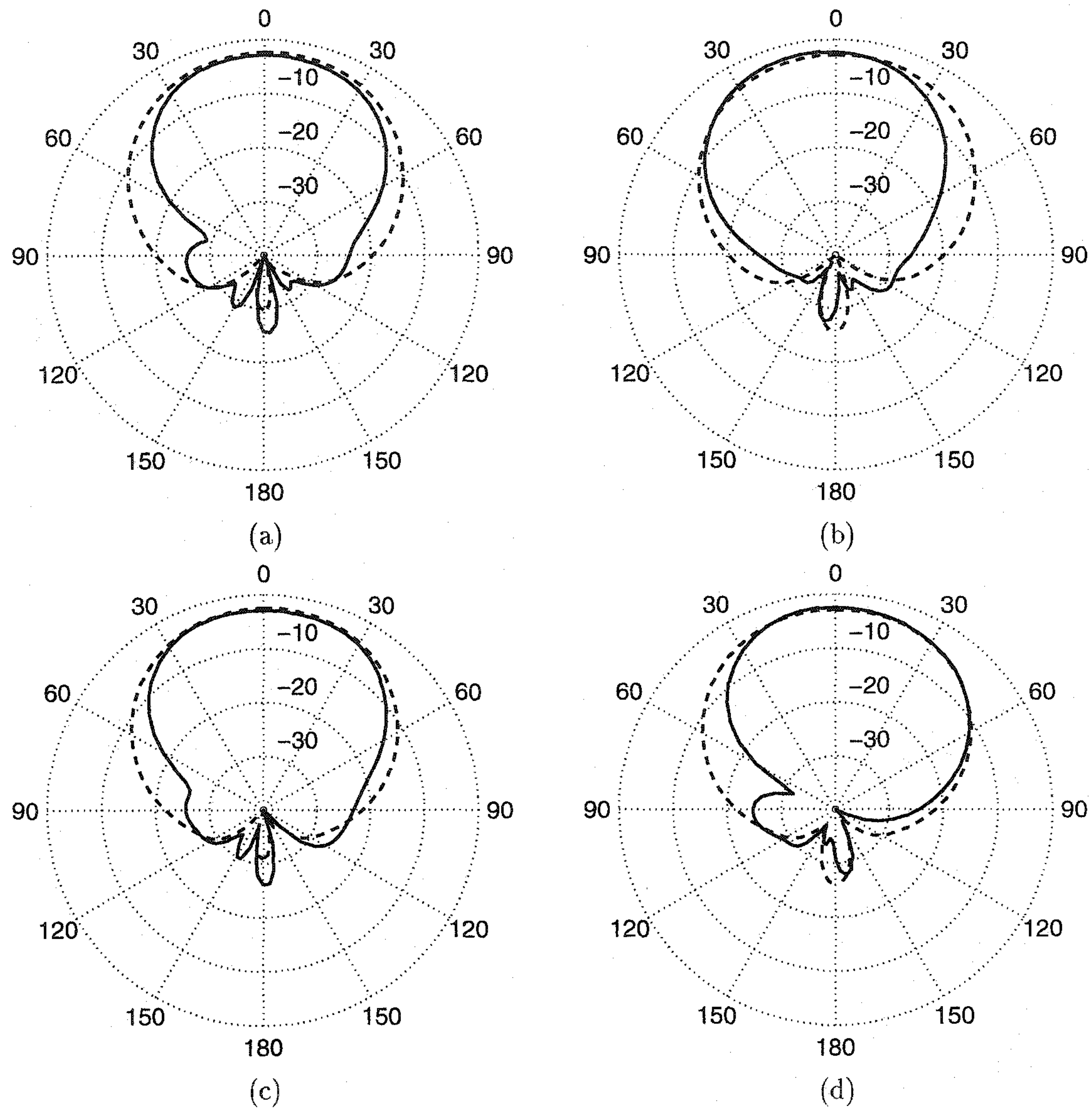

Figure 5.11: Radiation patterns E_θ (solid line) and E_ϕ (dotted line) of the modified patch (antenna#2): (a) & (b) at the lower resonant frequency in xz and yz plane, respectively, and (c) & (d) at the higher resonant frequency in xz and yz plane respectively.

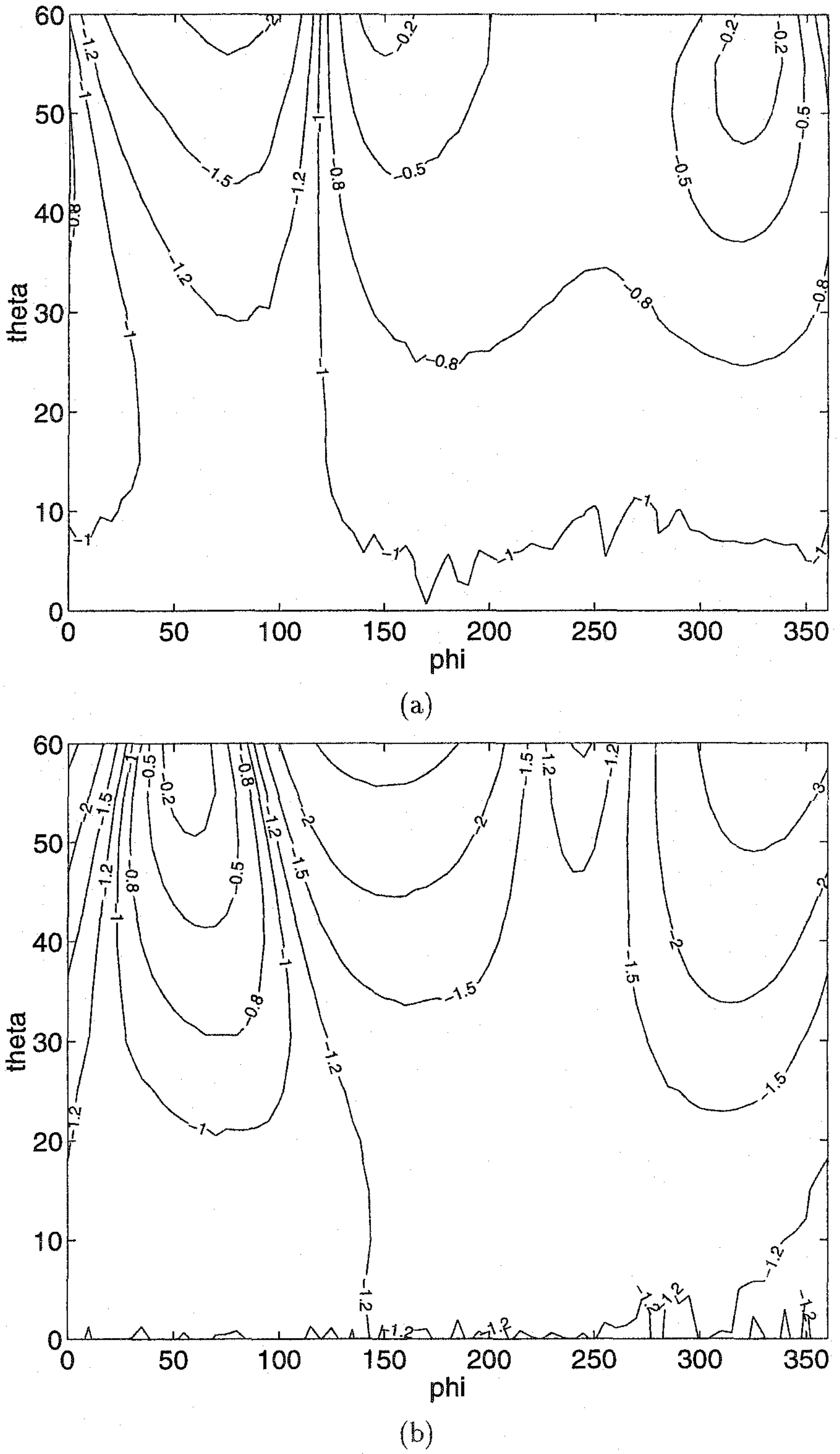

Figure 5.12: Polarization loss factor (PLF) of the modified patch (antenna#2) for an incident RCP wave: (a) Lower resonant frequency, and (b) Higher resonant frequency.

Table 5.1: Dimensions of the various antennas (See also Fig. 5.1).

Antenna	W mm	L mm	w mm	l mm	h mm	y_0 mm	Substrate permittivity, ε_r
Standard square	32	32	-	-	4	16	1.0
Modified square#1	32	32	18	26	4	18	1.0
Modified square#2	32	32	16	28	4	16	1.0
Standard square	32	32	-	-	4	16	2.1
Modified square#1	32	32	18	28	4	18	2.1
Modified square#2	32	32	16	29	4	16	2.1

frequencies are computed using both FDTD and Ensemble to validate the results. Excellent agreement (within 1%) is observed between the results obtained with the two methods.

5.3 Conclusion

Modified microstrip patch antennas have been designed and analyzed. They provide a reasonably wide impedance bandwidth, which is more than twice that of standard square patches with the same dimensions. The increase in the bandwidth is accompanied by gain reduction of about 1 dB. The modified patches also have an axial ratio of approximately 4.5 dB in the midband region and less than 14 dB within the bandwidth. They are suitable for the reception of circularly polarized incident waves with an average PLF of about 1.5 dB within the 10 dB beamwidth of the radiation pattern. These modified patches are well suited for application in satellite communication.

Table 5.2: Performance of the various antennas

Antenna	f_{r1}/f_{r2} GHz	Gain dB	Bandwidth (%)		
			VSWR$\leq$2	AR$\leq$6	PLF$\leq$ 1
Standard square, ε_r=1	3.89	9.0	7.59	-	-
Antenna#1 ε_r=1	3.7/ 4.1	7.96/ 7.95	21.44	5.2	10.8
Antenna#2 ε_r=1	3.7/ 4.2	7.6/ 7.9	22.78	5.6	11.5
Standard square, ε_r=2.1	2.89	6.73	4.4	-	-
Antenna#1 ε_r=2.1	2.8/ 3.0	5.97/ 5.9	11.07	2.7	5.6
Antenna#2 ε_r=2.1	2.8/ 3.1	5.68/ 5.8	12.78	3.1	6.4

Chapter 6

Planar Photonic Band Gap Structures

6.1 Introduction

Two dimensional (2D) planar PBG structures described in [65] and [66] have been shown to behave as high impedance electromagnetic surfaces and thus suppress the surface currents within the stop band. It has further been shown that, when these structures are used as ground planes, antenna performance is improved significantly due to the suppression of surface waves. The structure described in [65] has been modeled using a lumped inductance L and capacitance C that can only predict the first resonant frequency of the structure but not the band gaps.

In this chapter we explore an analytical model for 2D microwave PBG structures, such as those in [65] and [66]. First, the structures are represented as transmission lines periodically loaded with an impedance. The whole structure is then analyzed using the theory of periodic structures [93]. The dispersion diagram of the structures has been calculated using the proposed method. A new structure with multiple stop bands has also been described and modeled. The FDTD method is used for numerical calculation of the transmission and reflection coefficients of the structures [68]. Part of this work has already been published [92].

6.2 Modeling PBG Structures

6.2.1 Analytical Model

Figure 6.1 shows a schematic diagram of the high-impedance surfaces modeled and their essential dimensions. A square metal sheet connected to the continuous ground plane through a thin wire (as that in [65]) constitutes a unit of the lattice. Similarly, as shown in Fig. 6.1b, a unit of the lattice consists of a square metal patch with four narrow connecting branches and supported by a continuous ground plane (as in [66]). Circuits in Fig. 6.1a and 6.1b can be considered as arrays of reactively loaded resonators coupled by gap capacitance. Each unit cell of the structures is a halfwave length microstrip resonator of resonant frequency, $f \approx \frac{c}{2w\sqrt{\varepsilon_{reff}}}$, if the shorting post and connecting branches in Fig. 6.1a and Fig. 6.1b, respectively, are disregarded. An additional resonant frequency below the half wavelength resonance results from reactive loading a microstrip resonator [94]. Shorting pins, [95] or narrow connecting branches [96], as shown in Fig. 1a and 1b, have both been used. At the resonance frequencies the structure radiates energy into the space above and a little energy propagates along the structure. So, the high-impedance surfaces of the type shown in Fig 6.1 are structures periodically loaded with capacitances of the gaps and reactances provided by the shorting pins (Fig. 6.1a) or connecting branches (Fig. 6.1b).

Both the TE and TM modes with respect to the normal to the surface exist in these structures (also called LSE and LSM modes). These TE and TM modes are

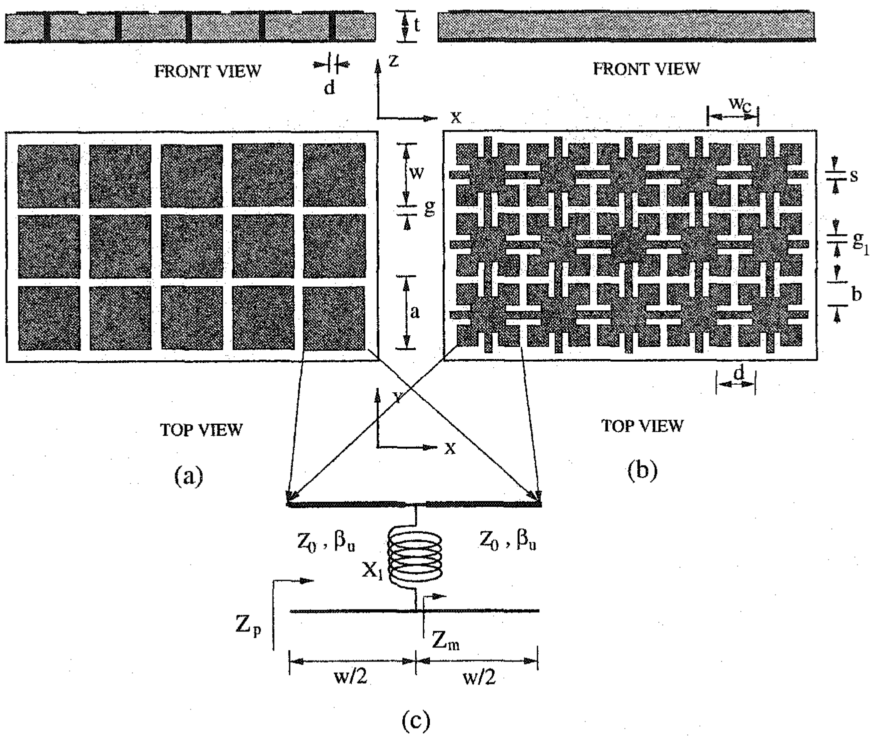

Figure 6.1: High impedance surfaces (a) array of square metal plates with shorting pins [65], (b) array of square metal plates with connecting branches [66], and (c) equivalent circuit of each resonator section.

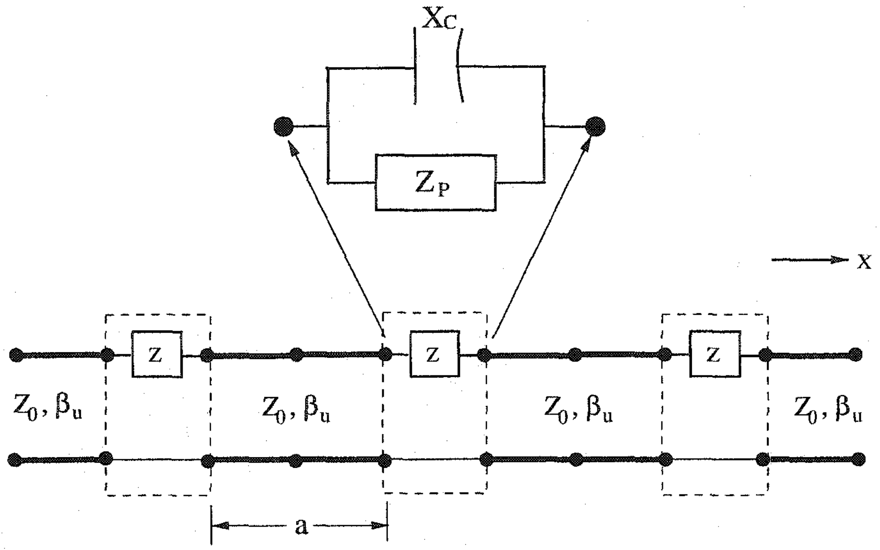

Figure 6.2: Equivalent circuit of the periodic structure.

coupled to each other, and neither mode can exist by itself [97] (contrary to the modes in a lossless dielectric slab on a ground plane).

Each reactively loaded resonator of Fig. 6.1a and 6.1b can be represented by an equivalent circuit as shown in Fig. 6.1c, where Z_p is the reactance of the resonator. The capacitive reactance X_c, results from coupling capacitance between the neighboring resonators. These are the two contributions to the total impedance between the two nodes of the periodic circuits shown in Fig. 6.2 for the wave propagation in x direction. The centrally located shorting pin in Fig. 6.1a provides the inductive loading X_l of the resonator, with inductance equal to [98]:

$$L = 2 \times 10^{-7} t \left[ln(\frac{4t}{d}) + 0.5(\frac{d}{t}) - 0.75 \right] \tag{6.1}$$

where t and d are the length and diameter of the pin, respectively.

The impedance of each microstrip resonator, for the wave propagating in the x

direction, can be calculated considering the loading at the center and using the well known transmission line formula:

$$Z_{in} = Z_0 \frac{Z_l + jZ_0 \tan(\beta_u l)}{Z_0 + jZ_l \tan(\beta_u l)} \tag{6.2}$$

where Z_0 is the characteristics impedance and β_u is the phase constant (losses of the transmission is assumed to be zero) of the microstrip resonator, Z_l is the loading impedance, and l is the line length. The transmission line is approximated either by microstrip line or conductor backed coplanar waveguide (CPW) depending on the width-height (w/t) ratio of the line and the dielectric material used (ε_r). For width-height ratio, $w/t \geq 2$, coupling with the neighboring resonators on two sides is negligible, and the line can be considered as microstrip line. But for low width-height ratio and low dielectric constant $(\varepsilon_r \leq 4)$, coupling with the resonators on two sides becomes significant and the line is better represented by conductor backed coplanar waveguides. The parameters $(Z_0$ and $\beta_u)$ of the line are calculated using microstrip line or CPW approximations depending on the dimensions of the structure. Design formulas used for calculating these parameters of the microstrip resonator are given in [99]. The impedance Z_p of each resonator section is calculated in two steps using Eqn. 6.3 and taking $Z_l = \infty$ at $l = 0$ and $Z_l = X_l // Z_m$ at $l = w/2$, where Z_m is the impedance before addition of the inductance and X_l is the inductive reactance at the center.

The coupling capacitor between the resonators has a capacitance [65]:

$$C = \frac{w\varepsilon_0(\varepsilon_{r1}+\varepsilon_{r2})}{\pi}\cosh^{-1}(\frac{a}{g}) \tag{6.3}$$

where ε_{r1} and ε_{r2} are the dielectric constants of the materials above and below the resonators and a, w, g are dimensions shown in Fig. 6.1.

Similarly each resonator of the uniplanar structure in Fig. 6.1b is loaded with four narrow axial connecting branches at the center. Total inductance provided by the branches can be calculated from [98]:

$$L = 0.25 \times 10^{-7} d \left[ln(\frac{d}{s}) + 0.2235(\frac{s}{d}) + 1.193 \right] k_g \tag{6.4}$$

where k_g is a correction factor to account for the ground plane and is [98]:

$$k_g = 0.57 - 0.145 ln(\frac{s}{t}) \tag{6.5}$$

where s and d are the width and length of the branch and t is the thickness of the substrate. Once X_l is known, Z_p can be calculated as described for the structure in Fig. 6.1a. The coupling capacitor between the resonators for the structure in Fig. 6.1b is:

$$C = \frac{2b\varepsilon_0(\varepsilon_{r1}+\varepsilon_{r2})}{\pi}\cosh^{-1}(\frac{a}{g}) \tag{6.6}$$

Equation 6.6 is obtained by modifying Equation 6.3 replacing w with $2b$ and a with w_c. Once the impedance of the resonator (Z_p) and the coupling capacitor (X_c)

are known for a particular direction of propagation, the structure in Fig. 6.1 can be treated as a transmission line periodically loaded with a lumped impedance Z consisting of Z_p in parallel with X_c with a period of 'a'. The equivalent circuit of the high-impedance surface for the wave propagation in x direction is shown in Fig. 6.2, and an analogous circuit corresponds to the propagation in y-direction. The propagation constant, γ, along the infinite periodic structure is calculated following the procedure outlined in [100]. For the circuit in Fig. 6.2 the voltage and current on either side of the n-th unit cell can be related using the $ABCD$ matrix:

$$\begin{bmatrix} V_n \\ I_n \end{bmatrix} = \begin{bmatrix} A & B \\ C & D \end{bmatrix} \begin{bmatrix} V_{n+1} \\ I_{n+1} \end{bmatrix} \tag{6.7}$$

where A, B, C and D are the matrix parameters for a cascade of transmission line section of length a, and a series impedance Z. So, the A, B, C, D parameters of the unit cell in Fig. 6.2 are given by

$$\begin{bmatrix} A & B \\ C & D \end{bmatrix} = \begin{bmatrix} cos(\beta_u a) & jZ_0 \sin(\beta_u a) \\ jY_0 sin(\beta_u a) & \cos(\beta_u a) \end{bmatrix} \begin{bmatrix} 1 & Z \\ 0 & 1 \end{bmatrix} \tag{6.8}$$

or

$$\begin{bmatrix} A & B \\ C & D \end{bmatrix} = \begin{bmatrix} cos(\beta_u a) & Z\cos(\beta_u a) + jZ_0 \sin(\beta_u a) \\ jY_0 sin(\beta_u a) & jZY_0 \sin(\beta_u a) + \cos(\beta_u a) \end{bmatrix} \tag{6.9}$$

where Z_0 is the characteristic impedance ($Y_0 = 1/Z_0$), and β_u is the phase constant for the unloaded structure. The characteristics impedance (Z_0) and the phase constant (β_u) used in Eqn. 6.7 and 6.8 are considered to be the same as those of the microstrip resonators.

For any wave propagating in the $+x$ direction, we must have

$$V(x) = V(0)e^{-\gamma x} \tag{6.10}$$

$$I(x) = I(0)e^{-\gamma x} \tag{6.11}$$

for a phase reference at $x = 0$. Since the structure is infinitely long, the voltage and current at the nth terminal can differ from the voltage and current at the $n + 1$ terminal only by the propagation factor, $e^{-\gamma a}$. Thus,

$$V_{n+1} = V_n e^{-\gamma a} \tag{6.12}$$

$$I_{n+1} = I_n e^{-\gamma a} \tag{6.13}$$

Using this result in Eqn. 6.7, we get the following:

$$\begin{bmatrix} V_n \\ I_n \end{bmatrix} = \begin{bmatrix} A & B \\ C & D \end{bmatrix} \begin{bmatrix} V_{n+1} \\ I_{n+1} \end{bmatrix} = \begin{bmatrix} V_{n+1}e^{\gamma a} \\ I_{n+1}e^{\gamma a} \end{bmatrix} \tag{6.14}$$

or

$$\begin{bmatrix} A - e^{\gamma a} & B \\ C & D - e^{\gamma a} \end{bmatrix} \begin{bmatrix} V_{n+1} \\ I_{n+1} \end{bmatrix} = 0 \qquad (6.15)$$

For a nontrivial solution, the determinant of the above matrix must vanish:

$$AD + e^{2\gamma a} - (A + D)e^{\gamma a} - BC = 0 \qquad (6.16)$$

or, since $AD - BC = 1$, using Eqn. 6.9 and 6.16

$$\cosh(\gamma a) = \frac{A + D}{2} = \cos(\beta_u a) + j\frac{Z}{2Z_0}\sin(\beta_u a) \qquad (6.17)$$

With $\gamma = \alpha + j\beta$, Eqn. 6.16 can be rearranged as

$$\cosh(\alpha a) cos(\beta a) + j\sinh(\alpha a)\sin(\beta a) = \cos(\beta_u a) + j\frac{Z}{2Z_0}\sin(\beta_u a) \qquad (6.18)$$

Since the right hand side of Eqn. 6.17 is real, as Z is imaginary for lossless resonators, as assumed, either $\alpha = 0$ or $\beta = 0$.

Case 1: $\alpha = 0$ corresponds to a non attenuated, propagating wave on the periodic structure, and defines the passband of the structure. Eqn. 6.17 reduces to

$$cos(\beta a) = \cos(\beta_u a) + j\frac{Z}{2Z_0}\sin(\beta_u a) \qquad (6.19)$$

which can be solved for β if the magnitude of the right hand side is less than or equal to unity.

Case 2: $\beta = 0, n\pi$ describes an attenuated wave along x direction, and this defines the stop band of the structure.

For periodic structures the propagation constant within the stop band is zero or $n\pi/a$. Within the pass band the propagation constant, β, is computed using Eqn.6.9 for different frequencies (β_u is a function of frequency).

6.2.2 Comparison with Numerical Modeling

Numerical modeling of the PBG structures shown in Fig. 6.1 has been carried out with the FDTD code, as described in more detail in chapter 3. The computational domain is terminated with perfectly matched layers (PML) of 7 cell thickness with a parabolic profile and the normal reflection below 80 dB. Cubic Yee-cell grid [68] with Δx = Δy = Δz = 0.5 mm is used. The structures are excited with a Gaussian pulse centered at 8 GHz and 6 GHz wide.

Fig. 6.3 and 6.4 show comparisons of the proposed analytic solution and numerical modeling for the structures in Fig. 1a and 1b, respectively. The dispersion diagrams (Fig. 6.3a and 6.4a) are valid for waves propagating in x or y direction (and for the so called $\Gamma - X$ region of the Brillouin zone [93]). For the dimensions of the structures considered (given in the caption), the shaded areas show the first stop-bands (between the 1st and 2nd modes). These analytically found stop bands are also shown in the numerically determined graphs of the transmission and reflection coefficients (Fig. 6.3b and 6.4b). For the structure in Fig. 6.1a, the transmission coefficient (S_{21}) is below -22 dB within the stop band. For the structure in Fig 6.1b, the attenuation level of the transmission coefficient (S_{21}) within the stop band is not that low (Fig. 6.4b). In this case the transmission coefficient is below -14 dB within

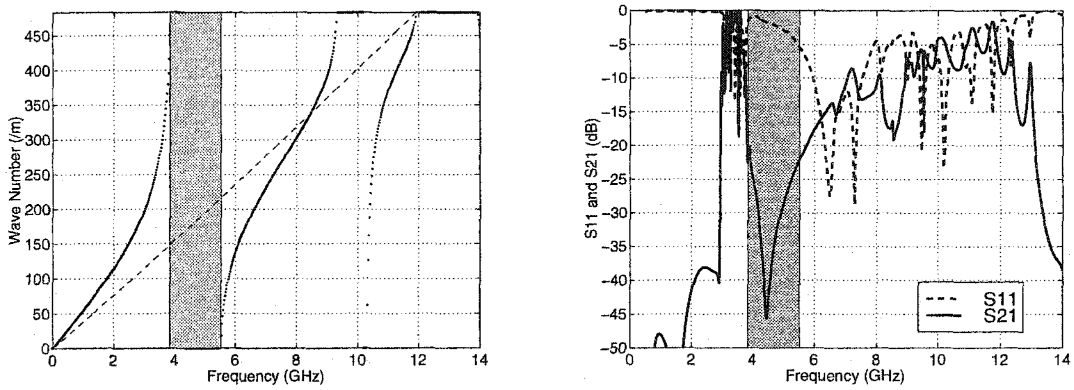

(a) (b)

Figure 6.3: (a) Dispersion diagram (dashed line represents the wave in a microstrip line), and (b) Transmission coefficients (S_{21}) and reflection coefficients (S_{11}) for the structure in Fig. 6.1a with the dimensions $a = 6.5mm, w = 6.0mm, g = 0.5mm, t = 3.0mm$, $d = 1.0mm$, and $\varepsilon_r = 4.2$.

the analytically determined stop band (5.7 to 8.1 GHz). The stop band attenuation level would further decrease if more PBG cells were inserted between the microstrip lines. On the other hand, this numerically obtained stop band level (in terms of dB values) is comparable to that reported in [66]. The dispersion diagrams in Fig. 6.3a and 6.4a also show band gaps between the subsequent higher modes like those reported in [65], [66].

Differences between the predicted band gaps and those evaluated numerically are more prominent in the lower frequency range. These can most likely be attributed to imperfect excitation and measurement of the transmission and reflection coefficients used here, as well as in the previous reports [65], [66]. The coupling of surface waves with the structures is very poor with this kind of setup, especially for lower frequencies. With a microstrip excitation (and also with coaxial line with extended inner conductor) there is no control over coupling to TE and TM modes. Finite size of the structure considered in the numerical simulations may also be responsible for

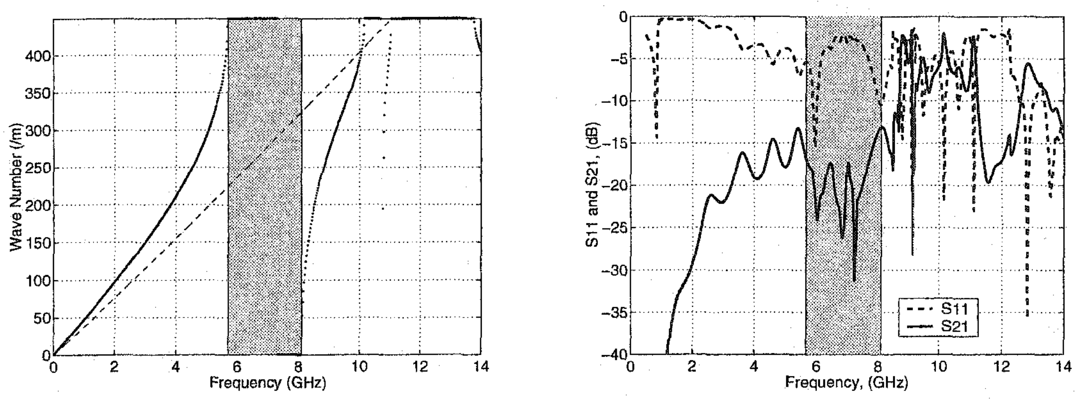

(a) (b)

Figure 6.4: (a) Dispersion diagram (dashed line represents the wave in a microstrip line), and (b) Transmission coefficients (S_{21}) and reflection coefficients (S_{11})for the structure in Fig 6.1b with the dimensions $a = 7.0mm, w = 6.5mm, g = s = 0.5mm, g1 = 0.75mm, b = 1.25mm, t = 3.0mm$, $d = 3.5mm$, and $\varepsilon_r = 4.2$.

the differences.

It has been mentioned earlier that the PBG structures also act as PMC surfaces within their stop bands. Figure 6.5 and 6.6 show the phase of the reflection coefficients (for normal incidence) from the PBG structures shown in Figure 6.1a and 6.1b, respectively (dimensions are shown in the caption). The shaded regions are the stop bands obtained from the analytical computations. Band gaps for the high frequency structures reported in [65] and [66] have also been computed using the proposed analytical model and compared with the previously published data. Table 6.1 summarizes the results and compares the analytical results with the numerical computations. The table also gives the ratio, R, of the stop-band determined from the reflection phase to that computed analytically.

The following observations can be made from Figures 6.3 - 6.6 and Table 6.1. As expected, the analytic model does not fully predict the behavior of the periodic structure, as it does not apply to all directions of surface wave propagation. However,

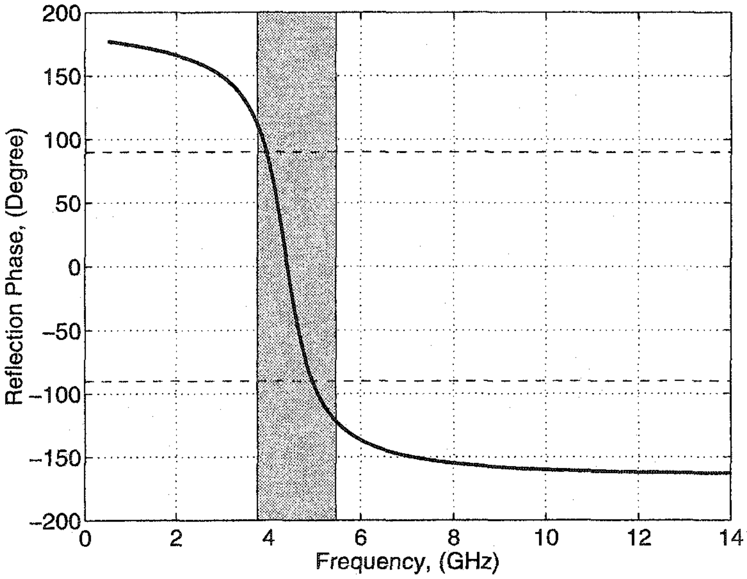

Figure 6.5: Phase of the reflection coefficient for the structure in Fig. 6.1a with the dimensions $a = 6.5mm, w = 6.0mm, g = 0.5mm, t = 3.0mm$, $d = 1.0mm$ $\varepsilon_r = 4.2$. (shaded region is the analytically obtained band gap)

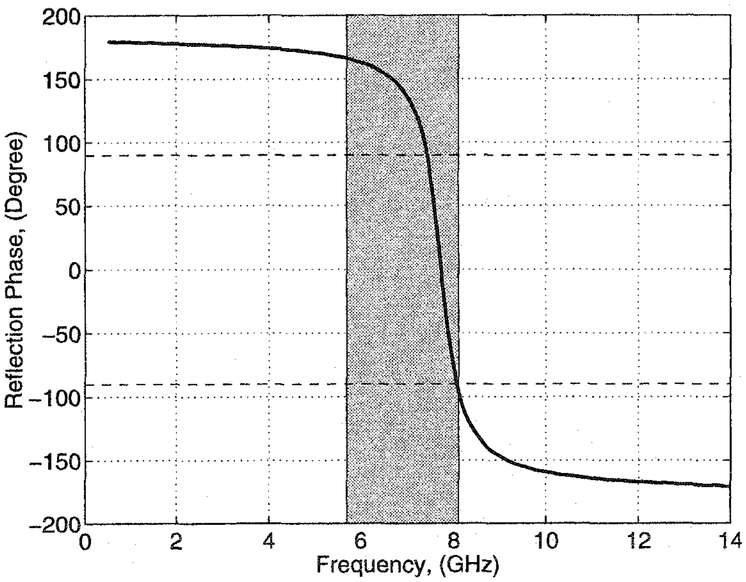

Figure 6.6: Phase of the reflection coefficient for the structure in Fig. 6.1a with the dimensions $a = 7.0mm, w = 6.5mm, g = s = 0.5mm, g1 = 0.75mm, b = 1.25mm, t = 3.0mm$, $d = 3.5mm$, and $\varepsilon_r = 4.2$. (shaded region is the analytically obtained band gap)

Table 6.1: Comparison of analytic model predictions with numerical computations.

Structure	Analytic stop-band	Reflection Phase $\pm\pi/2$ band	Previously published data	R
Patches with pins, Fig.6.1a $w/t = 2$, $\varepsilon_r = 4.2$	3.76-5.44 GHz (Fig.6.3)	3.95-4.95 (Fig.6.5)	-	$\frac{0.225}{0.365} = 0.62$
Patches with pins, Fig.6.1a $w/t = 1.4$, $\varepsilon_r = 2.2$	9.88-16.7 GHz	10.1-14.77 GHz	10-14.5 GHz$^{(1)}$	$\frac{0.376}{0.513} = 0.73$
Patches with branches, Fig.6.1b $w/t = 2.17$, $\varepsilon_r = 4.2$	5.7-8.1 GHz (Fig.6.4)	7.4-8.1 GHz (Fig.6.6)	-	$\frac{0.091}{0.348} = 0.26$
Patches with branches, Fig.6.1b $w/t = 2.2$, $\varepsilon_r = 10.2$	8.9-12.7 GHz	11.85-12.7 GHz	11.4-12.8 GHz$^{(2)}$ 9-12.8 GHz$^{(3)}$	$\frac{0.069}{0.352} = 0.20$

1. From [65], computed (FEM) stop-band for all direction of propagation (approx. values from Fig.10).
2. From [66], computed (FDTD) stop-band for all directions of propagation.
3. From [66], computed (FDTD) stop-band for x (or y) direction of propagation (approx. values from Fig.5).

it provides a quick and useful means of predicting the stop-band for propagation along the principal axis. Computations with the FDTD of the phase of the reflection coefficient, on one hand, illustrate the limitation of the analytic model, as the practical stop band is narrower. On the other hand, FDTD simulations are also simple and fast. Their simplicity is due to much simpler periodic boundary conditions than those required to compute the dispersion diagram. They also illustrate that the stop-band based on the reflection phase is reduced for a PBG structure of type shown in Figure 6.1b compared to a PBG structure in Figure 6.1a.

6.3 Compact and Multiple Stop Band Structures

In many applications of PBG structures reduction of their physical size is important. In typical PBG structures the period of the lattice has to be a half-wavelength at the stop band frequency. However, a stop band frequency below the half-wavelength frequency can be obtained by loading the unit cells [65], [66]. Of the two PBG structures described earlier, the one with the shorting pins (Fig. 6.1a) is more compact as the loading on the patches is greater than that of the other structure with connecting branches (Fig. 6.1b). It is obvious from the discussions in the previous section that by increasing the loading on the individual patches the stop band frequency can be reduced further. On the other hand, if the patches have multiple resonances below the half-wavelength frequency, the structure can have multiple stop bands. In [65], a second layer of metal pads with grounding vias is inserted below the top layer, as shown in Fig. 6.7, to make the structure more compact. However, this makes the structure more difficult to manufacture.

In this section, a novel compact structure is presented that produces multiple stop

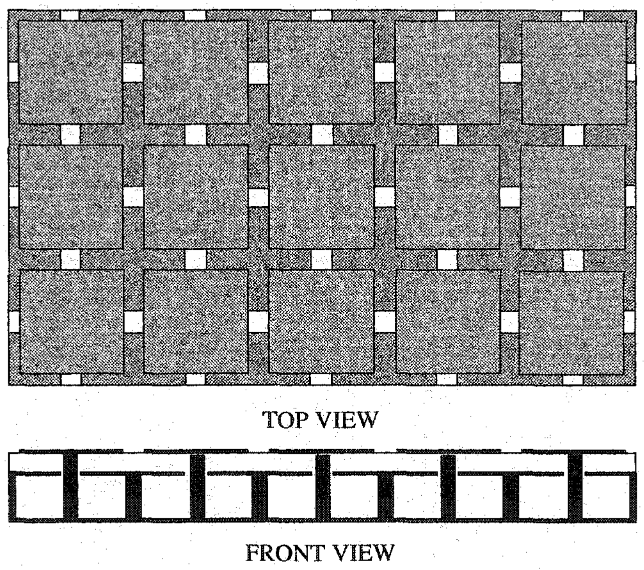

Figure 6.7: Two layered PBG structure.

bands below the half-wavelength stop band frequency.

6.3.1 Design and Analytical Model

The structure is obtained by modifying the single layered structure of Fig. 6.1a and is shown in Fig. 6.8a. Each square patch is modified by connecting four narrow branches while retaining the same period of the structure. The branches contribute additional loading on the patches along with the shorting pins. Fig. 6.8b shows the dimensions of each patch. For the wave propagation in x direction, each resonator section can be presented by the equivalent circuit shown in Fig. 6.8c, where X_l and Z_b are the reactances of the shorting pin and each narrow branch, respectively. In this case, only the two branches connected to the x-axis edges contribute to the loading. The width and length of the patch are w and w_l, respectively; X_l is the same as that in Fig. 6.1a and given by Eqn. 6.1, and Z_b is given by

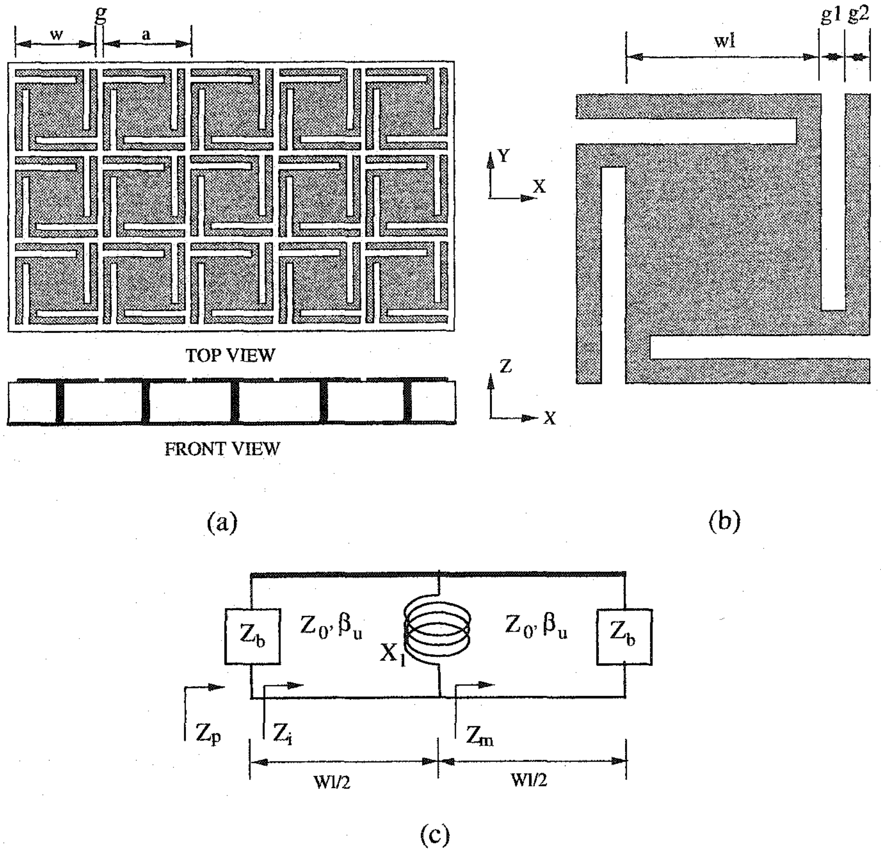

(a)

(b)

(c)

Figure 6.8: (a) Single layered compact and multiple stop band PBG structure, (b) single cell of the structure, and (c) equivalent circuit of each resonator section.

$$Z_b = -jZ_{0l}cot(\beta_{ul}d_l) \tag{6.20}$$

where Z_{0l}, β_{ul}, and d_l are the characteristics impedance, phase constant, and length of the connecting branch, respectively. Once X_l and Z_b are known, the impedance of each resonator section (Z_p) is calculated using Eqn. 6.2 in three steps taking $Z_l = Z_b$ at $l = 0$, $Z_l = X_l//Z_m$ at $l = w_l/2$ and $Z_l = Z_b//Z_i$ at $l = w_l$, where Z_m and Z_i are the impedances before addition of X_l and Z_b, respectively.

The structure in Fig. 6.7a can then be represented by the periodic circuit shown in Fig. 6.2, where X_c is the capacitive reactance of the coupling capacitor C and given by Eqn. 6.3. Now the structure can be analyzed as discussed in the previous section, and the dispersion diagram can be calculated using Eqn. 6.18.

6.3.2 Comparison with Numerical Modeling

The transmission and reflection coefficients of the structure are computed using FDTD method, as described in the previous section, and compared with the analytical solution in Fig. 6.9. The dispersion diagram (Fig. 6.9a, valid for x or y direction and for $\Gamma - X$ region) shows wide band gaps at (3.48-4.50) GHz and (8.28-9.14) GHz, and a narrow gap at 6.1 GHz. These analytically found wide band gaps (shaded regions) are also apparent in the numerically determined graphs of reflection and transmission coefficients in Fig. 6.9b. As anticipated, the lower edge of the first band gap (3.48 GHz) is lower than that of the structure in Fig. 6.1a (3.76 GHz) with the same period. This compact nature of the structure and multiple stop bands are obtained at the cost of reduced band widths.

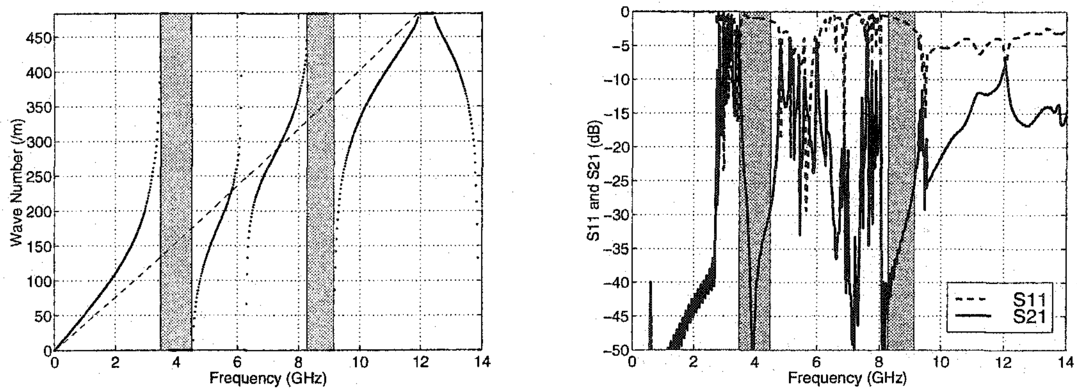

(a) (b)

Figure 6.9: (a) Dispersion diagram (dashed line represents the wave in a microstrip line), and (b) Transmission coefficients (S_{21}) and reflection coefficients (S_{11}) for the structure in Fig. 6.1a with the dimensions $a = 6.5mm, w = 6.0mm, g = g1 = g2 = 0.5mm, wl = 4.0mm, t = 3.0mm$, and $d = 1.0mm$.

6.4 Conclusions

Two different high-impedance surfaces proposed in the literature have been represented by an analytic model, which combines the transmission line representation and the theory of periodic structures. The proposed analytic approach is simple, fast and suitable also for other PBG structures for which the impedance for the unit cell can be obtained. The dispersion diagrams calculated with the proposed method predict a stop band region that is in good agreement with those obtained from the numerical experiment. However, the analytic model does not consider all directions of surface wave propagation, and it is useful only as the first step in design of the structure. Computation with the FDTD of the phase of the reflection coefficient provides an additional simple means of evaluation of the practical stop-band frequency range. Results of these computations are in agreement (max. differences below 4%) with more complex numerical evaluations reported in [65] and [66].

A new compact structure with multiple stop band has also been modeled and analyzed using the proposed method. Analytically obtained stop bands for the structure are in good agreement with the numerically computed results.

Chapter 7

Application of PBG Structure in Patch Antenna

It has been mentioned earlier that the propagation of surface waves on and within the substrate of microstrip patch antenna lowers its efficiency. Two techniques have been thus far used to suppress surface wave propagation in the antenna substrate to achieve better performance, namely micromachining [101],[102] and photonic band gap (PBG) structures [51]-[54]. It has also been observed that the application of PBG structures increases the bandwidth of patch antennas.

In this chapter, one of the patch antennas described in Chapter 5 has further been investigated integrating with planar PBG structure. A significant improvement has been observed in both impedance and AR bandwidth. Antennas and the PBG structure are modeled with the finite-difference time-domain (FDTD) method. Experimental results for the antennas are also presented.

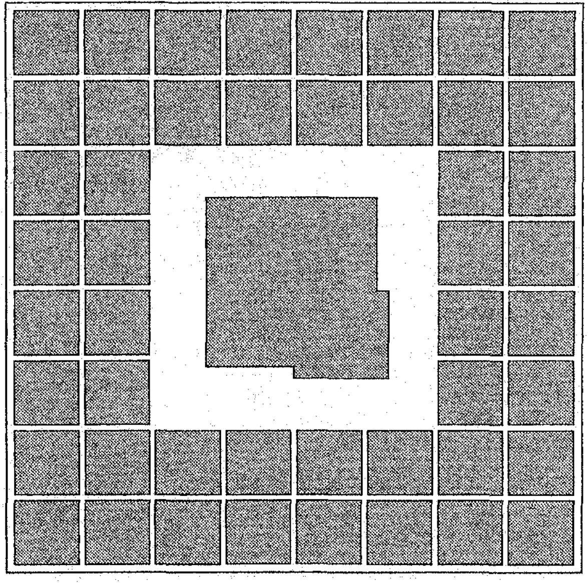

Figure 7.1: Modified square patch antenna surrounded by PBG cells

7.1 Description of the Antenna and PBG Structure

Antenna#2 (Figure 5.1b) described in Chapter 5 serves as the basic reference structure. This patch has been surrounded by two rows of a PBG structure, as shown in Figure 7.1. The PBG structure described in Chapter 6 (Figure 6.1a) has been used because of its wider band gap and compact nature. Dimensions of the PBG structure are selected such that the band gap can accommodate the operating range of the antenna. Both the analytical and numerical methods described in Chapter 6 have been used to design the PBG structure.

The patch has been designed on a $26.25mm \times 26.25mm \times 1.5mm$ board for operation in X band. The permittivity of the substrate is $\varepsilon_r = 4.4$. Other dimensions of the antenna are $L = 7.5mm$, $l = 6.75mm$, $x_0 = 1.125mm$, and $y_0 = 4.25mm$. A capacitive feed technique [36] has been used for the antenna to compensate the input inductance due to the coaxial feed. A narrow slot has been cut around the feed point on the patch to introduce the capacitance. The PBG structure has been designed with a band gap from 7.6GHz to 9.8GHz. The period of the structure is 3.25mm with a gap of 0.25mm between the square patches. The diameter of the shorting pin is 0.5mm.

7.2 Numerical Results

The VSWR, AR, and PLF characteristic of the antenna with (PBG patch, solid line) and without the PBG structure (ref. patch, dotted line) are shown in Figures 7.2a, 7.2b, and 7.2c, respectively. A significant improvement in all the characteristics of the antenna is evident from the figures. Performances of the two antennas are summarized in Table 7.1. Figures 7.3a and 7.3b show the radiation patterns of the reference and PBG patch, respectively. The solid lines represent the E_θ component and the dotted lines represent the E_ϕ component of the pattern in xz plane. The patterns are computed for frequencies close to the resonance. It can be observed that, with the PBG substrate, the amplitude ratio is improved in the upper hemisphere. This also improves the PLF distribution for an incident CP wave in all direction above the ground plane. An improvement in front to back ratio of the radiation patterns is also evident. This is due to the reduction of scattering at the edges of the finite ground plane. This is expected as the propagation of surface wave is suppressed within the substrate.

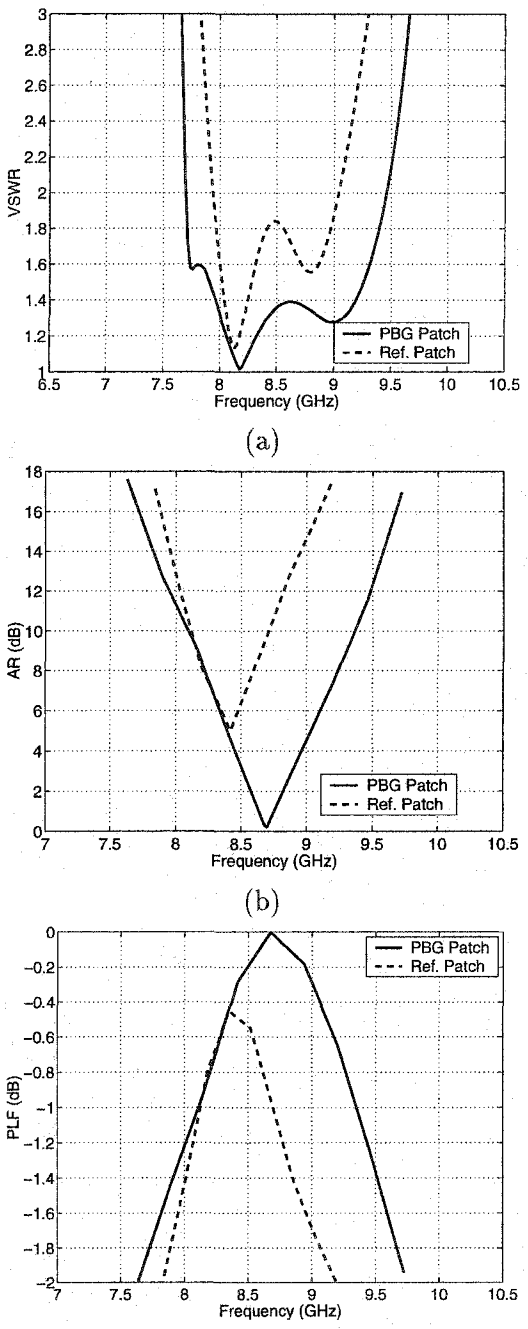

(a)

(b)

(c)

Figure 7.2: Numerically computed (a) VSWR, (b) Axial ratio (AR), and (c) polarization loss factor (PLF) of the reference and the PBG patch.

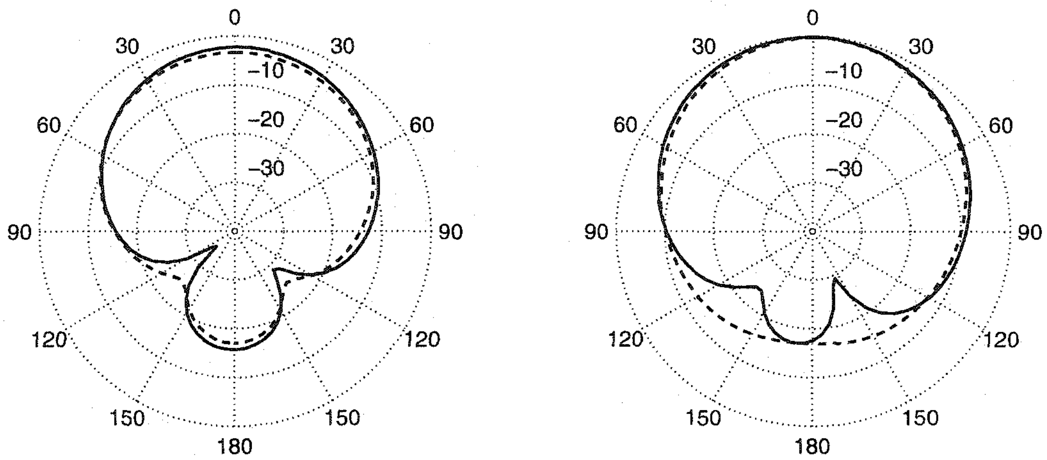

(a) (b)

Figure 7.3: Numerically computed E_θ (solid line) and E_ϕ (dotted line) component of the radiation pattern in the xz plane for (a) reference patch, and (b) PBG patch.

7.3 Experimental Results

Both, the reference and PBG patch have been fabricated on 1.5 mm thick FR4 (plexiglass) board of 26.25mm×26.25mm. The dielectric constant of the board is 4.4. Experimental methods for measuring the antenna properties have been described in Appendix B. Figures 7.4a and 7.4b show the VSWR and AR of the antennas. The solid and dotted lines represent the PBG patch and reference patch, respectively. Table 7.1 also summarizes the experimental results and compares with the numerical results. It is observed that the experimental results are shifted in frequency by 2%. This discrepancy may arise from the fabrication process of the antenna. Another probable reason may be the poor modeling of the planar feed capacitor of the patches. The gap around the feed point has been modeled with only one FDTD cell. Nevertheless, the agreement between the bandwidths is excellent. Figures 7.5a and 7.5b show the spin-linear patterns of the reference and PBG patch on the *E-plane* (patterns on the *H-plane* are similar) at 8.6GHz and 9.0GHz, respectively. The pat-

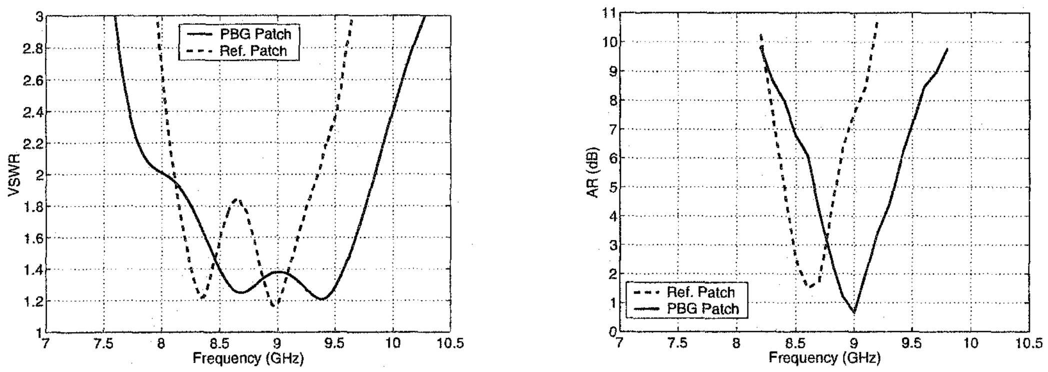

(a) (b)

Figure 7.4: Measured characteristics of the reference and PBG patch antenna, (a) VSWR, and (b) Axial Ratio.

terns have been measured only above the ground plane due to the limitations of the experimental setup. Significant improvement in the axial ratio for the PBG patch can be observed in all directions with a maximum AR of 2.5 dB along 90^0. The gain of the PBG patch (5.67dBi at 9.0 GHz) is also increased compared to the reference patch (4.55dBi at 8.6 GHz). This has also been observed by the previous authors [65], [66].

Table 7.1: Performance of the various antennas.

Antenna		Bandwidth			Front to Back ratio (dB)
		VSWR$\leq$ 2 (GHz)	AR$\leq$ 6 (GHz)	PLF$\leq$ 1 (GHz)	
Modified square patch	Computed	13.1% (7.93-9.04)	1.4% (8.35-8.47)	6.9% (8.12-8.7)	14
	Measured	14.0 % (8.12-9.33)	5.0% (8.37-8.8)	–	–
Modified square patch on PBG structure	Computed	20.2% (7.7-9.46)	8.8% (8.33-9.1)	14.25% (8.11-9.35)	18
	Measured	20.2% (8.02-9.84)	8.9% (8.6-9.4)	–	–

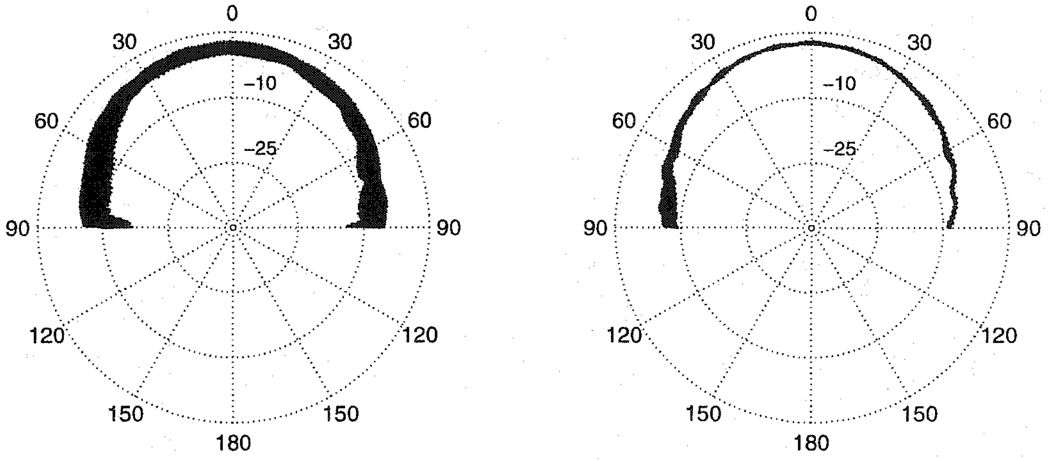

(a) (b)

Figure 7.5: Measured spin-linear patterns of (a) reference patch (8.6GHz), and (b) PBG patch (9.0GHz).

7.4 Conclusions

A wide band circularly polarized patch antenna has been designed and integrated with 2D planar PBG structure. Antenna parameters of both the reference and PBG patch antennas have been measured and compared with numerical computations. An excellent agreement has been found. It has also been observed, that only two cells of PBG structure surrounding the circularly polarized patch antenna can significantly improve the antenna performance.

Chapter 8

Conclusions and Future Work

8.1 Conclusions

The main objective of this work has been to investigate and improve the design of compact and low profile antennas for wireless communications. Another objective of this work has been to model the antennas in realistic and complex environment in order to achieve reliable performance characteristics. To realize these objectives the following investigations have been accomplished.

Two antennas for hand held telephones are designed that can operate in both the allocated frequency bands in North America (AMPS and PCS). These dual band antennas, namely: the sleeve-monopole antenna and the dual-meander-sleeve antenna, provide wide bandwidths for both bands with a single feed. Antenna performances (radiation patterns, VSWR) for both the antennas have been investigated in presence of a realistic head model of the user. The FDTD code has been used to model the antennas and the user's head. The energy absorbed (SAR) in the user's head from the designed antennas has also been calculated and shown to be within the prescribed safe limits.

Two novel microstrip patch antennas have been developed for possible application in satellite communications or on portable computers. These new antennas have been designed by modifying the radiating edges of a standard square patch antenna. The impedance bandwidths of the antennas are more than twice of that of the standard square patch antennas. The wider bandwidth is achieved without increasing the volume of the antennas. A wide circular polarization bandwidth is also achieved with a single feed to the antennas.

In this work, various existing high-impedance surfaces have also been analyzed. These surfaces are basically 2D planar PBG structures and have promising features to be used as ground planes for low profile antennas (e.g. microstrip antennas). A simple analytical model for these 2D planar PBG structures has been presented for the calculation of dispersion diagram. The analytically calculated dispersion diagrams clearly show the stop bands of the structures. The stop band of the structures has also been calculated numerically by computing the transmission and reflection coefficients using the FDTD method. A good agreement is observed between the analytical and numerical results.

One of the patch antennas analyzed has further been investigated by integrating it with the PBG structure. Different parameters of the antennas have been measured and compared with the numerically computed results. An excellent agreement has been found between the computed and measured results. A significant improvement in the antenna performances has also been observed due to the integration with the PBG structure.

8.2 Future Work

8.2.1 Antennas

In the future dual band antennas for hand held telephones can be modified to make them more compact. One possible solution is to use one sleeve instead of two. Different characteristics of these single sleeved antennas should be investigated with and without the presence of the user's head. Another area of research can be to continue the current research on wide band circularly polarized patch antennas. The possibility of the use of these antennas in handsets and other mobile systems for satellite communication should be investigated. This research should be more focused to make the antennas more compact for the use in handsets.

8.2.2 PBG Structures

Further research on the PBG surfaces can be continued. It has been mentioned in Chapter 4 that the metal box of the handheld telephone becomes a part of the antenna system and radiates a significant portion of the absorbed energy within the user's head. This is due to the current that flows on the surface of the handset. A layer of the high-impedance surfaces can be used on the handsets to prevent the propagation of surface current and reduce the radiation into the user's head. On the other hand, as this structure also serves as a magnetic surface, horizontal monopole antennas can be used for handsets instead of vertical monopoles [65]. The main obstacle for achieving these goals is the physical size of the PBG structures. Currently available structures are not small enough to accommodate a sufficient number of PBG cells on the handset surfaces. Thus, research should be directed towards finding techniques to make more compact PBG surfaces (e.g. lower operating frequency with small periodicity). In addition, better methods for numerical computations of the PBG structures using FDTD method may be explored.

Bibliography

[1] K. Fujimoto, A. Henderson, K. Hirasawa, and J. R. James, *Small Antennas* , Research Studies Press, UK, distributed by Wiley , USA, 1987.

[2] Z. D. Liu, and P. S. Hall, "Dual-band antenna for hand-held portable telephones," *Electron Letters.* , Vol.32, pp.609-610, March 1996.

[3] P. Erätuali, P. Haapala, and P. Vainikainen, "Dual frequency wire antennas," *Electron Letters.* , Vol.32, pp.1051-1052. June 1996.

[4] I. J. Bhal, and P. Bhartia, *Microstrip Antennas* , Dedhuam, Massachusetts: Artech-House, 1980.

[5] C. A. Balanis, *Antenna Theory Analysis and Design*, Harper and Row Publishers, NY, 1982.

[6] *IEEE Transaction on Antennas and Propagation* , Vol. AP-17, No.3, May 1969.

[7] C. A. Balanis, *Advanced Engineering Electromagnetics*, John Wiley & Sons Inc., USA, 1989.

[8] K. Fujimoto and J. R. James, *Mobile Antenna Systems Handbook.* Norwood, MA: Artech House, 1994.

[9] J. T. Williams, H. J. Delgado, and S. A. Long, "An antenna pattern measurement technique for eliminating the fields scattered from the edges of a finite ground plane", *IEEE Transactions. On Antennas and Propagation* , Vol.AP-38, No.11, pp.1815-1822, November 1990.

[10] S. A. Long, and A. W. C. Chu, "Radiation patterns of a monopole antenna mounted on a cubical conducting box", *IEEE Antennas and Propagation International Symposium Digest* , pp.654-657, June 1987.

[11] M. M. Weiner, "Monopole element at the center of a circular ground plane whose radius is small or comparable to a wavelength", *IEEE Transactions. On Antennas and Propagation* , Vol.AP-35, No.5, pp.488-495, May 1987.

[12] S. Bhattacharya, S. A. Long, and D. R. Wilton, "The input impedance of a monopole antenna mounted on a cubical conducting box", *IEEE Transactions. On Antennas and Propagation* , Vol.AP-35, No.7, pp.756-762, July 1987.

[13] H. Nakano, J. Yamaguchi, and H. Mimaki, "Backfire radiation from a monofilar helix with a small ground plane", *IEEE Transactions. On Antennas and Propagation* , Vol.AP-36, No.10, pp.1359-1364, October 1988.

[14] M. N. O. Sadiku, *Numerical Techniques in Electromagnetics* , Boca Raton: CRC Press, pp.309-406, 1992.

[15] K. Sato, K. Matsumoto, K. Fujimoto, and K. Hirasawa, "Characteristics of a planar inverted-F antenna on a rectangular conducting body", *Electronics and Communications in Japan* , Part 1, Vol.72, Scripta Publishing, October 1989.

[16] J. E. Padgett, C. G. Gunther, and T. Hattori, "Overview of wireless personal communications," *IEEE Communications Magazine* , Vol.33, pp.28-41, January 1995.

[17] Y. Ebine, and K. Kagoshima, "Multi-frequency dipole antenna with closed-spaced parasitic elements," *IEICE Transactions.* , Vol.J71-B, pp.1252-1258, 1988.

[18] C. R. Rowell, and R. D. Murch, "A compact PIFA suitable for dual-frequency 900/1800 MHz operation," *IEEE Transactions on Antennas and Propagation.* , Vol.AP-46, pp. 596-598, April 1998.

[19] Z. D. Liu, P. S. Hall, and D. Wake, "Dual-Frequency planar inverted-F antenna," *IEEE Transactions. Antennas and Propagation* ,Vol.AP-45, pp.1451-1458, October 1997.

[20] K. Karimullah, K-M. Chen, and D. P. Nyqueist, "Electromagnetic coupling between a thin wire antenna and a neighboring biological body: theory and experiment", *IEEE Transactions on Microwave Theory and Techniques* , Vol. MTT-28, pp.1218-1225, November 1980.

[21] H. O. Ruoss, and F. M. Landstorfer, "Slot antenna for hand held mobile telephones showing significant reduced interaction with the human body", *Electronic Letters*, Vol.32, No.6, pp.513-514, March 1996.

[22] J. Toftgrad, S. Hornsleth, and J. Bach Andersen, "Effects on portable antennas of the presence of a person", *IEEE Transactions on Antennas and Propagation.*, Vol.AP-41, pp.739-746, 1993.

[23] M. A. Jensen, and Y. Rahmat-Samii, "EM interaction of handset antennas and human in personal communications", *Proceedings of the IEEE*, Vo.83, No.1, pp.7-17, 1995.

[24] J. S. Colburn, and Y. Rahmat-Samii, "Human proximity effects on circularly polarized handset antennas in personal satellite communications," *IEEE Transactions on Antennas and Propagation.*, Vol.46, pp.813-820, July 1998.

[25] M. Okoniewski, and M. A. Stuchly, "A study of the handset antenna and human body interaction," *IEEE Transactions. Microwave Theory Tech*, Vol.44, pp.1855-1864, October 1996.

[26] So-ichi Watanabe, M. Taki, T. Nojima, O. Fujiwara, "Characteristics of the SAR distributions in a head exposed to electromagnetic fields radiated by a hand-held portable radio Watanabe", *IEEE Transactions on Microwave Theory and Techniques* , Vol. MTT-44, No.10, pt.2, pp.1874-1883, October 1996.

[27] A. D. Tinniswood, C. M. Furse, and O. P. Gandhi, "Computations of SAR distributions for two anatomical based models of the human head using CAD files of commercial telephones and the parallelised FDTD code." *IEEE Transactions. Antennas Propagation.*, Vol.46, pp.828-833, July 1998.

[28] D. H. Schaubert, "A review of some microstrip antenna characteristics", in *Microstrip Antennas* edited by D. M. Pozar and D. H. Schaubert, New York: IEEE Press, pp.59-67, 1995.

[29] E. Chang, S. A. Long, and W. F. Richards, "An experimental investigation of electrically thick rectangular microstrip antennas," *IEEE Transactions. Antennas Propagation,* Vol.AP-3, pp.767-772, June 1986.

[30] D. H. Schaubert, D. M. Pozar, and A. Adrian, "Effect of microstrip antenna substrate thickness and permittivity: comparison of theories and experiment," *IEEE Transactions. Antennas Propagation,* Vol.AP-37, pp.677-682, June 1989.

[31] A. Henderson, J. R. James, and C. M. Hall, "Bandwidth extension techniques in printed conformal antennas," Military Microwaves, MM86, Brighton, U.K., June 1986.

[32] H. Pues, and A. Van de Capelle, "An impedance matching technique for increasing the bandwidth of microstrip antennas," *IEEE Transactions. Antennas Propagation.,* Vol.AP-37, pp.1345-1354, November. 1989.

[33] D. A. Paschen, "Practical examples of integral broadband matching of microstrip antenna elements," *Proceedings of the 1986 Antenna Applications Symp.,* pp.199-217, 1986.

[34] H. An, B. Nauwelaers, and A. Van de Capelle, "Broadband active microstrip array elements", *Proceedings of the 1986 Antennas and Applications Symposium* , pp. 199-217, 1986.

[35] F. S. Fong, H. F. Pues, and M. J. Withers, "Wideband multilayer coaxial fed microstrip antenna element", *Electronic Letters* , Vol.21, pp.479-499, 1985.

[36] P. S. Hall, "Probe compensation in thick microstrip patches", *Electronic Letters* , Vol.21, pp,606-607, 1987.

[37] S. Dey, C. K. Anandan, P. Mohanan, and K. G. Nair, “A new broadband circular patch antenna”, *Microwave and Optical Technology Letters* , Vol.7, No.13, pp.604-605, September 1994.

[38] P. S. Hall, C. Wood, and C. Garrett, “Wide bandwidth microstrip antenna for circuit integration,” *Electronics Letters,* Vol.15, pp.458-460, 1979.

[39] C. H. Chen, A. Tulintseff, and R. M. Sorbello, “Broadband two-layer microstrip antenna,” *IEEE Antennas Propagation. Soc. Int. Symp. Dig.,*, pp.251-254, 1984.

[40] G. Kumar, and K. C. Gupta, “Directly coupled multiple resonator wideband microstrip antennas,” *IEEE Transactions. Antennas Propagation.,* Vol.AP-33, pp.588-593, June 1985.

[41] H. Pues, J. Bogaers, R. Pieck, and A. Van de Capelle, “Wideband quasi-log-periodic microstrip antenna,” *Inst. Elec. Eng. Proc.,* Vol.128, pt.H, pp.159-163, June 1981.

[42] T. Huynh, and K. F. Lee, “Single-layer single-patch wideband microstrip antenna”, *Electronics Letters* , Vol.31, No.16, pp.1310-1312, August 1995.

[43] D. M. Pozar, “A review of bandwidth enhancement techniques for microstrip antennas”, in *Microstrip Antennas* edited by D. M. Pozar and D. H. Schaubert, New York: IEEE Press, pp.157-166, 1995.

[44] J. D. Joannopoulos, R. D. Meade, & J. N. Winn, *Photonic Crystals: Modeling the Flow of Light*, Princeton University Press, Princeton, 1995.

[45] E. Yablonovitch, T. J. Gmitter,and K. M.Leung, “Photonic band structure: The face-centered-cubic case employing nonspherical atoms”, *Phys. Rev. Letters* , Vol.67, pp.2295, 1991.

[46] M. M. Sigalas, et al., “Metallic photonic band-gap materials”, *Phys. Rev. B* Vol.52, pp.11744, 1995.

[47] E. Yablonobitch, “Photonic band-gap structures”, *J. Opt. Soc. Am. B* Vol.10, pp.283, 1993.

[48] V. Radisic, Y. X. Qian, R. Coccioli, T. Itoh, “Novel 2-D photonic bandgap structure for microstrip lines”, *IEEE Microwave and Guided Wave Letters* , Vol.8, pp.69-71, Feb. 1998.

[49] K. Agi, et al., “Photonic crystals: A new quasi-optical component for high-power microwaves”, *IEEE Trans. Plasma* , (Special Issue on High Power): pp.1067, 1996.

[50] K. P. Ma, K. Hiroshi, F. R. Yang, Y. Qian and T. Itoh, “Realization of magnetic conducting surface using novel photonic band gap structure”, *Elec. Lett.*, Vol.34, pp.2041-2042, October 1998.

[51] Y. X. Qian, R. Coccioli , D. Sievenpiper , V. Radisic, E. Yablonovitch , T. Itoh, “A microstrip patch antenna using novel photonic band-gap structures”, *Microwave Journal* , Vol.42, pp.66, January 1999.

[52] M. P. Kesler, J. G. Meloney, and L. Shirley, “Antenna design with the use of photonic band-gap materials as all-dielectric planar reflectors”, *Microwave & Opt. Tech. Letters* , Vol.11, pp.169, 1996.

[53] G. S. Smith, M. P. Kesler, and J. G. Meloney, "Dipole antennas used with all-dielectric, woodpile photonic-bandgap reflectors: gain, field patterns, and input impedance", *Microwave and Optical Technology Letters* , Vol.21, No.3, pp.191-196, May 1999.

[54] K. Agi, K. J. Malloy, E. Schamiloglu, M. Mojahedi, E. Niver, "Integration of a microstrip patch antenna with a two-dimensional photonic crystal substrate", *Electromagnetics* , Vol.19, pp.277-290, May-June 1999.

[55] P. K. Kelly, S. Hagness, and M. Piket-May, "Band diagram for a grounded periodic dielectric substrate with square lattice and finite height", *URSI GA abstracts* , Toronto, pp.97, August 13-21, 1999.

[56] M. Plihal, and A. A. Maraduddin, "Photonic band gap structure of two-dimensional system: the triangular lattice", *Physical Review B* , Vol.44, October 1991.

[57] D. F. Sievenpiper, et. al., "3D metallo-dielectric photonic crystals with strong capacitive coupling between metallic islands", *Phys Review Letters* , Vol.80, pp.2829-2832, March 1998.

[58] E. A. Navarro, J. Martinez-Pastor, V. Such, "Transmission properties at microwave frequencies of two-dimensional metallic lattices", *Journal of Applied Physics* , Vol.86, pp.1177-1180, August 1999.

[59] K. M. Leung, and Y. F. Liu, "Full vector wave calculation of photonic band structures in face-centered-cube dielectric media", *Physical Review Letters* , Vol.65, pp.2646-2649, 1990.

[60] H. Y. D. Yang, "Double vector-integral-equation method for microstrip-line on photonic band-gap substrates", *IEEE MTT-S International Microwave Symposium Digest* , pp.191-194, June 1997.

[61] R. Coccioli, T. Itoh, and G. Pelosi, "A finite element generalized network analysis of finite thickness photonic crystal", *IEEE MTT-S International Microwave Symposium Digest* , pp.195-198, June 1997.

[62] J. B. Pendry, "Photonic band structures", *Journal of Modern Optics* , Vol.41, No.2, pp.174-175, 1994.

[63] H. Y. D. Yang, "Finite deference analysis of 2D photonic crystals", *IEEE Transactions on Microwave Theory and Techniques* , Vol.MTT-44, pp.2688-2695, 1996.

[64] S. Fan, P. R. Villeneuve, and J. D. Joannopolos, "Large omnidirectional band gaps in metallodielectric photonic crystals", *Physical Review B*, Vol.52, pp.10673-10676, 1995.

[65] D. F. Sievenpiper et. al., "High-impedance electromagnetic surfaces with a forbidden frequency band", *IEEE Microwave Theory and Techniques* , Vol.MTT-47, pp.2059-2074, November 1999.

[66] R. Coccioli, F. R. Yang, K. P. Ma, and T. Itoh, "Aperture-coupled patch antenna on UC-PBG substrate", em IEEE Microwave Theory and Techniques , Vol.47, pp.2123-2130, November 1999.

[67] P. K. Kelly, L. Diaz, M. Piket-May, and I. Rumsey , "Investigation of scan blindness mitigation using photonic bandgap structure in phased arrays", *Proc. of SPIE*, Vol.34, pp.239-248, July 1998.

[68] K. S. Yee, "Numerical solution of initial boundary value problems involving Maxwell's equations in isotropic media", *IEEE Trans. Antennas Propagation* , Vol.AP-14, pp.302-307, May 1966.

[69] A. Taflove, *Computational Electrodynamics: The Finite-Difference Time-Domain Method* , Norwood, MA: Artech House Publications, 1995.

[70] K. S. Kunz, and R. J. Lubbers, *The Finite Difference Time Domain Method for Electromagnetics* , Boca Raton, FL: CRC Press Inc., 1993.

[71] J. P. Berenger, "A perfectly matched layer for the absorption of electromagnatic waves," *J. Comp. Phys.*, Vol.114, pp.185-200, 1994.

[72] S. Chebolu, and R. Mitra, "The analysis of microwave antennas using the FDTD method", *Microwave Journal* , pp.134-150, January 1996.

[73] M. Okoniewski, M.A. Stuchly, and S. S. Stuchly, "Modeling of interactions of cellular telephones with the user and implantable devices," *ANTEM, Symposium on Antenna Technology and Applied Electromagnetics, Proc.* , Montreal, Canada, pp.409-412, 1996.

[74] M. Ali, S.S. Stuchly, and K. Caputa, "A wide-band dual meander-sleeve antenna", *Journal of Electromagnetic Waves Applications* , Vol.10, pp.1223-1236, 1996.

[75] M. G. Douglas, M. Okoniewski, and M. A. Stuchly, "A planar diversity antenna for hand-held PCS devices," *ANTEM, Symposium on Antenna Technology and Applied Electromagnetics, Proceedings* , Montreal, Canada, pp.447-450, 1996.

[76] J. Anderson, M. Okoniewski, and S. S. Stuchly, "Practical 3D contour/staircase treatment of metals in FDTD", *IEEE Microwave and Guided Wave Letters* , Vol.6, pp.146-148, 1996.

[77] N. Kuster, and Q. Balzano, "Experimental and numerical dosimetry", in *Mobile Communications Safety* , edited by N. Kuster, Q. Balzano and J. C. Lin, London: Chapman & Hall, pp. 13-64, 1997.

[78] C. Polk, and E. Postow, '*Handbook of Biological Effects of Electromagnetic Fields* , Boca Raton: CRC Press, 1986.

[79] Federal Communications Commission (FCC), *Guidelines for Evaluating the Environmental Effects of Radiofrequency Radiations,* ET Docket No. 93-62, Washington, DC, August 1996.

[80] CENELEC, *Consideration for human exposure to EMFs from Mobile Telecommunication Equipment (MTE) in the frequency range 30MHz-6GHz*, European Prestandard prepared by the Committee for Electrotechnical Standardization, 1997.

[81] K. Caputa, M. Okoniewski, and M. A Stuchly, "Algorithm for computing specific absorption rate", *IEEE Antennas Propagation Magazine* (accepted, Fall 1999).

[82] M. A. Schamberger S. Kosanovich, and R. Mittra, "Parameter extraction and correction for transmission lines and discontinuities using the finite-difference time-domain method", *IEEE Microwave Theory and Techniques* , Vol.MTT-44, No.6, pp.919-925, June 1996.

[83] R. C. Hall, and D. I. Wu, *Ensemble User's Guide (Version 5.1),* Ensoft Corp., 1998.

[84] K. R. Foster, and H. P. Schwan, "Dielectric properties of tissues", in *Handbook of Biological Effects of Electromagnetic Fields* , edited by C. Polk and E. Postow, Boca Raton, FL: CRC Press, pp.27-96, 1986.

[85] I. G. Zubal, C. R. Harrell, E. O. Smith, Z. Rattner, G. R. Gindi, and P. H. Hoffer, "Computerized three-dimensional segmented human anatomy", *Physics in Medicine and Biology* , Vol.21, pp.299-302, 1994.

[86] M. Rahman, M. A. Stuchly, M. Okoniewski, "Dual-band strip-sleeve monopole for handheld telephones", *Microwave and Optical Technology Letters* , Vol.21, No.2, pp.79-82, 1999.

[87] T. Williams, M. Rahman, M. A. Stuchly, "Dual-Band Meander Antenna for Wireless Telephones", *Microwave and Optical Technology Letters* , Vol.24, No.2, pp.81-85, January 2000.

[88] R. King, "Asymmetrically driven dipole antennas and the sleeve dipole," *Proceedings of I. R. E.*, pp. 1154-1163, October 1950.

[89] H. E. King, and J. L. Wong, "An experimental study of balun-fed open-sleeve dipole in front of a metallic reflector," *IEEE Transactions Antennas Propagation*, pp. 201-204, March 1972.

[90] H. E. King, and J. L. Wong, "Height-reduced meander zigzag monopoles with broad band characteristics", *IEEE Transactions Antennas Propagation* , Vol.AP-34, No.5, pp.716-717, May 1986.

[91] M. Rahman, M. A. Stuchly, "Dual-polarization broadband patch antenna", *Microwave and Optical Technology Letters* , Vol.22, No.6, pp.414-420, September 1999.

[92] M. Rahman, M. A. Stuchly, "Transmission Line-Periodic Circuit Representation of Planar Microwave Photonic Band Gap Structures", To appear in *Microwave and Optical Technology Letters* , July 2001.

[93] L. Brillouin, *Wave propagation in Periodic Structures* , Dover Publications, Inc., 1953.

[94] S. Maci, and G. B. Gentilli, "Dual frequency patch antenna", *IEEE Antennas and Propagation Magazine* , vol. 39, pp. 13-19, Dec. 1997.

[95] M. Sanad, "Effects of the shorting posts on short circuit microstrip patches", *Proceedings of the IEEE Antennas and Propagation International Symposium,* Part 2 (of 3), pp. 794-797, Seattle, WA, USA, June 19-24, 1994.

[96] S. E. Davidson, S. A. Long, and W. A. Long, "Dual-Band Microstrip Antenna with Monolithic Reactive Loading", *Electronics Letters* , vol. 21, pp. 936-937, 1985.

[97] R. Collin, *Field theory of Guided Waves*, IEEE Press, New York, 1991.

[98] I. J. Bahl, and P. Bhartia, *Microwave Solid State Circuit Design* , John Wiley, New York, 1988.

[99] K. C. Gupta *et. al.*, *Microstrip Lines and Slotlines* , Artech House Inc., 1996.

[100] D. M. Pozar, *Microwave Engineering* , John Wiley & Sons, Inc; 1998.

[101] G. P. Gauthier, A Courtay, and G. M. Rebeiz, "Microstrip antennas on synthesized low dielectric-constant substrate," *IEEE Transactions Antennas Propagation,* Vol.AP-45, pp. 1310-1314, August 1997.

[102] I. Papapolymerou, R. F. Drayton, and L. P. B. Katehi, "Micromachined patch antennas," *IEEE Transactions Antennas Propagation,* Vol.AP-46, pp. 275-283, Feb. 1998.

Appendix A

Antenna Parameters

Since this research is concerned with designing and modeling antennas, some basic antenna parameters, such as radiation patterns, half power beam-widths, input impedance, voltage standing wave ratio (VSWR), bandwidth, gain, directivity, efficiency, and polarization are described here. These parameters are important for the characterization of the antennas in complex environments. All definitions and mathematical expressions are taken from [5] unless otherwise indicated. The definitions inside quotation marks are from the IEEE Standard Definitions of Terms for Antennas (IEEE Std 145-1973) [6].

A.1 Radiation Patterns and Half-Power Beam-Width

The *radiation pattern* of an antenna is defined as the "graphical representation of the radiation properties of the antenna as a function of angular coordinates. In most cases the radiation pattern is determined in the far-field region and is represented as a function of the angular coordinates. Radiation properties include radiation intensity, field strength, phase or polarization."

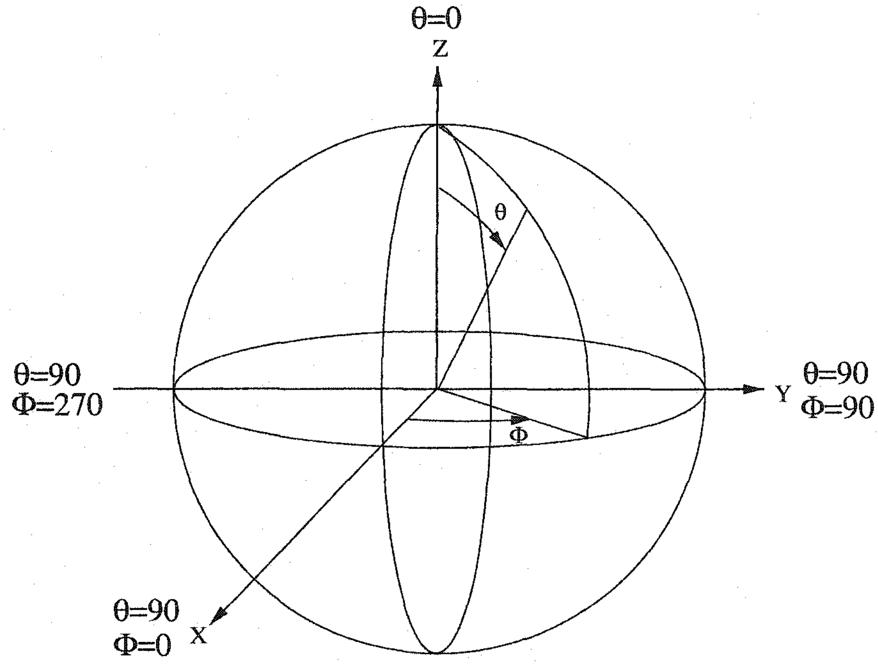

Figure A.1: Spherical coordinate system.

Radiation pattern of an antenna can be either a *power pattern* or a *field pattern* . Referring to Fig. A.1 a two dimensional pattern is obtained by fixing one of the angle (θ or ϕ) while varying the other. Keeping ϕ constant, and varying θ ($0 \leq \theta \leq 180$) gives *elevation patterns* . Similarly, keeping θ constant, and varying ϕ ($0 \leq \theta \leq 2\pi$) gives *azimuthal patterns* .

The performance of an antenna is often described by using patterns in two principal planes which are called the *E-plane* and the *H-plane* patterns. The *E-plane* pattern for a linearly polarized antenna is defined as "the plane containing the electric field vector and the direction of maximum radiation". Similarly, the *H-plane* pattern is defined as "the plane containing the magnetic field vector and the direction of maximum radiation". Radiation pattern can be broadly classified as isotropic, directional, and omnidirectional. An isotropic radiator is defined as, "a hypothetical antenna having equal radiation in all directions". A directional antenna is one "having the property of radiating or receiving electromagnetic waves more effectively in some directions than in others". An *omnidirectional pattern* is defined as one "having an essentially nondirectional pattern in a given plane of the antenna and a directional pattern in any orthogonal plane".

"In a plane containing the direction of the maximum beam, the angle between the directions in which the radiation intensity is one-half the maximum value of the beam" is defined as the *half-power beamwidth* of an antenna.

A.2 Input Impedance and VSWR

Antenna input impedance is defined as "the impedance presented by an antenna at its terminals or the ratio of the appropriate components of the electric and magnetic fields at a point". The input impedance consists of a resistance and a reactance of which the resistance comprises of a radiation resistance, R_r and a loss resistance, R_L.

The VSWR of antenna is defined by the ratio of the reflected and incident voltages at the input terminal of an antenna and can be expressed in terms of the antenna input impedance by

$$VSWR = \frac{|Z_{in} + Z_0| + |Z_{in} - Z_0|}{|Z_{in} + Z_0| - |Z_{in} - Z_0|} \tag{A.1}$$

where Z_0 is the characteristics impedance of the feeding transmission line and Z_{in} is the input impedance of the antenna.

A.3 Directivity, Efficiency and Gain

The directivity of an antenna is defined as "the maximum value of the *directive gain* in the direction of its maximum value". Thus

$$D_0 = \frac{4\pi U_{max}}{P_{rad}} \tag{A.2}$$

where D_0 is the directivity, U_{max} is the maximum of the radiation intensity and P_{rad} is total radiated power by the antenna.

Antenna efficiency accounts for the losses at the input terminals of the antenna and within the structure of the antenna. Losses in an antenna may occur due to the mismatch between the feeding line and the antenna, and also due to conductor and dielectric losses.

The overall efficiency can be expressed as $e_t = e_r e_{cd}$ where e_t is the overall efficiency, e_r is the reflection efficiency, and e_{cd} is the conduction and dielectric efficiency. The reflection efficiency is $(1 - |\Gamma|^2)$ where Γ is the reflection coefficient and $e_{cd} = \frac{R_r}{R_r + R_L}$ where R_r and R_L are radiation and loss resistance, respectively.

A useful measure of the performance of an antenna is its gain. *Power Gain* of an antenna in a specific direction is defined as "4π times the ratio of the radiation intensity in that direction to the power accepted by the antenna from a connected transmitter". The maximum gain is defined as

$$G_0 = e_t D_0 \tag{A.3}$$

A.4 Bandwidth

The bandwidth of an antenna can be defined as “the range of frequencies within which the performance of the antenna, with respect to some characteristics, conforms to a specified standard”.

The characteristics of the antenna can be pattern, input impedance, beamwidth, gain, efficiency, polarization, or beam direction. The term ‘range of frequencies’ may mean the ratio between the upper and the lower frequencies for a broadband antenna. For narrow-band antennas, the bandwidth is usually expressed as a percentage of the center frequency. The type of bandwidth chosen for a particular antenna is usually the one corresponding to the antenna characteristic that is most strongly influenced by frequency. For the antennas considered in this research, the input impedance is a strong function of frequency while the radiation pattern, polarization, and gain are less affected. Thus in this research the term bandwidth refers to the input impedance bandwidth.

A.5 Polarization

The *polarization of a radiated wave* is defined as “property of a radiated electromagnetic wave describing the time-varying direction and relative magnitude of the electric field vector; specifically, the figure traced as a function of time by the extremity of a vector at a fixed location in space, and the sense in which it is traced, as observed along the direction of propagation”.

Polarization may be classified as *linear, circular,* and *elliptical* . Considering the instantaneous electric field of a plane wave, travelling in the positive z-direction, [7]

$$\mathcal{E} = \hat{a}_x E_{x0}^{+} cos(\omega t - \beta z + \phi_x) + \hat{a}_y E_{y0}^{+} cos(\omega t - \beta z + \phi_y) \qquad \text{(A.4)}$$

(The magnetic field is related to the electric field of (A.4) by the intrinsic impedance of the medium), polarization is defined as follows .

Linear Polarization: A time-harmonic field is linearly polarized at a given point in space if the electric (or magnetic) field vector at that point is always oriented along the same straight line at every instant of time. This can happen if the field vector possesses (a) only one component or (b) two orthogonal linearly polarized components that are in time phase or 180^o out of phase.

Circular Polarization: Circular polarization can be obtained only when the magnitude of the two components in Eqn. (A.4) are the same and the phase difference between them is odd multiple of $\pi/2$.

Elliptical Polarization: Elliptical polarization can be achieved (a) when the magnitude of the field components in (A.4) are not equal and the time-phase difference between them is an odd multiple of $\pi/2$ or (b) when the time-phase difference between the components of (2.4) is not equal to $\pi/2$ irrespective of their magnitudes.

Appendix B

Antenna Measurements

Antennas described in Chapter 7 have been fabricated and their properties have been measured. This chapter presents the experimental methods for measuring the antenna properties. Possible source of errors and the methods to minimize them are also discussed.

B.1 Input Impedance, Return Loss and VSWR

The measurements of the impedance of an antenna can be performed with a wide range of laboratory equipment, from conventional bridges to sophisticated automatic systems. In this work, a broadband swept frequency vector network analyzer (HP8720C) has been used. Figure B.1 shows the schematic diagram of the experimental setup. The antenna is connected to the VNA through a coaxial connector and a section of transmission line. The outer conductor of the coaxial connector is connected to the ground plane and the inner conductor is connected to the antenna. The VNA measures the reflection coefficient, Γ, from the antenna at the reference plane, as shown in Figure B.2, and given by

$$\Gamma = |\Gamma|e^{j\phi} = \frac{E_r}{E_i} \tag{B.1}$$

where $|\Gamma|$ and ϕ are the magnitude and phase of the reflection coefficient.

Once the reflection coefficient is known, the return loss (S_{11}), input impedance (Z_{in}) and the VSWR can be calculated using the following equations

$$S_{11} = 20log_{10}|\Gamma| \tag{B.2}$$

$$Z_{in} = Z_c \left[\frac{1+\Gamma}{1-\Gamma}\right] \tag{B.3}$$

$$VSWR = \frac{1+|\Gamma|}{1-|\Gamma|} \tag{B.4}$$

where Z_c is the characteristic impedance of the transmission line and the coaxial connector.

To get accurate results, the VNA is calibrated by connecting standard 'short', 'open', and a 50Ω load at the calibration plane. The electrical delay caused by the thin coaxial connector from the calibration plane to the antenna input terminal (reference plane) must be taken into account. This is particularly important for obtaining the exact phase of the reflection coefficient from the antenna itself. The characteristic impedance of both the transmission line and the thin coaxial connector should be the same. Any mismatch produces an unwanted reflection from the calibration plane

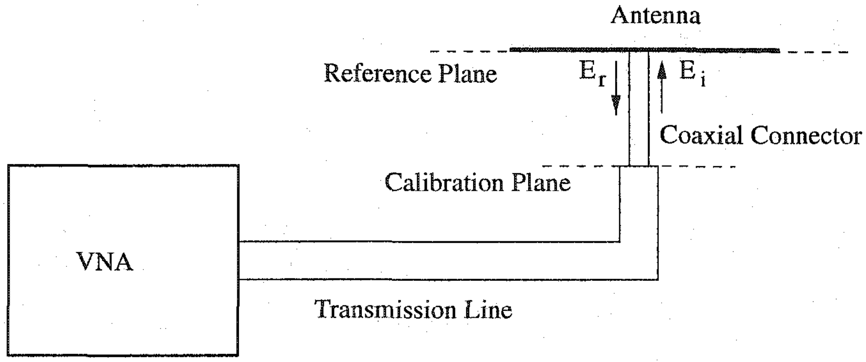

Figure B.1: Experimental setup for measuring the antenna input impedance, VSWR, and return loss.

that corrupts the actual reflection from the reference plane. By using a longer coaxial connector and applying a gate in the time domain, this unwanted reflection can be filtered out.

B.2 Radiation Patterns, Axial Ratio, and Gain

The measurement of the properties such as radiation patterns, axial ratio, and gain require that the radiator under test is illuminated by a uniform plane wave. This is achieved only in the far-field region. The requirement of an ideal plane wave illumination can be achieved by utilizing a compact range. A Compact Antenna Test Range (CATR) is a collimating device which generates nearly planar wavefronts in a very short distance compared to the $2D^2/\lambda$ (minimum) distance required to produce the same size test region using the standard system configuration. It can be mentioned here that the CATR system is usually used for testing antennas with large dimensions. The antennas that have been tested for this research are small in size (D=27mm) and a standard measurement system could have been used to measure their properties. However, the facilities at the University of Manitoba that have been

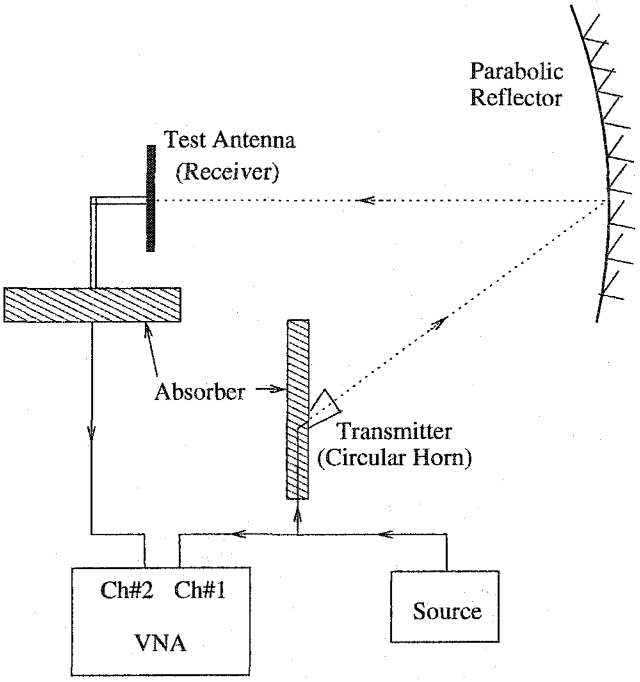

Figure B.2: Experimental setup for measuring the antenna radiation patterns, and axial ratio.

used for the antenna properties reported are equipped with a CATR system.

Figure B.2 shows such an arrangement in an anechoic chamber for measuring antenna parameters. A linearly polarized circular horn antenna is used as a transmitting antenna that illuminates a parabolic reflector, which converts the impinging spherical waves to plane waves near the antenna under test. The test antenna, which is the receiving antenna, receives the signal and sends it to the VNA. The VNA also receives the transmitted signal in its other channel and produces the desired parameters by comparing the two.

Before recording the data for the test antenna the system is calibrated using a standard gain horn antenna. The standard gain horn (8.2-12.4GHz) is used as a test antenna and its radiation patterns are measured in both E and H planes. The calibration coefficients of the system are computed using the measured data and the gain of the horn provided by the manufacturer.

The antenna properties have been measured in two principal planes (E and H). For measuring the E_θ and E_ϕ component of the radiation patterns the transmitting antenna is oriented in the vertical or horizontal polarization and the receiving antenna is rotated in the horizontal plane. E and H plane patterns are obtained by aligning the antenna E and H planes with the horizontal plane, respectively. The axial ratio, which is a measure of the circular polarization, has been measured with the transmitting antenna spinning about its axis continuously while the test antenna is rotated over the desired plane. In order to obtain the desired polarization pattern, the rate of rotation of a linearly polarized antenna is much greater than the rotation rate of the test antenna. The axial ratio pattern obtained in this method is also called spin-linear pattern.

Appendix C

Additional Experimental Results for Chapter 7

A wide band circularly polarized microstrip patch antenna has been described in Chapter 7 and its performances with and without the PBG structures have been analyzed. Experimental results for the PBG patch and the reference patch have also been presented in Chapter 7. Some additional experimental results for both the reference patch and the PBG patch (i.e. input impedance, return loss, and radiation pattern) have been presented in this section.

Figures B.1a and B.1b show the input impedance of the reference patch and the PBG patch, respectively. Two peaks in the input resistance indicate two resonant frequencies of the antennas. The input reactances near the resonant frequencies are close to zero due to the capacitive feed that has been used for these antennas. Figures B.2a and B.2b present the return loss of the antenna without and with the PBG structure, respectively. A significant improvement in the impedance bandwidth of the antenna is observed due to the integration with the PBG structures.

Figures B.3 and B.4 show the linear patterns of the antennas in E and H plane,

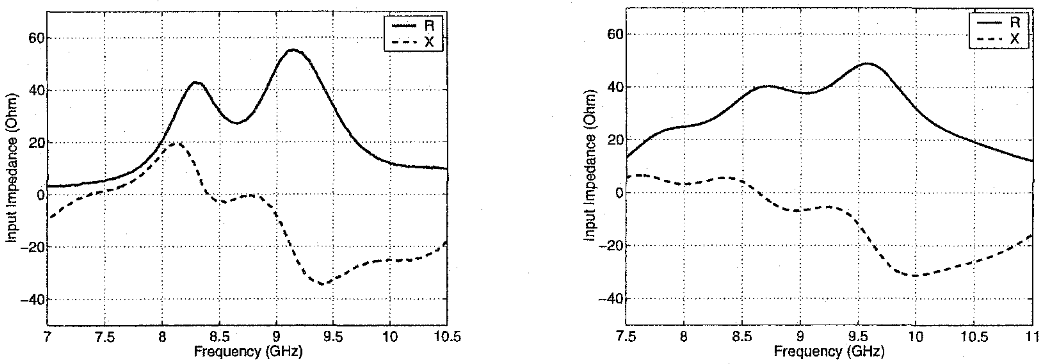

(a) (b)

Figure C.1: Measured input impedance of (a) reference patch, and (b) PBG patch.

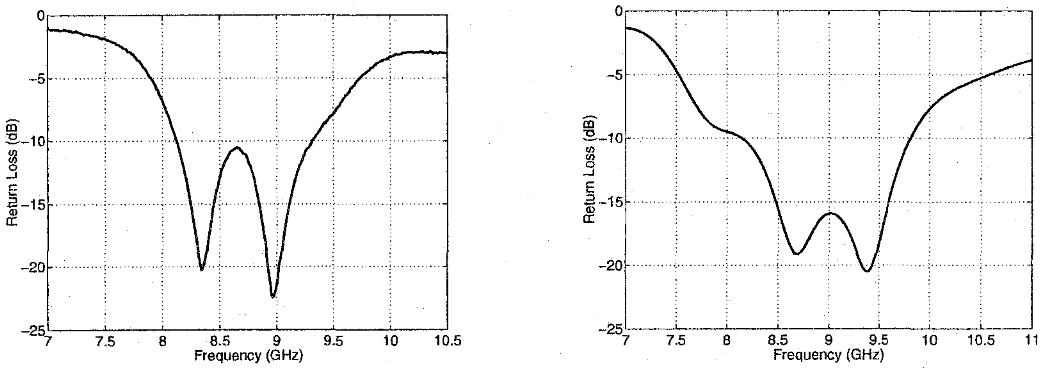

(a) (b)

Figure C.2: Measured return loss of (a) reference patch, and (b) PBG patch.

respectively. It can be observed that when the antenna is integrated with the PBG structures the ratio of E_θ and E_ϕ becomes approximately 1. This also improves the AR of antenna as has been discussed in Chapter 7.

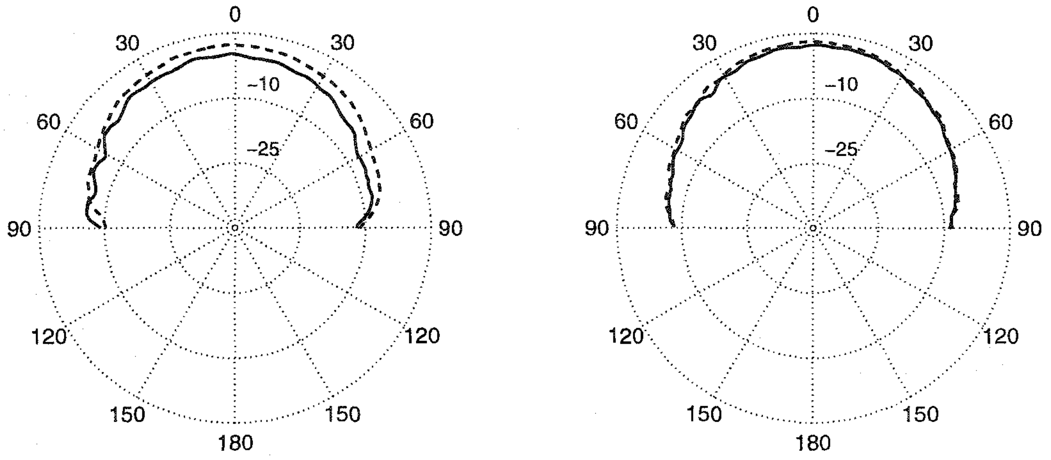

(a) (b)

Figure C.3: Measured radiation patterns of (a) reference patch (8.6GHz), and (b) PBG patch (9.0GHz) in *E-Plane* . (E_θ is the solid line and E_ϕ is the dotted line.)

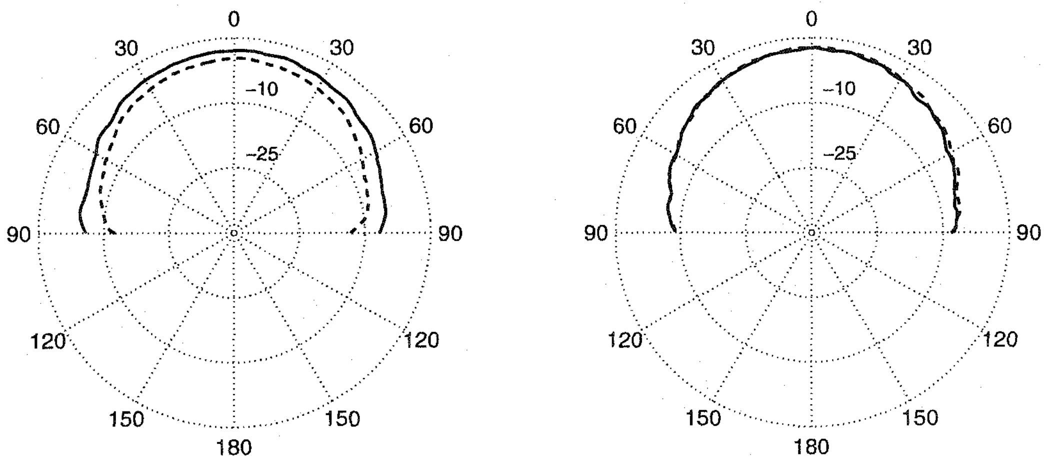

(a) (b)

Figure C.4: Measured radiation patterns of (a) reference patch (8.6GHz), and (b) PBG patch (9.0GHz) in *H-Plane* . (E_θ is the solid line and E_ϕ is the dotted line.)